USING COMPOSITE SPECTRAL ENERGY DISTRIBUTIONS TO CHARACTERIZE GALAXY POPULATIONS AT $1 < z < 4$

A Dissertation

by

BENJAMIN W. FORREST

Submitted to the Office of Graduate and Professional Studies of
Texas A&M University
in partial fulfillment of the requirements for the degree of

DOCTOR OF PHILOSOPHY

Chair of Committee,	Kim-Vy Tran
Committee Members,	Casey Papovich
	Lucas Macri
	James Long
Head of Department,	Grigory Rogachev

May 2018

Major Subject: Physics

ABSTRACT

In this dissertation, I aim to improve our knowledge of galaxy evolution during the first half of cosmic history. To do so I use a sample of $\sim$ 7000 high signal-to-noise galaxies from the FourStar Galaxy Evolution Survey, which provides multi-wavelength imaging and accurate redshifts, allowing analysis of these galaxies' physical properties. I also employ several statistical grouping methods to classify galaxies and build composite spectral energy distributions based on these classifications.

To begin, I analyze galaxies that fall between the blue star-forming cloud and the red quiescent sequence in color space, known as the 'green valley'. Thought to be in the process of shutting down star formation, these galaxies hold the keys to understanding the mechanisms which cause the cessation of star formation, a key point in a galaxy's evolution. I find that such galaxies reside between the star-forming and quiescent populations not only in color and star formation rate, but also in size, Sérsic index, and Hα equivalent width. This suggests that the quenching processes responsible produce changes in these parameters on similar timescales. Additionally, the number density of these green valley galaxies increased by more than a factor of ten from $z = 3$ to $z = 1$, while post-starburst galaxies remain at a roughly constant number density over the same timespan.

I then explore the bluest, most vigorously star-forming galaxies, representing the other extreme of galaxy histories. These galaxies appear much more frequently at $z \sim 3$ than in the local universe and show extreme nebular emission features, consistent with their proposed role in cosmic reionization. I also find that they are clustered around an overdensity at $z = 3.47$, in contrast to locally, where galaxies in clusters are preferentially found to be quenched.

Lastly, I investigate the effects of dust attenuation and reddening on galaxy observations at redshifts $1 < z < 3$. This enables improved constraints on intrinsic galaxy properties such as star formation rate. I find that the average dust properties do not change drastically from $z \sim 0$ to $z \sim 2$, closely replicating a starburst type dust law.

DEDICATION

To my mother and father

For their unending support,

And unshakeable belief,

That one day I'll find my way

In this crazy world of ours.

ACKNOWLEDGMENTS

I must begin by thanking my graduate advisor, Kim-Vy Tran. Your guidance over the last four years has been invaluable, and you've helped keep graduate school as enjoyable as I believe is possible. Now I can finally answer, "What is the scientific goal of your research?" To my committee members Casey Papovich and Lucas Macri - thanks for teaching me most of the astronomy that I didn't know I didn't know in my first year at Texas A&M, and continuing to educate and advise after that. Astronomy is at the point where a deep knowledge and understanding of statistics is critical, and I would not have such (if indeed I do) without the help of James Long.

A special thank you to Rob Kennicutt for providing a role model who is always willing to help students and provide tips for career development. Thank you also to Peter Brown and Ryan Quadri for helping to develop my research abilities, as well as the rest of the astronomy postdocs and faculty at Texas A&M for your knowledge and support. The staff in the Department of Physics & Astronomy has also been fantastic - special thanks to Don Carona, for your help at the campus observatory, and Sherree Kessler for making sure I met all the various deadlines. I'd also like to thank the Mitchell family, particularly the late George P. Mitchell, for their continuing support of astronomy at Texas A&M.

To all of my past teachers and educators from grade school through my time at Rutgers University who have helped shape my intellectual curiosity and encouraged discipline and perserverance - the hours of work you put in have not gone unnoticed, thank you so much. A special thanks to my undergraduate advisor, Andrew Baker, for encouraging me to pursue a graduate research program.

The ZFOURGE collaboration has provided a wonderfully useful dataset with which to work. Team members also had a multitude of insightful comments and suggestions that have helped steer my research into something useful, for which I am grateful. A special thanks to Caroline, Ivo, Lee, Karl, Michael, and Themiya. This survey was based on data gathered with the 6.5 m Magellan Telescopes located at Las Campanas Observatory, Chile - we thank the team at Las Campanas, as well as the instrumentation team at Carnegie Observatories for their work in making the survey

possible. This work is also based in part on observations made with the Spitzer Space Telescope, which is operated by the Jet Propulsion Laboratory, California Institute of Technology under a contract with NASA, and on observations made with the NASA/ESA Hubble Space Telescope, obtained from the data archive at the Space Telescope Science Institute. STScI is operated by the Association of Universities for Research in Astronomy, Inc. under NASA contract NAS 5-26555.

The number of computing packages that have been developed for astronomy in python, IDL, and R that were utilized for this work is too great to list, but a huge thank you to groups that have done so, without whom this Ph.D. would have lasted far longer.

To all the astronomy graduate students at Texas A&M - Samantha, Adam, Jimmy, Heath, Ryan, Brett, Mike, Steven, Ting, Dan, Nancy, Yi, Wenlong, Leo, Andrew, Vince, Peter C., Katelyn, Jonathan, Taylor, Peter F., Sarah, Sijie, Jacqueline, Alex, and Tarini, as well as Emily - thank you for trying to make me have 'fun' and putting up with all the suggestions that we have lunch at IHOP. Your advice, encouragement, and willingness to listen throughout the years has also been invaluable. My friends from the Texas A&M Triathlon Team, without whom I doubt very much I would be here today, also have my gratitude. You helped provide a much needed opportunity to focus and dedicate myself to something other than just academics during my time here.

Finally, the support of my family, particularly my parents, has been a huge comfort throughout my time here. Thanks for listening, counseling, and encouraging me to take the occasional break.

CONTRIBUTORS AND FUNDING SOURCES

Contributors

This work was supported by a dissertation committee consisting of Professors Kim-Vy Tran, Casey Papovich, and Lucas Macri, of the Department of Physics & Astronomy and Professor James Long of the Department of Statistics.

The data analyzed for this work were provided by ZFOURGE, with additional data provided by the *CANDELS - Herschel* Survey. Members of the ZFOURGE team were of great help providing various catalogs and data products.

Parts of the statistical comparison detailed in Appendix 2.4 were completed as part of the graduate course *Statistical Methods for Astronomy*, led by Dr. James Long and Dr. Lifan Wang with assistance from Katelyn Stringer of the Department of Physics & Astronomy and Nayan Chaudhary of the Materials Science & Engineering Department.

All other work conducted for the dissertation was completed by the student independently.

Funding Sources

Graduate study was supported by a Doctoral Merit Fellowship from Texas A&M University, a Heep Fellowship from the Hagler Institute of Advanced Study, and the National Science Foundation under grant #1410728. Further support was obtained through Teaching and Research Assistantships through the Department of Physics & Astronomy.

NOMENCLATURE

Å	Ångstrom
β	Ultraviolet Slope
Ω_Λ	Energy density of the Universe
Ω_M	Matter density of the Universe
λ	Wavelength
ΛCDM	Lambda Cold Dark Matter
$\sigma_{\rm NMAD}$	Median Absolute Deviation
μm	Micron/Micrometer
AB	Absolute Bolometric
AGN	Active Galactic Nucleus
ALMA	Atacama Large Millimeter/submillimeter Array
A_V	Dust Extinction at the V band
CDFS	Chandra Deep Field South
COSMOS	Cosmological Evolution Survey
DOG	Dust Obscured Galaxy
D4000	4000 Ångstrom break
EAZY	Easy and Accurate $z_{\rm phot}$ from Yale
FAST	Fitting and Assessment of Spectral Templates
$f_{\rm esc}$	Escape Fraction
Gyr	Gigayear
H_0	Hubble constant
HAC	Hierarchical Agglomerative Clustering

HST	Hubble Space Telescope
IR	Infrared
IRAC	Infrared Array Camera
IRX	Infrared Excess
JWST	James Webb Space Telescope
$L_{\odot}$	Solar Luminosity
LLE	Local Linear Embedding
$M_{\odot}$	Solar Mass
MIPS	Multiband Imaging Photometer for Spitzer
Myr	Megayear
PACS	Photodetecting Array Camera and Spectrometer
PCA	Principal Component Analysis
SED	Spectral Energy Distribution
SNR	Signal to Noise Ratio
SFH	Star Formation History
SFR	Star Formation Rate
sSFR	Specific Star Formation Rate
UDS	The Ultra Deep Survey
ULIRG	Ultra Luminous Infrared Galaxy
UV	Ultraviolet
Z	Metallicity
z	Redshift
$z_{\rm phot}$	Photometric Redshift
$z_{\rm spec}$	Spectroscopic Redshift
ZFOURGE	FourStar Galaxy Evolution Survey

TABLE OF CONTENTS

Page

LIST OF FIGURES

FIGURE Page

LIST OF TABLES

TABLE Page

1. INTRODUCTION

1.1 The Evolution of Galaxy Populations

Galaxy evolution is a complex topic and has been the focus of increasingly intense research over the last two decades. Properties such as the mass, star formation rate, size, kinematics, and environment of a galaxy influence how it will evolve in the near future, and can also offer clues to its evolutionary history. In general, the massive dark matter halos of galaxies gravitationally attract pristine gas from the nearby universe. Additional gas can be provided by a merging galaxy, or recycled from galactic outflows. Whatever the source, as this gas cools and condenses it forms new stars. The amount and color of light that these stars emit varies tremendously with their masses. Analysis of this light informs scientists about the current state of star formation in a galaxy. The growth of this stellar mass varies over a galaxy's lifetime, and the most massive galaxies today are observed to have virtually no ongoing star formation.

Due to the long timescales of galaxy evolution, tracking the evolution of a single galaxy directly is impossible. Thus, discoveries are often made by studying populations of galaxies at various epochs throughout cosmic history. From such studies it has become clear that the universe as a whole reached the peak of its star formation about 10 Gyr ago (see Figure 1.1; Madau & Dickinson, 2014). This observation is a confluence of both a large number of galaxies forming stars, and a large number of stars being formed in each star-forming galaxy.

The fraction of galaxies that are no longer forming stars has increased with the age of the universe since galaxies began to cease star formation, an event known as quenching (Tomczak et al., 2016). Such quenched galaxies existed as early as when the universe was only ~ 1.5 billion years old (Straatman et al., 2014; Glazebrook et al., 2017). From snapshots of a range of cosmic times, these galaxies make up the massive end of the stellar mass distribution of galaxies.

In addition, the rate at which a typical star-forming galaxy produces new stars today is lower than that of typical star-forming galaxies at earlier epochs (Whitaker et al., 2012b; Tomczak et al.,

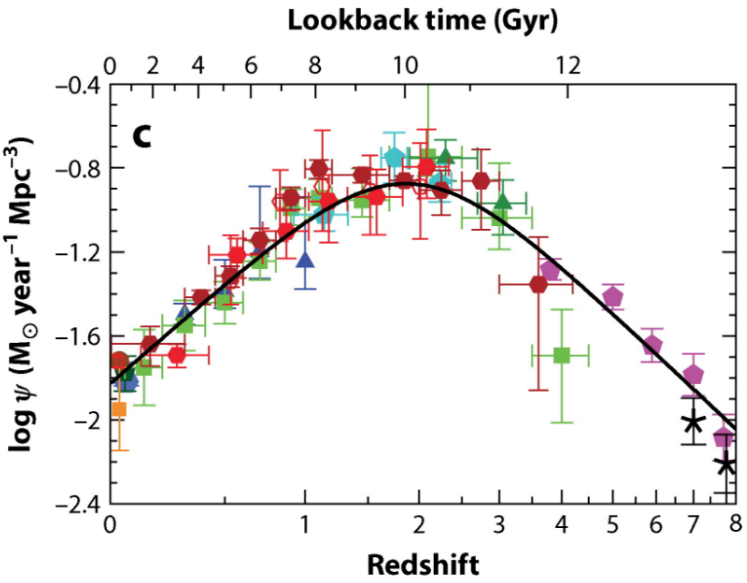

Figure 1.1: The cosmic star formation density history from Madau & Dickinson (2014). This is the amount of mass transformed into stars per year per unit comoving volume throughout the history of the universe. Colored points represent results from a range of experiments, probing ultraviolet or infrared light to determine star formation rate. This star formation density of the universe is seen to peak around 10 Gyr ago.

2016). This may be due to a decrease in available gas for turning into stars or a lower efficiency with which such gas forms stars. While there are still young galaxies today that are vigorously birthing new stars, they are rarer than in the past (Cardamone et al., 2009; Maseda et al., 2016).

Furthermore, all but the very youngest galaxies are partially obscured by dust, which is ejected into the interstellar medium by massive stars and supernovae. This dust decreases the amount of ultraviolet (UV) light observed from a galaxy, a direct indicator of recent star formation. While it re-emits the energy from these photons in the infrared (IR), converting the IR light back to intrinsic UV light requires assumptions about properties of the dust such as grain size and distribution relative to stars. Additionally, the scaling factors used to derive the dust corrected star formation rates are determined from relations observed in nearby galaxies, which may not hold at high redshift.

In this dissertation, I address the above concerns by analyzing populations of galaxies from the FourStar Galaxy Evolution Survey grouped by their distributions of emitted light across a range of wavelengths, known as spectral energy distributions (SEDs). Using this composite spectral energy

distribution method, I explore the three areas above: the cessation of star formation, the most vigorously star-forming galaxies, and dust obscuration.

1.2 Shutting off Star Formation

At this time the mechanisms that cause the cessation of star formation are still not completely understood. Since cool gas is required for star formation, gas must either be heated or removed from the galaxy to shut off star formation. A large number of possible environmental processes, such as ram pressure stripping, galaxy-galaxy interactions and gas starvation, which remove gas from a galaxy, have all been proposed (Darvish et al., 2016). Other studies show that internal mechanisms such as mass quenching and feedback from active galactic nuclei (AGN) can be responsible (Kocevski et al., 2017; Papovich et al., 2018). Furthermore, it has also been suggested that a high galaxy central density can prevent the gravitational collapse of gas to form stars (Martig et al., 2009; Zolotov et al., 2015a; Barro et al., 2017). Not only do several or all of these mechanisms almost certainly play a role in various galaxies, but their relative importance can vary as a function of redshift and galaxy mass.

Whatever the processes are, they quench galaxy star formation relatively quickly, generally on timescales less than two billion years (Couch & Sharples, 1987; Tran et al., 2003; Nelson et al., 2017; Davé et al., 2017; Pandya et al., 2017). While the brevity of this timescale relative to galaxy lifetimes makes such galaxies rare, galaxies in this phase hold the keys to unlocking and understanding these quenching processes.

The best known of these galaxies are the post-starburst galaxies. These galaxies have large numbers of A stars, but little evidence of blue, massive O and B stars. B stars have main sequence lifetimes of ~ 1 Myr, while A stars reside there for ~ 1 Gyr - as a result, star formation in post-starburst galaxies shut off in the past somewhere between these two times.

Additionally, a small fraction of galaxies ($\sim 6\%$ from Fang et al., 2012, but this depends heavily upon selection cuts) have colors and morphologies between typical star-forming and quiescent populations, lacking the clear spectral signatures of post-starburst galaxies. This so-called 'green valley' was first pointed out in data from the *Galaxy Evolution Explorer* (*GALEX*) and the *Sloan*

Digital Sky Survey (*SDSS*) (Salim et al., 2007; Wyder et al., 2007; Martin et al., 2007). The prevailing hypothesis is that these galaxies are in the process of shutting off star formation. Analyzing differences in evolution of morphology, specific star formation rate, and color for these populations informs the order in which these properties change, and therefore which mechanisms are the cause.

Not all galaxies necessarily stop star formation forever though. Recent simulations have shown that galaxies can be 'rejuvenated' and have bursts of star formation after previously shutting off (Nelson et al., 2017). Thus, some of the green valley may be populated by galaxies which have recently gotten bluer and increased their star formation. Discovering differences between these galaxies and those in the process of quenching are essential to understanding galaxy evolution.

1.3 Rapidly Star-Forming Galaxies as Cosmic Reionizers

At the other end of the galaxy lifespan are small, young galaxies, with impressively high levels of star formation. While quenching galaxies have ratios of star formation to stellar mass (specific star formation rate; sSFR) of $\sim 10^{-10.5}$ yr^{-1}, these galaxies approach sSFR values of $\sim 10^{-8}$ yr^{-1} (Dickey et al., 2016).

Galaxies with such rapid star formation produce large amounts of high-energy radiation from their young, massive stars. If this radiation interacts with nearby gas, the gas can be excited or even ionized - for many of these young galaxies, [O III]$\lambda 5007$ equivalent widths (EW) of 300-1500Å are seen. Such galaxies have been found in the local universe but are not common, with $\sim 2/\mathrm{deg}^2$ brighter than 20.5 mag (Cardamone et al., 2009; Izotov et al., 2011).

However, similar galaxies appear more frequently at higher redshifts (van der Wel et al., 2012; Maseda et al., 2016). With sufficient numbers, these galaxies can contribute to reionization of the universe at $z \sim 7$ (Robertson et al., 2015).

The actual ionizing photons themselves have proven elusive at high redshifts, with the best known confirmed source *Ion2* at $z = 3.218$ (Vanzella et al., 2015; de Barros et al., 2016). As a result, other tracers of ionizing photons such as large oxygen emission lines are used to select candidates for follow-up (Nakajima & Ouchi, 2014). This has been done out to $z \sim 2$ in several works (van der Wel et al., 2011; Hagen et al., 2016; Maseda et al., 2016).

At higher redshifts, excesses in broadband photometry can be used to identify candidates for spectroscopic follow-up, although samples remain small (Stark et al., 2013; Smit et al., 2014). Increasing the number of candidates for spectroscopic follow-up at $z \sim 3-4$ remains an important piece of determining the number density evolution and escape fraction of these rapidly star forming galaxies, and the contribution of similar galaxies at higher redshifts to cosmic reionization.

1.4 Dust Attenuation and Reddening

The characterization of dust in galaxies is an ongoing challenge in extragalactic astronomy, particularly at high redshift. Dust grains are produced by massive stars and processes in the interstellar medium (e.g., Draine, 2003). These grains scatter and absorb ultraviolet (UV) light from young, massive stars, and are heated, reemitting the energy in the far infrared (IR). The manner in which they do so depends upon not only the quantity and type of dust grains, but also their geometry with respect to stars in a galaxy.

Correcting for this attenuation at blue wavelengths is where the challenge lies. In the nearby universe, this is somewhat easier, as resolved galaxies have many lines of sight which can be used to characterize the dust distribution. Pei (1992) presented extinction curves for the Milky Way and both Magellanic Clouds based on averages of sight lines to individual stars of known spectral type. Calzetti et al. (1994) used a sample of blue compact and starburst galaxies to derive an alternative for such rapidly star-forming galaxies.

Often in extragalactic work, the assumption is made that the dust forms a screen in front of the stars, instead of being mixed in, as seems likely to be the physical reality (e.g., Calzetti, 2001; Reddy et al., 2010; Tress et al., 2018). To first order, this assumption does not significantly affect derived results except for those galaxies with large amounts of dust such as ultra-luminous IR galaxies (ULIRGs; e.g. Charlot & Fall, 2000; Kennicutt et al., 2009).

Additionally, far IR measurements make quantification of the energy absorbed by dust easier. Many works have used a weighted UV and IR dust characterization to derive properties such as star formation. Until recently, this was difficult at high redshifts, as the angular resolution of telescopes such as the *Herschel Space Observatory* is large (tens of acrseconds), making source confusion and

contamination significant problems. Recently, ALMA has given scientists the ability to do similar work at higher redshifts.

There is also some degeneracy between the intrinsic colors of a galaxy and its dust content, particularly when only photometry is available. Meurer et al. (1999) developed a metric, IRX-β, which nicely separates out red galaxies by comparing the UV colors to the ratio of UV to IR light. For their sample of local starburst galaxies, the results agree nicely with the starburst dust law of Calzetti et al. (1994).

Several studies have traced this relation to higher redshifts, finding some evidence for different dust attenuation curves (Reddy et al., 2012a; Penner et al., 2012; Casey et al., 2014; Salmon et al., 2016). This apparent evolution of average dust properties suggests that a more flexible parameterization, such as that of Noll et al. (2009b) or Salmon et al. (2016), is necessary to better characterize dust attenuation, and thus remove its effects from observations.

1.5 The FourStar Galaxy Evolution Survey

In this work I use data from the FourStar Galaxy Evolution Survey (ZFOURGE; Straatman et al., 2016) to address the gaps in knowledge mentioned in Section 1.1. ZFOURGE is an international collaborative survey which used 45 nights on the 6.5m Magellan Baade Telescope in Chile (Persson et al., 2013) to image three extragalactic fields on the sky - the Chandra Deep Field South (CDFS), Cosmic Evolution Survey field (COSMOS), and the Ultra Deep Survey field (UDS).

The 45 nights of imaging over 400 arcmin^2 of sky allowed for deep imaging (limiting magnitude $K_s\sim$ 26) and thus sensitivity to faint and distant galaxies. The three fields have been extensively imaged by previous surveys, with up to 40 photometric measurments from 0.3-8μm, so the shape of the SED for detected galaxies can be well constrained. Previous images in the K-band from these surveys were also stacked with the ZFOURGE K_s-band observations, yielding an impressively deep detection image of ~ 26 AB mag, a factor of $\sim 10^8$ times fainter than visible with the naked eye.

1.5.1 Accurate Photometric Redshifts

The universe is expanding at an accelerating rate (Riess et al., 1998). As a result of this expansion, the farther away a galaxy is, the faster the space between the galaxy and the observer is growing. The observational effect is phenomenologically similar to a Doppler shift, although the underlying mechanism is different. As such, a measurement of a galaxy's recessional velocity is an effective proxy for its distance. While the gravitational attraction between the Milky Way and other nearby galaxies, such as Andromeda, is strong enough to overcome this expansion, and factors such as environment can add scatter to it, the relationship holds for distant galaxies.

This apparent stretching and reddening of light due to this cosmological expansion is known as redshift (z). For two galaxies with different redshifts, the light which is observed with a certain filter is not emitted at the same wavelength. Only by accurately correcting for the different redshifts of galaxies can we compare the physical processes intrinsic to those galaxies. This increases the importance of having observations over a wide range of wavelengths.

Measuring redshift is much easier than any geometric measure of distance for distant galaxies. It is typically determined by looking for prominent spectral features, such as strong emission lines, in a galaxy's SED. The ratio between the observed wavelengths of these features and their known rest-frame wavelengths at which the feature is emitted gives the redshift,

$$1 + z = \frac{\lambda_{\rm obs}}{\lambda_{\rm rest}} \tag{1.1}$$

While local galaxies effectively have $z = 0$, and $z \sim 0.75$ corresponds to a time when the universe was half its current age, the earliest discovered galaxies have $z \sim 10 - 11$, when the universe was less than 0.5 Gyr old (Coe et al., 2013; Oesch et al., 2016; Salmon et al., 2018).

ZFOURGE imaging was conducted with five intermediate-band mid-infrared filters. Compared to traditional broad-band filters, this increased the effective spectral resolution of the survey at wavelengths corresponding to the 4000Å-break at $1 < z < 4$. Combined with previous multi-wavelength observations, precise identification of this well-known feature improved the ability to

constrain galaxies' redshifts more effectively than possible with standard photometry.

1.5.2 Composite Spectral Energy Distributions

Nearly all astronomical knowledge stems from studying electromagnetic radiation, or photons, from distant objects (the exceptions being neutrinos, and very recently, gravitational waves). The quantity of photons, as well as their distribution over a range of energies (typically measured as wavelengths in astronomy) make up the spectral energy distribution (SED) of a source. The greater detail we have of this SED, the more we can deduce about the source's properties.

Astronomers have two broad categories for how finely the SED is sampled - photometry and spectroscopy. The difference between these two from an instrumental standpoint can be complex, but the effect is simply a difference in size of the wavelength bins into which photons are split. Photometry uses broad filters, which enable the detection of faint galaxies, but have low wavelength resolution. Doing so allows detection of faint objects, and analysis of colors and morphologies. Without the precise knowledge of spectral line locations however, redshifts to photometrically identified objects ($z_{\rm phot}$) are much less certain than those observed spectroscopically ($z_{\rm spec}$).

Spectroscopy splits light passing through a filter into many fine bins, which allows for detailed analysis of aspects such as spectral lines and galaxy kinematics. However, this also limits spectroscopy to studying brighter objects than photometry for a given amount of telescope time. As a result, the largest and deepest extragalactic surveys are limited to photometric observations.

The composite SED method generates low resolution spectra of statistically grouped galaxy populations using photometry alone. This enables the analysis of spectral features for objects that are too faint to be spectroscopically detected. Additionally, detailed properties can be studied for populations of galaxies instead of individual ones. Thus, advantages of both photometry (depth, broad wavelength coverage) and spectroscopy (line analysis) are accessible with this method, and its usefulness has been demonstrated in many projects (e.g., Kriek et al., 2011; Kriek & Conroy, 2013; Utomo et al., 2014; Forrest et al., 2016; Yano et al., 2016; Forrest et al., 2017).

The ZFOURGE data set is perfectly suited to the composite SED method due to its accurate photometric redshifts, large number of galaxies, and impressive depth, which allows us to probe

faint populations out to $z \sim 4$. I detail the composite SED method in Section 2, and use these composite SEDs in Section 3 to determine which galaxies have lower star formation rates than other galaxies of similar mass. I then analyze other properties, such as morphologies, emission line equivalent widths, and number densities to address quenching timescales and mechanisms from $z \sim 4$ to $z \sim 1$.

Section 4 presents a population of extreme emission line galaxies which offer clues to the earliest phases of star formation in galaxies as well as the role of star forming galaxies in cosmic reionization. In Section 5, I show that the average dust law at $z \sim 2$ is consistent with the starburst dust law derived from local star-forming galaxies. The conclusions of the dissertation and directions of future research are presented in Section 6.

2. CONSTRUCTION OF COMPOSITE SEDS

The composite SED method was first introduced in Kriek et al. (2011). Briefly, this method groups galaxies together based on SED shape, then de-redshifts and scales photometric observations of those galaxies at different redshifts to increase the spectral resolution of said objects. This section details the method, including slight alterations that we made in the course of development, as well as various tests, validations, and comparisons to other statistical grouping methods. All references to clusters in this section refer to galaxy data grouped in a statistical sense, not the astronomical definition.

2.1 Data Selection

The strength of the composite SED method relies upon being able to accurately group galaxies together by SED shape from multi-wavelength photometry. Therefore, galaxies in a sample of interest must have photometry spanning a wide range of wavelengths, ideally from the near-UV to the IR. To minimize vertical scatter in the resultant composite SED, the data must have high signal to noise (SNR) - in this work we require $SNR > 20$ in the detection imaging. Similarly, a poor redshift estimate will increase scatter on the horizontal axis. The ZFOURGE galaxies used in this sample have a characteristic $\sigma_{\rm NMAD} \sim 0.02$ (Straatman et al., 2016; Nanayakkara et al., 2016), extremely good for photometric redshifts. Finally, galaxies at a range of redshifts must be included in order to increase the resolution of the composite SED. However, if the range is too large in redshift, there will not be overlapping observations in the rest-frame with which to compare galaxies.

2.2 Synthetic Rest-Frame Photometry

Many methods of statistical comparison have difficulty with unevenly spaced data, such as the rest-frame wavelengths observed for objects at different redshifts. This is solved by generating synthetic rest-frame photometry for all galaxies of interest based on template fitting.

For this process I use EAZY (Brammer et al., 2008), which fits a set of galaxy SED templates

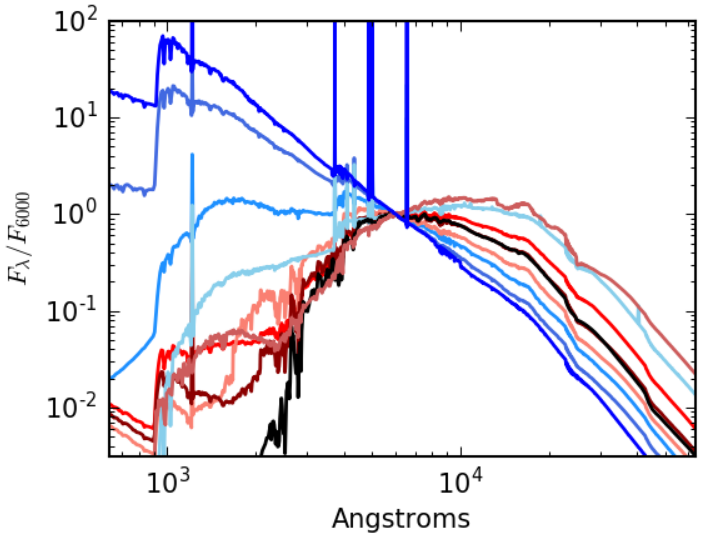

Figure 2.1: EAZY galaxy SED templates. The EAZY templates used to fit galaxy SEDs, the same as used in ZFOURGE (Straatman et al., 2016). The template with the greatest flux at 1000Å is a high-EW model from Erb et al. (2010), while the template with the greatest flux at 1μm is an old, dusty template Straatman et al. (2016). Other templates are included with EAZY (Brammer et al., 2008).

to observed photometry in linear combination to generate a best fit SED. A set of nine galaxy SED templates from Fioc & Rocca-Volmerange (1999); Brammer et al. (2008); Erb et al. (2010); Whitaker et al. (2011); Straatman et al. (2016) is used to fit each galaxy (see Figure 2.1. The templates are described in Section 5.1 of Straatman et al. (2016).

Top hat filters are then used to generate synthetic photometry. In order to exclude the effects of the resonant Lyman-α line as well as probe the reddest wavelengths of the *Spitzer*-IRAC bandpasses at moderate redshifts, these filters range from 1240Å to 5.5μm. These filters have equivalent bandpass widths in logarithmic space, and the central wavelengths are evenly spaced in logarithmic space:

$$\log_{10}(\lambda_{c,i}/\text{Å}) = 3.13 + 0.073i \tag{2.1}$$

Thus, they weight every wavelength of those between $1226 < \lambda/\text{Å} < 49580$ equally in $\log_{10}$

space.

The ZFOURGE data have 25-40 photometric measurements per galaxy, ranging from $0.3 - 8.0\mu$m. Additionally, any synthetic filters which lie outside observed wavelengths are not used in galaxy comparison, preventing any extrapolation from the data.

2.3 Building Methodology

2.3.1 Grouping Galaxies

Galaxies are grouped together based on their SED shape as determined from the synthetic rest-frame photometry, f_λ^{rf}, described above. This is compared using the b-parameter below, which quantifies the dissimilarity between two sets of synthetic rest-frame photometry. Only the colors are compared, and a is a scaling factor to take out flux differences - thus two galaxies with the same SED shape will have $b = 0$. Between any two galaxies, we only compare those filters which lie between the rest-frame wavelengths photometrically observed for both galaxies. Thus, galaxies at vastly different redshifts will have few filters compared - this is taken into account when choosing a sample redshift range. This prevents any similarity due to extrapolation of SED shape, but also means that galaxies across wider redshift ranges will have fewer data points used in comparison.

$$b_{12} = \sqrt{\frac{\Sigma(f_\lambda^{rf1} - a_{12} f_\lambda^{rf2})^2}{\Sigma(f_\lambda^{rf1})^2}} \tag{2.2}$$

$$a_{12} = \frac{\Sigma f_\lambda^{rf1} f_\lambda^{rf2}}{\Sigma(f_\lambda^{rf2})^2} \tag{2.3}$$

Each section of the dissertation details the specific sample used for each work, which have different redshift cuts and parent catalogs. Once a sample is selected, each pair of galaxies is compared, and a and b are calculated. All pairs below a certain threshold in b are considered. This threshold is chosen in concert with the SNR cut such that two intrinsically identical galaxies will be grouped together if each has random noise of the cut level. For the work in this dissertation, we require $SNR_{K_s} > 20$ and $b < 0.05$.

From the list of matches, the galaxy with the largest number of matched galaxies, termed the *primary*, and all of said matched galaxies, termed *analogs*, are removed from the sample and placed into a group. This is done repeatedly until the largest remaining group has five or fewer galaxies. At this point, each analog is again compared to all of the primaries, and placed into a group of the primary with which it has the lowest value of b. Doing so prevents galaxies that are matches with multiple primaries from simply being placed in the largest group. Galaxies in each group with at least twenty galaxies are then used to construct a composite SED. In several instances, other groups are also analyzed, which are detailed in the respective section above.

2.3.2 Composite SEDs

When the groups are finalized, observed photometry from all galaxies is then deredshifted according to ZFOURGE $z_{\rm phot}$ measurements and scaled to the primary using the scaling factor a in Equation 2.3. If two galaxies are at different redshifts, this effectively doubles the spectral resolution of photometry probing the intrinsic SED. When this is done for groups of many galaxies, the result is a low-resolution spectrum.

We then split these observed photometric points for a group into wavelength bins with equal numbers of observations per bin. The bins therefore are not necessarily equal in wavelength size, nor are they the same between different composite SEDs. Medians of the de-redshifted, scaled photometry in each wavelength bin are taken, generating the composite SED, as shown in Figure 2.2.

In what follows we work only with groups of at least 19 galaxies (with three exceptions, detailed in Sections 3.4.2 & 3.4.3), which allows for good characterization of the intrinsic SED shapes. Groups of galaxies that passed our cuts but were not placed into composite SEDs due to their small sizes were inspected as well - these are susceptible to noisy observations. While we require $SNR > 20$ for the K_s detection bandpass, other bands for these galaxies have much lower SNR. If photometry in several bands is particularly noisy in the same direction, a group of galaxies may fail the similarity criteria and be placed into separate groups.

As a result, many of these small groups look very similar to other composites in e.g., the

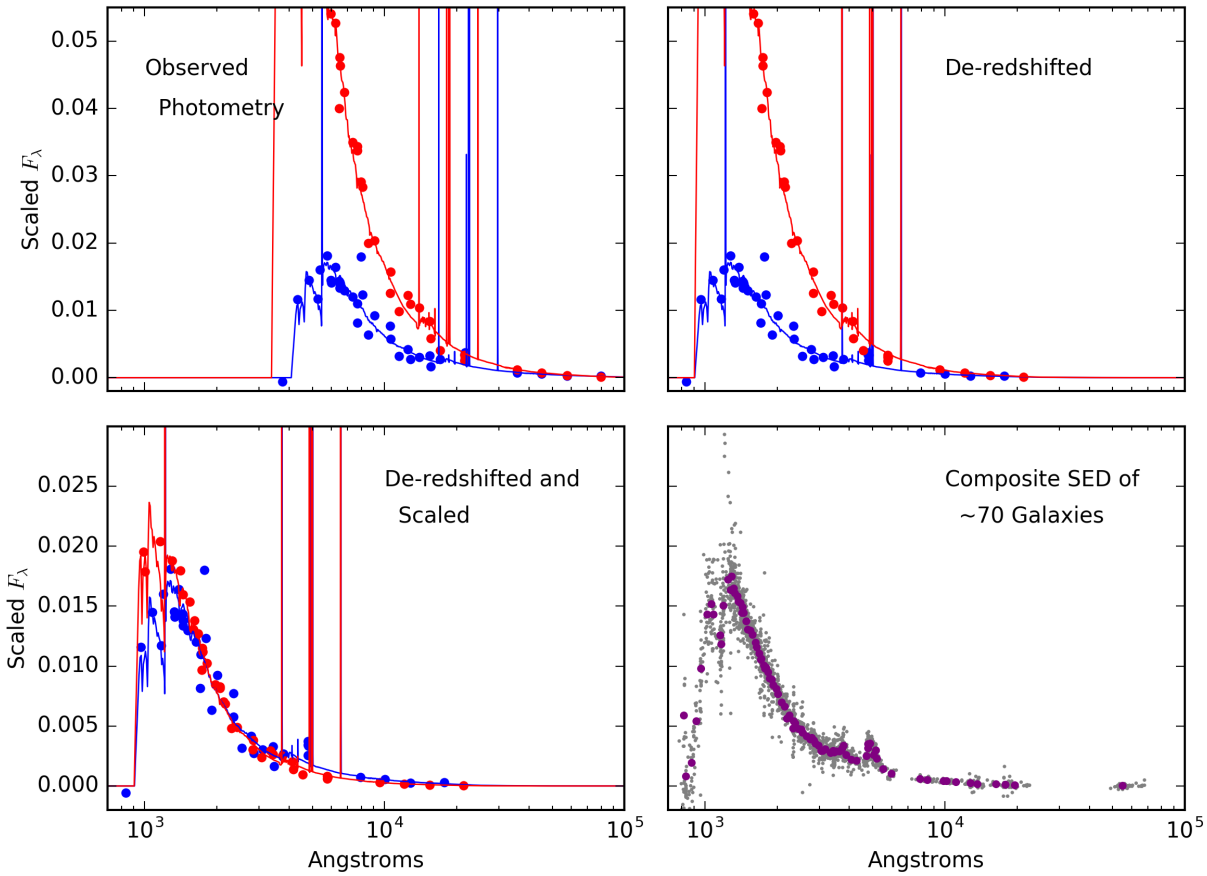

Figure 2.2: Composite SED construction method. The observed photometry (points) and best-fit SEDs of two similar galaxies are shown in the top left panel. These are de-redshifted (top right), and scaled to match (bottom left), effectively doubling the resolution of the photometry. With a significant number of galaxies, a composite SED with impressive spectral resolution ($R \sim 50$ in the near-UV to optical) can be derived from photometric observations alone. An example is shown in the bottom right, with photometric observations in gray and median points in purple.

optical wavelengths, but offset in the e.g., near-infrared. While the possibility exists that these are an intrinsically separate population, these galaxies are a larger fraction of the high-redshift sample consistent with the effects of noise. Regardless, no group appears to have a drastically different SED shape overall, and merging a group with another similar SED shape would not effect our results due to their small numbers.

There are also non-detections in the data, particularly for quiescent galaxies in the UV, and we include these when calculating the composite SED points (i.e., negative fluxes are included when calculating medians). If the median signal for the analog points in a bin has $SNR < 1$, the associated composite SED point is considered an upper limit. This is often seen in the far-UV and near-IR regions of the composite SEDs where there is little flux relative to instrument sensitivities. The final sets of composite SEDs are shown in the Appendix.

2.3.3 Custom Composite SED Filter Curves

Median values of the deredshifted, scaled photometric values in each wavelength bin are the composite SED points. Each of these median points also has an associated composite filter response curve, which is a linear combination of the deredshifted photometric filters. A given filter curve is compressed into the observed galaxy rest-frame and scaled (using a value k) such that there is equal area (C) under the resulting response curve:

$$\lambda_{comp} = \lambda_{filter,rest}/(1+z) \tag{2.4}$$

$$C = k \int_{\lambda_{comp,min}}^{\lambda_{comp,max}} R_{filter,rest} d\lambda_{comp} \tag{2.5}$$

This ensures that each photometric observation is equally weighted and contributes the same amount to the composite filter response curve. These filter curves allow the characterization of the composite SEDs using EAZY and Fitting and Assessment of Synthetic Templates (FAST; Kriek et al., 2009).

2.4 Comparison to Other Grouping Methodologies

The composite SED method as introduced in Kriek et al. (2011) is comprised of two pieces. While the deredshifting of galaxy photometry to increase resolution is relatively straightforward, the statistics used to group galaxies together are not as singular. In this section I compare to three other statistical grouping methods in order to validate the effectiveness of using Equations A.3 and A.4.

2.4.1 Principal Component Analysis

Principal Component Analysis (PCA) is a statistical tool developed over a century ago that finds which eigenvectors of a multi-dimensional dataset explain the highest amount of variance (e.g., Pearson, 1901; Wold et al., 1987). Doing so allows a dimensionality reduction which is particularly useful in identifying the discriminating spectral features that allow differentiation between galaxy classes. While an extremely useful tool, PCA requires that data are consistent in wavelength space

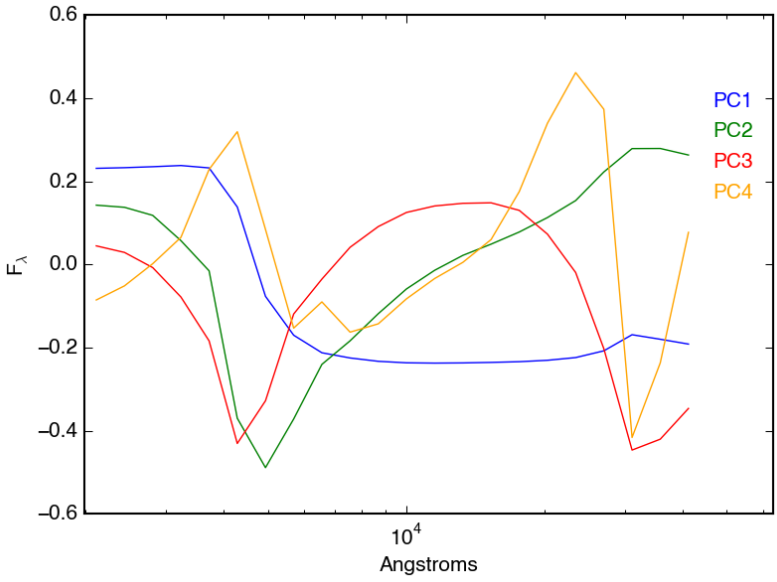

Figure 2.3: Principal components from galaxy photometry. The first component (blue) can clearly be attributed to unobscured star formation with its large UV flux. PC2 (green) corresponds to the strength of the 4000 Å break and the population of A stars; post-starburst and quiescent populations have large negative coefficients for this component.

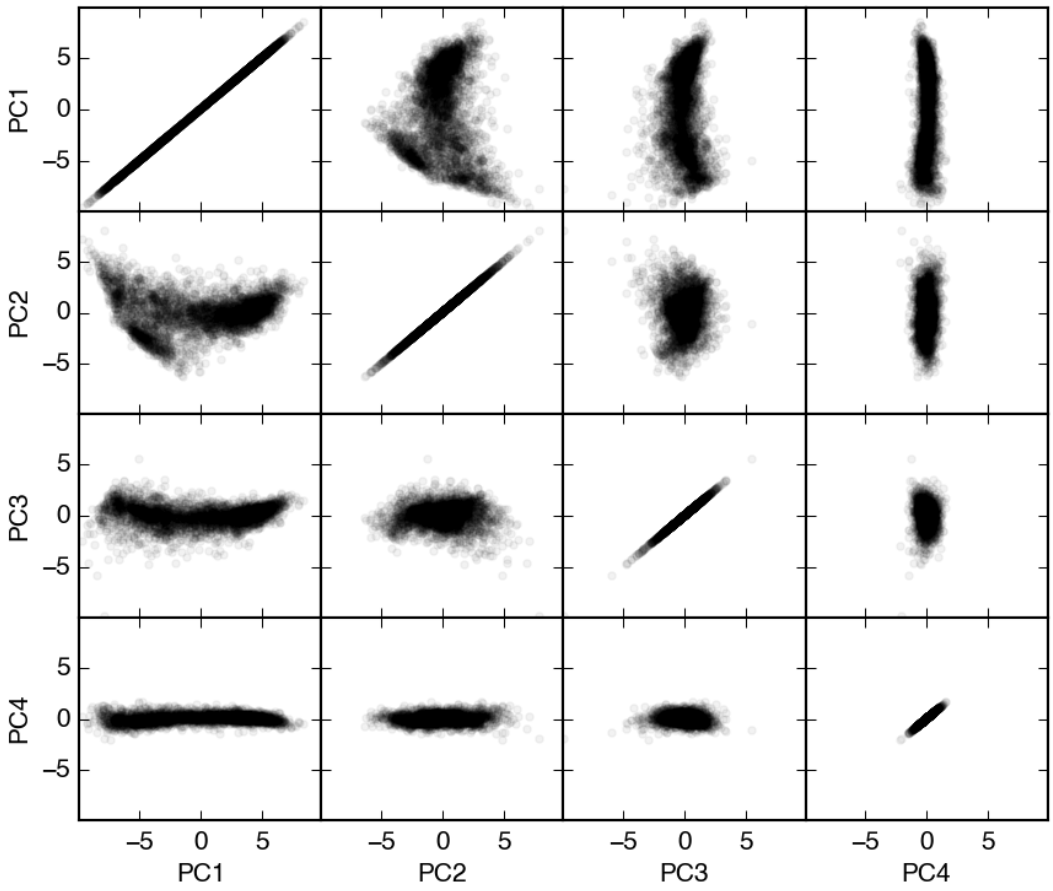

Figure 2.4: Eigenvector pairs for the first four principal components. Significant structure is only visible when comparing the first two.

(Functional PCA, which does not have this requirement, necessitates a series of functional curves, and was beyond the scope of this work). As such, PCA was performed on the 22 bands of synthetic rest-frame photometry of galaxies analyzed in Section 5.

For this process I begin by normalizing the rest-frame photometry such that its sum is one for each galaxy. I also subtract off the mean values and normalize by the standard deviation,

$$X' = (X - 1\mu^T)S^{-1}. \tag{2.6}$$

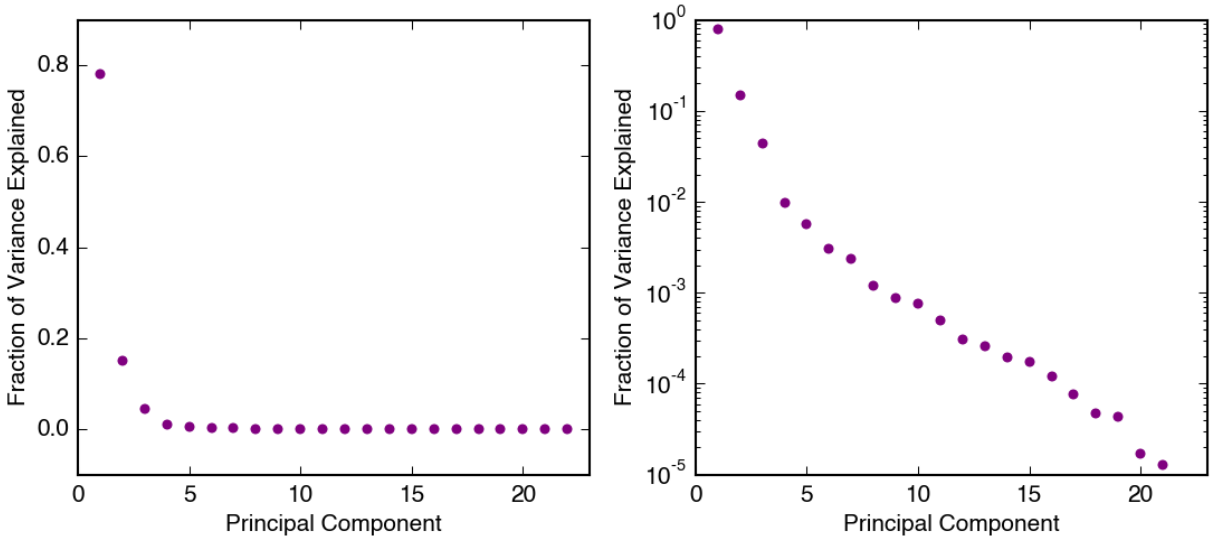

Figure 2.5: Principal component scree plot. A scree plot showing the variability explained by the different principal components of our decomposition. 93% of the variance is due to differences in the first two eigenvalues.

The decomposition goes as

$$X' = U\Sigma V^T, \tag{2.7}$$

where U is the set of eigenvalues in the new space, V are the eigenvectors (components), and Σ describes the amount of total variance that is explained by each component. The first four principal components as functions of wavelength are shown in Figure 2.3.

I can also compare the eigenvalues of different components to each other and look for structure there, as in Figure 2.4. Any extended, non-elliptical structure on these plots implies separate populations. Such structure is clearly seen in PC1 and PC2, and is less visible in other comparisons, including those of other principal components not shown.

A useful analytical tool at this point is a scree plot, which shows the amount of variance between galaxies which is explained by a particular component (Figure 2.5). This confirms the hypothesis from Figure 2.4 which suggested that the first two components can be used to discriminate between different SED shapes.

Next, I make cuts based on the visual clusters in the comparison between principal components

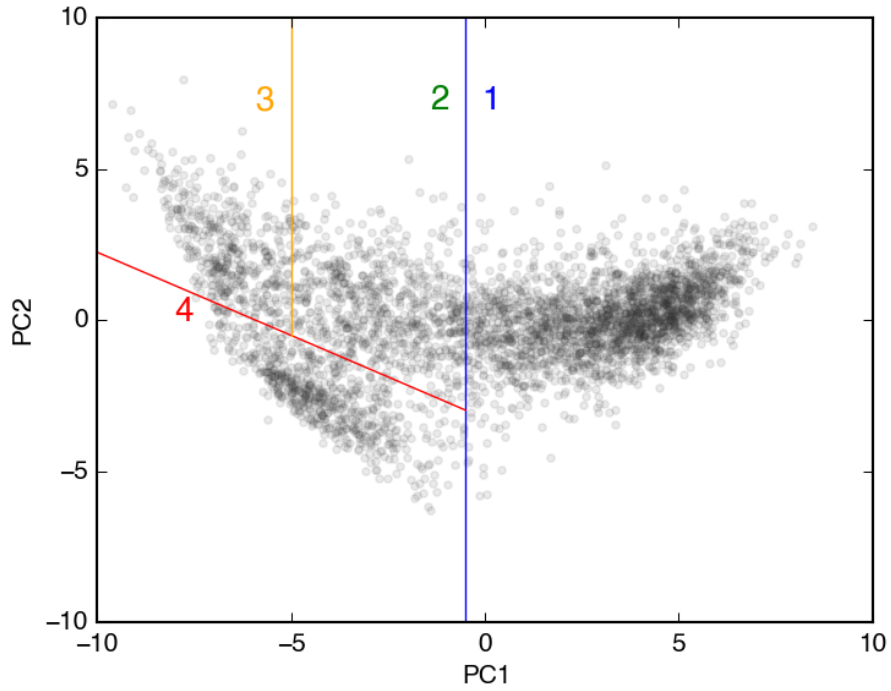

Figure 2.6: Principal component selection cuts. Group 1: PC1 > -0.5. Group2: $-5 <$ PC1 < -0.5 and PC2 > -0.55 PC1 -3.25. Group3: PC1 < -5 and PC2 > -0.55 PC1 -3.25. Group4: PC1 < -0.5 and PC2 < -0.55 PC1 -3.25.

1 & 2 (Figure 2.6). The resulting clusters shown in Figure 2.7 reinforce beliefs about the physical nature of the first two principal components, and also yield some new insights. Similar to a UVJ diagram, a continuum of star forming galaxies is seen, as well as a separate wedge for the quiescent population. In Figure 2.6 the star-forming trend from dust-free to dust-obscured goes from right to left, with quiescent galaxies lying in the lower left quadrant. All three star-forming groups (1,2, & 3) show clear evidence of Hα emission, which the quiescent group (4) lacks. As noted in previous methods, the star forming population does appear to be a true continuum, characteristic of the evolution of galaxies, and not composed of distinct clusters. This can also be seen in the resulting composites as there seems to be a small amount of overlap between the extremes of SED shapes in different composites.

2.4.2 *Hierarchical Agglomerative Clustering*

Next, I use hierarchical agglomerative clustering to analyze the same sample. This method begins by treating each galaxy as its own cluster, then merging the two most similar clusters and repeating the process until the desired number of clusters are obtained. In this work I use complete linkage; for every two clusters C_i and C_j, the dissimilarity is calculated as a distance,

$$D(C_i, C_j) = \max_{x \in C_i, x' \in C_j} d(x, x'). \tag{2.8}$$

That is, the 'distance' between two clusters is considered the maximum distance attainable between two points, one in each cluster. The two clusters with the smallest $D(C_i, C_j)$ are merged to form a new cluster.

For this example a first guess is made by selecting a cut such that

$$N_{clusters} \times min(D(C_i, C_j)) \sim 1. \tag{2.9}$$

This creates 10 clusters, with $min(D(C_i, C_j)) = 0.1$; however, this creates a cluster with only 18 members, an order of magnitude fewer than any other cluster. I choose to reselect for 9

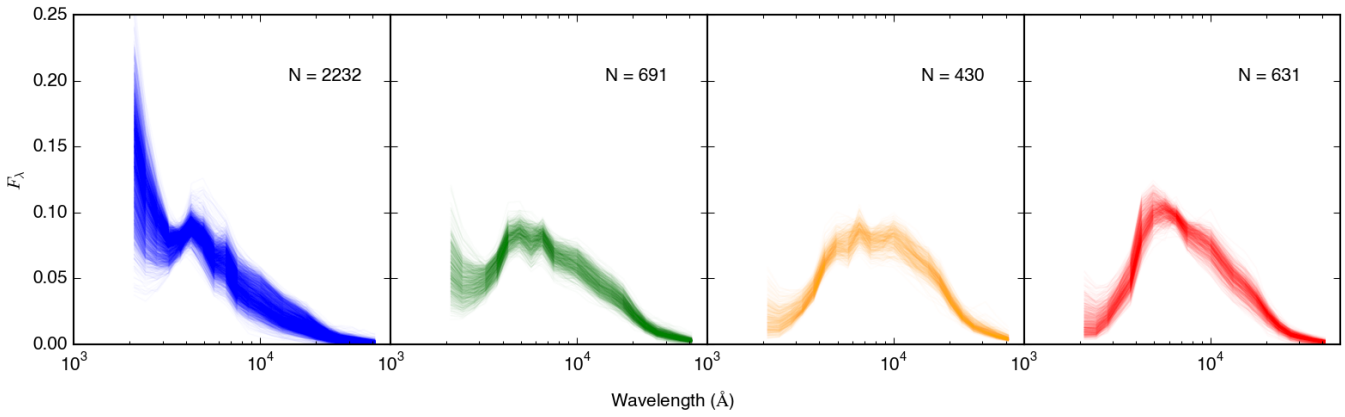

Figure 2.7: PCA composite SEDs. The composite SEDs from the PCA grouping colored by group from Figure 2.6, from Group 1 on the left to Group 4 on the right.

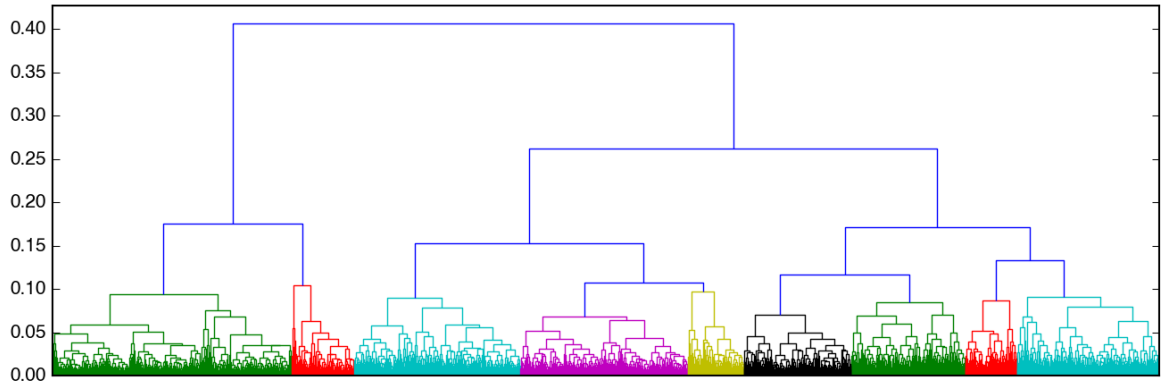

Figure 2.8: HAC dendrogram clusters. Dendrogram showing the entire clustering process for our revised guess of 9 clusters. For reference, the tenth cluster was formed by splitting the left-most red cluster.

clusters, effectively merging this small cluster with its nearest neighbor. The results are shown shown colored in Figure 2.8 and with populations in Figure 2.9.

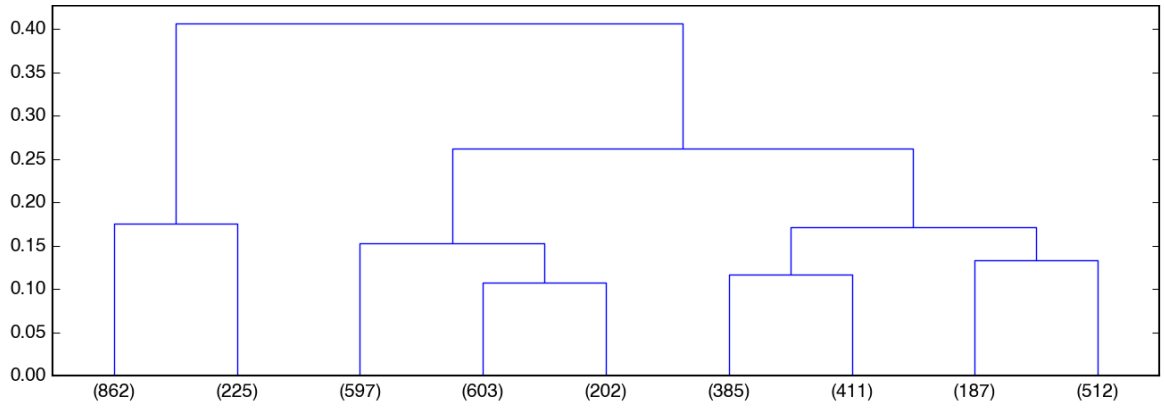

Figure 2.9: HAC dendrogram numbers. Dendrogram showing the number of galaxies in each of 9 clusters. For reference, the tenth cluster split to second cluster from the left into two clusters, one of 207 galaxies and one of 18 galaxies.

The photometry of the galaxies in each cluster are then scaled and plotted together, both for the synthetic photometry (Figure 2.10), and the observed photometry (Figure 2.11).

Both of the above methods split the sample into reasonable groups. While the population as a

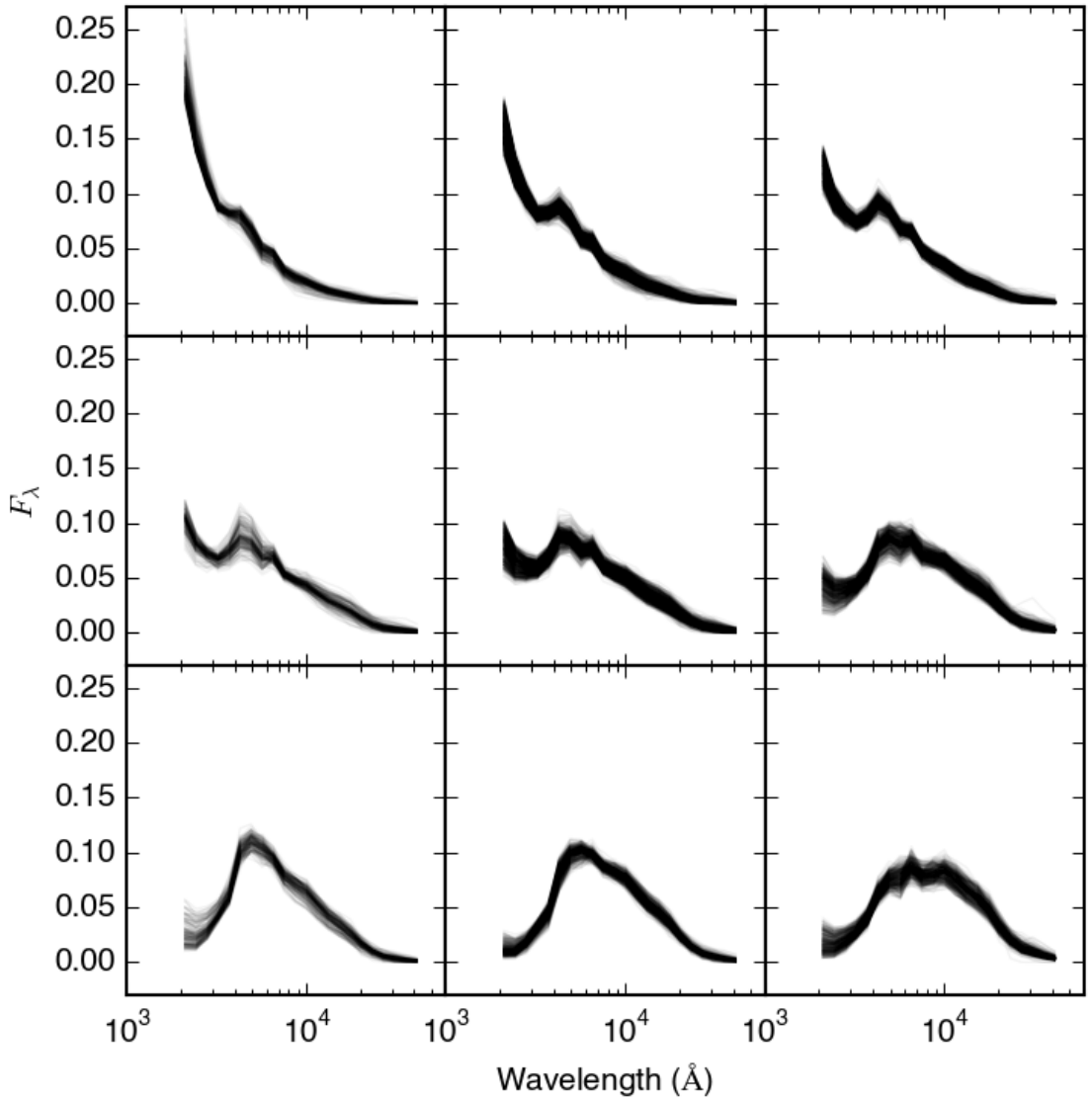

Figure 2.10: HAC rest-frame synthetic photometry. The scaled rest-frame photometry of galaxies grouped into 9 clusters based on HAC.

whole is certainly more of a continuum than discrete clusters, there are SED shapes with a higher rate of occurrence (star-forming) than others (quiescent). This is related to the amount of time a galaxy spends in a particular stage during its evolution from a star-forming galaxy (top row of Figures 2.10 & 2.11).

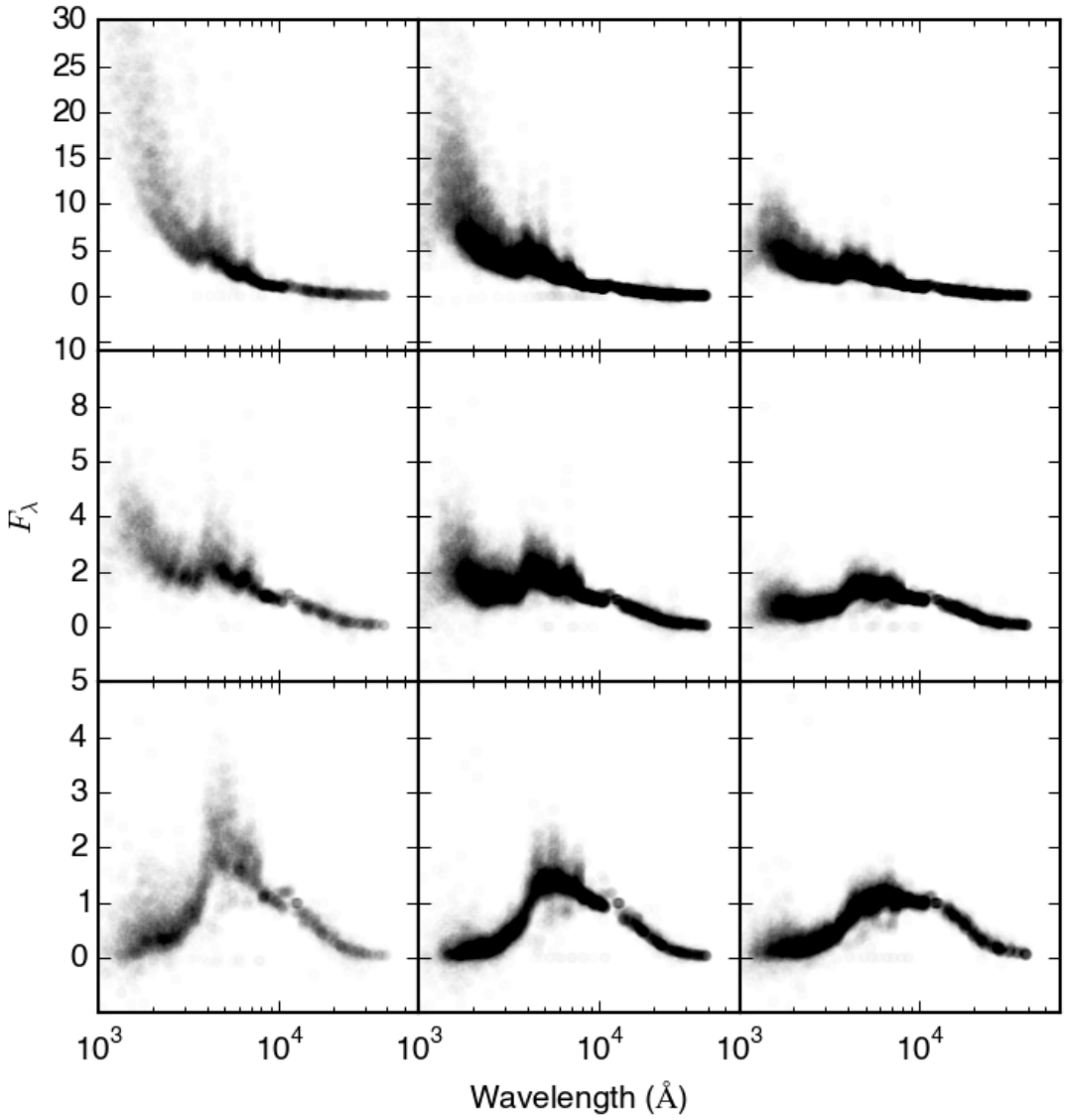

Figure 2.11: HAC composite SEDs. The de-redshifted and scaled observed photometry of galaxies grouped into 9 clusters. The different rows have different limits on the y-axis for clarity.

2.4.3 Local Linear Embedding

The local linear embedding (LLE) technique seeks to reduce the dimensionality of multidimensional data based on the relationships between the data points (e.g. Roweis & Saul, 2000). The algorithm examines each data point individually, searching for its k nearest neighbors. The neighbors are chosen based on the minimum Euclidean distance between respective dimensions of

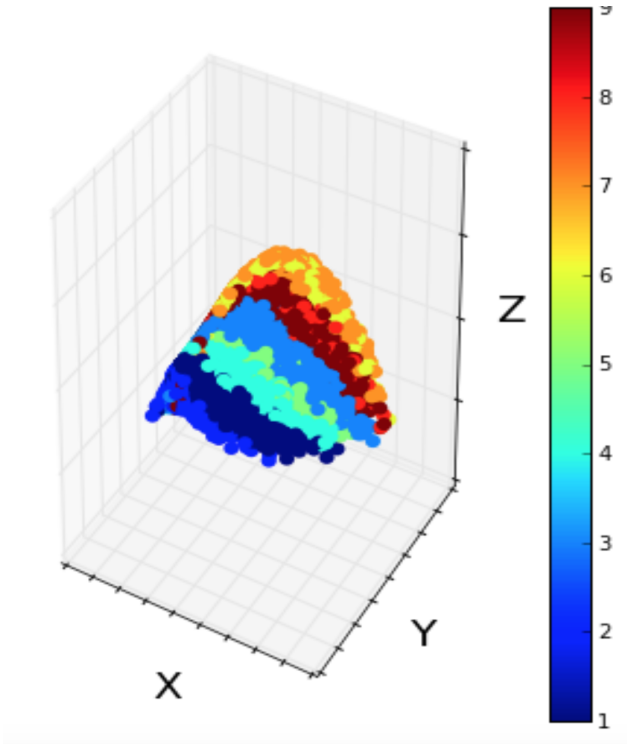

Figure 2.12: LLE surface. 3-D representation after removing outliers.

the data point in question and the possible neighbor. Once the nearest neighbors are determined for a given data point, a weight vector is calculated that assigns statistical weights to the neighboring data points based on their proximity (the closest one is weighted the heaviest, non-nearest neighbors receive a weight of 0, etc). These vectors essentially record the data point's location in terms of the positions of its closest neighbors.

Said weight vectors are then combined into one NxM matrix, where N is the number of data points and M is the number of dimensions each data point has. In this case, each 'point' is a galaxy, and $M = 22$, the number of synthetic rest-frame photometric dimensions. This global weight matrix can be multiplied by a new set of lower dimensional unit vectors to map the data's locations to a lower dimensional coordinate system. In this way, each data point is plotted near other data points to which it is the most similar. The physical locations of the data points on the new coordinate system are directly related to the characteristics of the data. Closely clustered data points will be the most similar while more distant points will be different. This method is described

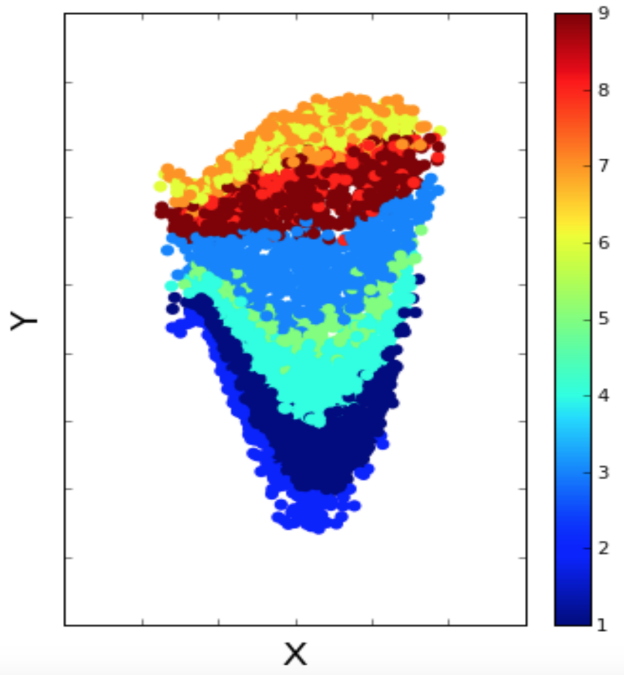

Figure 2.13: An alternative view of the LLE surface. Top-view of the previous 3-d representation.

in Vanderplas & Connolly (2009).

The parameters to choose in this algorithm are the number of neighbors and the dimension in which you want the representation to be. After doing a grid search over a number of neighbors ranging from $20 - 160$, 60 was chosen as the optimal number of neighbors. The initial result has some outliers from the main surface, which is initially concerning, as LLE is known to be fairly sensitive to noise, and thus the outliers could be skewing the results. However, rerunning the algorithm after removing these points does not change our results, which are plotted in Figures 2.12 & 2.13. The different colors on the plot represent the 9 different clusters identified by the hierarchal clustering method explained above. These clusters form distinct bands on the LLE surface, showing that the two methods produce consistent results. Thus a new point can effectively be classified by finding its position on this low dimensional representation.

To make a physical relation to the different regions on this low dimensional representation, we plotted the synthetic photometry for the one point from each colored cluster on the above surface. However, as one can observe the photometry for some clusters look quite identical. This fact can

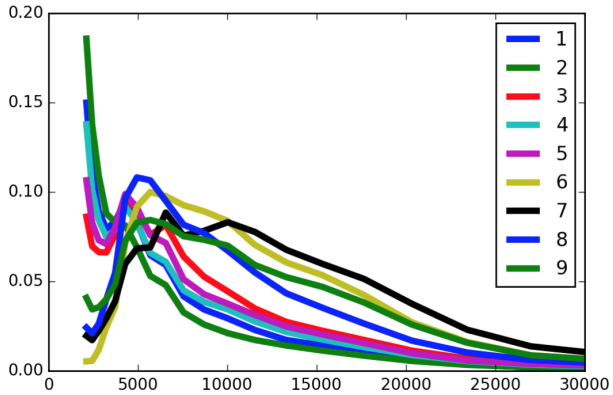

Figure 2.14: LLE composite SEDs. Median de-redshifted rest-frame synthetic photometry for each of the clusters on the surface of LLE.

also be seen as manifested in the very close and (sometimes intertwined) colors on the surface of the LLE. So we tried to combine some clusters based on their positioning on the LLE surface and see if their photometry was kind of same and then if we had much difference between these new clusters.

We have now 4 new clusters : a) 1,2 b) 3 c) 4,5 d) 6,7,8,9 As can be seen from the figures, by combining some of the clusters from the clustering algorithm based on their position on the LLE surface we can identify more physical clusters in the data. These new clusters have much similarity between the original clusters grouped in them, and quite variation among themselves. We can also map known classes of galaxies from another classification algorithm or astronomical literature insight on the LLE surface which can then act as a very good visual representation of all our data.

3. TRACKING GALAXIES IN TRANSITION AT $1 < z < 4$

3.1 Synopsis

We use ~ 7000 galaxies from ZFOURGE with precise photometric redshifts to generate composite spectral energy distributions (SEDs) over two redshift ranges, $1 < z < 3$ and $2.5 < z < 4.0$, based on the shape of galaxy spectral energy distributions from intermediate-band multi-wavelength photometry. These composite SEDs show a variety of spectral shapes and also show trends in parameters such as color, mass, star formation rate, and emission line equivalent width. Using emission line equivalent widths and *D*(4000), we classify the composite SEDs into five categories: extreme emission line, star-forming, transitioning, post-starburst, and quiescent galaxies. The most extreme line emitters have characteristic [O III]+Hβ equivalent widths of $EW_{\rm REST} > 1000$Å. Meanwhile, the transitioning population of galaxies show modest Hα emission compared to more typical star-forming composite SEDs at $\log_{10}(M/M_{\odot}) \sim 10.5$ ($EW_{\rm REST} \sim 40$Å vs. 80Å). They also have redder colors due to dust ($\beta \sim -0.3$ vs. -1.5 and $A_V \sim 0.7$ mag vs. 1.7 mag), smaller sizes (3 kpc vs. 4 kpc), and higher Sérsic indices (2.7 vs. 1.5). These relations confirm that this 'green valley' population represents a stage of galaxy evolution during which star formation is being turned off that differs from the more well-known post-starburst stage ($EW_{\rm REST} < 5$Å, $\beta \sim 1$, $A_V \sim 0.3$ mag, r_e/kpc ~ 1.5, and $n \sim 3.8$ at similar masses). The transitional group shows a strong increase of over one dex in number density from $z \sim 3$ to $z \sim 1$, similar to the growth in the quiescent population, while post-starburst galaxies become rarer at $z \lesssim 1.75$. We conclude that a fast quenching mechanism found in post-starbursts dominated the quenching of galaxies at early times, while a slower process has become more common in the last 10 Gyr.

3.2 Background Information

Since the beginning of the millennium, the number of galaxies with multi-wavelength photometric observations and accurate redshifts has exploded. A wide range of surveys including the Sloan Digital Sky Survey (Abazajian et al., 2003), the NEWFIRM Medium Band Survey (van

Dokkum et al., 2009), *3D-HST* (van Dokkum et al., 2011), the Cosmic Assembly Near-Infrared Deep Extragalactic Legacy Survey (*CANDELS*; Koekemoer et al., 2011), and the FourStar Galaxy Evolution Survey (ZFOURGE; Straatman et al., 2016) have increased our knowledge of galaxy formation and evolution tremendously. With upcoming facilities such as LSST, we will soon truly be in an era where analyzing each individual galaxy is impossible (if we are not already there). Grouping galaxies together based on their similarities will become an important piece of understanding the lifecycles of galaxies through cosmic time.

Previous studies have grouped galaxies together in a variety of ways. Often galaxies with similar values of a given parameter e.g., mass, star formation rate (SFR), Sérsic index, radius, rest-frame color, emission line strength, or infrared (IR) luminosity, will be analyzed together, and all such categorizations can tease out important pieces of information (e.g., Shapley et al., 2003; Brinchmann et al., 2008; Nakajima & Ouchi, 2014; Eales et al., 2017, 2018). Perhaps most prevalent in extragalactic studies, plotting the rest-frame colors *(U-V)* and *(V-J)* against one another has been used to classify galaxies into star-forming or quiescent regimes and approximate dust content (e.g., Labbé et al., 2005; Wuyts et al., 2007; Williams et al., 2009; Whitaker et al., 2011; Brammer et al., 2011; Patel et al., 2012). More recently, other trends in this *UVJ* diagram have been noticed, such as a trend with specific SFR that has been observed for high redshift populations (e.g., Straatman et al., 2016).

More statistically robust methods have also been utilized for grouping galaxies, including local linear embedding (Vanderplas & Connolly, 2009), principal components analysis (PCA, Wild et al., 2014; Maltby et al., 2016), and composite SED construction (Kriek et al., 2011; Yano et al., 2016; Forrest et al., 2016, 2017). Using medium-band and broadband filters to construct these composite SEDs allows for impressive sensitivity and sample size. At the same time, this method enables analysis of emission lines and discriminates more clearly between stellar populations than is typically possible without spectroscopic data.

In this work, we use composite SEDs and spectral diagnostics from said composite SEDs to classify galaxies and show that this classification scheme accurately picks out rare populations,

as supported by other properties and scaling relations. This includes galaxies with strong nebular emission lines (Emission Line Galaxies - ELG), as well as galaxies transitioning from star-forming (SFG) to quiescent (QG) regimes, which we split into two groups based on Hα emission - post-starburst galaxies (PSB; without) and transitional galaxies (TG; with).

PSBs have been a historically rare population, and have been studied in small numbers for some time (e.g., Couch & Sharples, 1987; Tran et al., 2003, 2004; Poggianti et al., 2009). Such galaxies have recently undergone a period of strong star formation, which has stopped within the last several hundred million years. As a result, their spectra are dominated by main sequence A stars with significant Balmer absorption, and have thus also been known as E+A or k+A galaxies (e.g., Dressler & Gunn, 1983).

While analysis of these galaxies potentially allows insight into the mechanisms by which galaxies cease forming stars, such galaxies generally require spectroscopic confirmation, further preventing large samples from being found, particularly at higher redshifts. Additionally, it is not clear that all galaxies undergo such a phase, as the mechanisms behind the quenching of galaxies are still uncertain, and may vary (Tran et al., 2003; Wilkinson et al., 2017). The timescale for which galaxies remain in this post-starburst state is thought to be on the order of 10^8 years (e.g. Wild et al., 2016), and may be dependent upon environment (e.g., Tran et al., 2003, 2004; Poggianti et al., 2009).

As this timescale is relatively short, finding such galaxies is somewhat challenging, and several methods have been used to more easily identify these objects. Whitaker et al. (2012b) use *UVJ* selection and single stellar population models, while other recent works such as Wild et al. (2014, 2016) have used principal components analysis (PCA) for identifying post-starburst galaxies from multi-wavelength photometry alone. Spectroscopic follow-up of these objects (Maltby et al., 2016) have shown a high success rate for this method.

Alternative pathways to quenching are also suggested by the population of non-PSB galaxies in what has come to be called the 'green valley' introduced in Martin et al. (2007); Salim et al. (2007); Schiminovich et al. (2007); Wyder et al. (2007) - in this work we term these transitional galaxies

(TGs). Originally selected to be between the star-forming sequence and quenched population the color-magnitude diagram, similar galaxies have been selected based on relations between colors, stellar masses, stellar mass surface densities, and SFRs (e.g., Mendez et al., 2011; Fang et al., 2013; Schawinski et al., 2014; Pandya et al., 2017). Studies have hypothesized different quenching routes that galaxies may take before shutting off star formation permanently, including the idea of rejuvenation, in which a galaxy stops and restarts star formation multiple times (e.g., Darvish et al., 2016; Pandya et al., 2017; Nelson et al., 2017; Davé et al., 2017).

In Section 3.3 we describe our sample and in Section 3.4 we detail our construction of composite SEDs. Section 3.5 relays our measurements based on the composite SEDs, as well as parameters from the individual galaxies themselves. We then present our composite SEDs in terms of spectral features from the composite SEDs and analysis of the photometry of individual galaxies (Sections 3.6 & 3.7, respectively). Discussion of the TGs (Section 3.8) follows. The entire set of composite SEDs and associated parameters are presented in the Appendix. Throughout the work we assume a cosmology with $H_0 = 70$ km s^{-1} Mpc^{-1}, $\Omega_m = 0.3$, and $\Omega_\Lambda = 0.7$ and make use of the AB magnitude system.

3.3 Data

We use multi-wavelength photometry from the FourStar Galaxy Evolution Survey (ZFOURGE; Straatman et al., 2016) in our work. This survey obtained deep near-IR imaging with the `FourStar` imager (Persson et al., 2013) of three legacy fields: CDFS (Giacconi et al., 2002), COSMOS (Scoville et al., 2007), and UDS (Lawrence et al., 2007). Straatman et al. (2016) combines K-band imaging data from a number of surveys (Retzlaff et al., 2010; Hsieh et al., 2012; McCracken et al., 2012; Fontana et al., 2014; Almaini et al., 2017) to create deep mosaics used as the detection images for these catalogs (see Section 2.3 of Straatman et al., 2016, for details). Morphological data for ZFOURGE galaxies cross-matched with *CANDELS* data from van der Wel et al. (2012) are also included.

In addition to these data, multi-wavelength data from a variety of sources were included in a set of publicly released catalogs (Giavalisco et al., 2004; Erben et al., 2005; Hildebrandt et al., 2006;

Taniguchi et al., 2007; Furusawa et al., 2008; Wuyts et al., 2008; Erben et al., 2009; Hildebrandt et al., 2009; Nonino et al., 2009; Cardamone et al., 2010; Grogin et al., 2011; Koekemoer et al., 2011; Windhorst et al., 2011; Brammer et al., 2012). The CDFS, COSMOS, and UDS fields have 40, 37, and 26 filter bandpass observations ranging from 0.3-8 μm with 80% completeness limits of 26.0, 25.5, and 25.8 AB magnitudes in the stacked K_s band, respectively (Straatman et al., 2016). These catalogs are particularly well suited to the composite SED method due to their accurate photometric redshifts ($1-2\%$; Nanayakkara et al., 2016), broad range of rest-frame wavelengths, and deep imaging which allows for inclusion of faint galaxies at high redshifts.

3.4 Composite SED Construction

3.4.1 Sample Selection

The construction of composite SEDs requires grouping galaxies together based on SED shape, as determined from multi-wavelength photometry. This method is based on the work presented in Kriek et al. (2011), with minor changes made in Forrest et al. (2016) and Forrest et al. (2017).

We begin by selecting a sample over some redshift range, based on Easy and Accurate $z_{\rm phot}$ from Yale (EAZY; Brammer et al., 2008) outputs included in the ZFOURGE catalogs (Straatman et al., 2016). EAZY fits linear combinations of sets of input galaxy spectral templates to photometry allowing calculation of photometric redshifts and rest-frame colors. Combined with the medium-bands of ZFOURGE, this yields precise photometric redshifts, which are necessary to minimize scatter in the resulting composite SEDs.

Since we only compare photometry observed at similar rest-frame wavelengths between galaxies, it is important that this redshift range is not too wide, otherwise galaxies may be artificially grouped together based on only a few photometric observations. On the other hand, the strength of the composite SED method is only realized when different redshifts are used. Grouping galaxies over a narrow redshift range does not improve sampling of the rest-frame wavelengths over observations of an individual galaxy. Kriek et al. (2011) used a redshift range of $0.5 < z < 2.0$, Forrest et al. (2016) required $1.0 < z < 3.0$ and Forrest et al. (2017) was based on composite SEDs from

galaxies in the range $2.5 < z < 4.0$. We regenerate composite SEDs from the latter two redshift ranges using an updated set of catalogs.

The signal to noise cut for our selection is $SNR_{K_s} > 20$. In general this limits the galaxies in the sample to those which have well-defined SEDs through accurate photometry. Combined with the similarity index described below, this ensures that duplicates of a galaxy will be grouped together within the noise limit. Finally, we eliminates stars and other contaminants by requiring the catalog flag `use=1`, and remove X-ray selected, IR selected, and radio selected active galactic nuclei (AGN) hosts as identified in Cowley et al. (2016). These cuts produce 7351 galaxies in $1 < z < 3$ and 1294 galaxies in $2.5 < z < 4$.

3.4.2 Composite SEDs at $2.5 < z < 4.0$

The ZFOURGE catalogs have 1294 galaxies at $2.5 < z < 4.0$ with the requisite SNR, use flag, and non-AGN identifiers. Of these, 940 (72.6%) are placed into 16 groups based on SED similarity. The resulting composite SEDs are comprised entirely of blue galaxies, none of which are particularly dusty. An analysis of the sample shows that there are in fact a small number of dusty star-forming galaxies as well as quiescent galaxies (based on position in the *UVJ* diagram). However, their SED shapes are different enough to not be grouped together using the above method. For these populations we increase the b-parameter cutoff to $b < 0.15$ to recover 2 quiescent groups and 2 dusty star-forming groups, all of which show slightly more scatter than our blue composite SEDs. In total we therefore have 20 composite SEDs comprised of 1037 galaxies (80.1% of the sample that passed our cuts).

The 90% mass completeness of ZFOURGE at $z = 3$ is $\log_{10}(M_{90}/M_{\odot}) \sim 10$ (Tomczak et al., 2016). However, there are a number of galaxies with strong [O III] and Hβ emission in our detection bandpass, K_s. We therefore are sensitive to objects with particularly strong emission from these lines at lower masses than those galaxies without this emission.

The method used to generate these composite SEDs has small methodological changes to that used in Forrest et al. (2017). These changes allow inclusion of a larger number of galaxies in the composite SEDs. The Extreme and Strong Emission Line Galaxies from Forrest et al. (2017)

are now split into several composite SEDs, the differences largely driven by the amount of UV luminosity in a galaxy.

3.4.3 Rebuilding Composite SEDs from Forrest et al. (2016)

The composite SEDs presented in Forrest et al. (2016) used an earlier, internally circulated version of the ZFOURGE catalogs. This version did not use the same deep stacked K_s-band detection image, and thus was limited to 3984 galaxies in the $1 < z < 3$ sample. This sample also met the other requirements above, namely having $SNR_{K_s} > 20$ and `use=1`. For consistency with the new composite SEDs constructed here, we also rebuild composite SEDs at $1 < z < 3$ using the publicly released catalogs. Using the updated catalogs, we obtain 7351 galaxies with the same criteria. The resulting 71 composite SEDs have 6314 galaxies, or 85.9% of the original sample. We do not perform regrouping of quiescent and dusty star-forming galaxies as several composite SEDs have already been built at these redshifts. One of the groups with fewer than 19 galaxies is also of interest however, as it contains 14 galaxies with very blue colors and strong emission features, consistent with the emission line galaxies seen in the higher redshift sample. We thus include this composite SED in our following analysis. ZFOURGE completeness is $\log_{10}(M_{90}/M_{\odot}) \sim 9$ at $z = 1.5$ (Tomczak et al., 2016), and 524 (8.3%) galaxies in our $1 < z < 3$ sample are less massive than this.

Between the two sets of composite SEDs, there are 6921 total galaxies, i.e., there are 444 galaxies which fall in the redshift range $2.5 < z < 3$ and are in composite groups in both regimes.

3.5 Measuring Individual Galaxy and Composite SED Properties

In this Section we discuss the measurement of quantities which are used in our analysis (Section 3.6 and Section 3.7). For our analysis of the composite SEDs, we consider both the properties of the analog galaxies and the properties of the composite SED itself. When composite SED 'fluxes' are described, these values are scaled due to the construction method of the composite SED. As a result, these can only be used validly as part of a color.

3.5.1 *Rest-frame colors*

We consider the *UVJ* diagram in our analysis. Rest-frame fluxes for analog galaxies are taken from the ZFOURGE data release. These values are calculated using EAZY and the nine different galaxy templates mentioned above. We use this same method with our composite SEDs and their custom filter curves to generate rest-frame colors for each composite SED.

3.5.2 *Using Emission Line Templates with FAST*

As shown in previous work, failure to account for emission lines when fitting templates to galaxy photometry can lead to severe errors in parameter estimation (e.g., Stark et al., 2013; Salmon et al., 2015; Forrest et al., 2017). We therefore refit all of the galaxies in our sample using FAST (Kriek et al., 2011) and a series of models from Bruzual & Charlot (2003) (BC03) with emission lines added.

These emission lines are based on modeling done with CLOUDY (Ferland et al., 1998), with methods from Inoue (2011) and Salmon et al. (2015). Briefly, the ionization parameter, metallicity, and density of hydrogen is varied to produce sets of emission line ratios from Lyman-α to 1 μm. These emission lines are added to the BC03 high resolution models and are used in our FAST runs.

We refit all galaxies in our composite SED samples with this set of emission line models, allowing other parameters to range as in the ZFOURGE catalogs. The resulting fits are checked to ensure that no galaxy is assigned an age greater than the age of the universe at the corresponding photometric redshift.

The differences from these new fits and the ZFOURGE results are non-negligible, showing two populations (see Figure 3.1). The first population consists of galaxies with emission lines, for which models sans emission lines overestimate the mass by 0.75 ± 0.12 dex at $\log_{10}(M/M_{\odot}) \sim 8.5$, decreasing to agreement at $\log_{10}(M/M_{\odot}) \sim 10.5$. These galaxies also show SFR underestimates of 0.92 ± 0.35 dex at $\log_{10}(M/M_{\odot}) \sim 8.5$. The second population shows little effect due to emission lines and has consistent masses over $9 < \log_{10}(M/M_{\odot}) < 11.5$, as well as SFR within half a dex over the same mass range. On average, this second population is higher mass, whose

greater stellar continuum reduces the effects of any nebular emission lines on SED fitting.

The SFR values have quite large offsets between the two methods, up to one dex at low masses, due to the change in the fit stellar continuum and emission lines. While the bottom panel of Figure 3.1 also shows differences in SFR for galaxies at $\log_{10}(M/M_{\odot}) \sim 9.5$, the histogram to the left reveals that this is actually a small fraction of the population. Additionally, our composite SED method uses averages of groups of galaxies, and thus the effects of the extreme scatter are mitigated in this work.

The composite SEDs are also fit with FAST. Similar to fluxes, the output masses and SFRs are scaled to unphysical values, although properties such as sSFR, age, and dust attenuation (A_V) are unaffected. For such affected properties, we use the median of the analog population as a characteristic value for the composite SEDs.

3.5.3 UV Slope

We fit a power law to the composite SED points within the wavelength range $1250 < \lambda/\text{Å} < 2600$, $F \propto \lambda^{\beta}$ to obtain the UV slope, β. This effectively prevents contamination from Lyman-α emission. We also masked around the 2175Å dust feature and refit the power law. For the vast majority of composite SEDs this makes no difference to the fit. In the several cases which show clear attenuation at this wavelength, we mask points over $2000 < \lambda/\text{Å} < 2350$ and use the resultant exponent.

3.5.4 D(4000)

The 4000 Ångstrom break (*D*(4000)) is defined in Bruzual A. (1983) as

$$D(4000) = \frac{(\lambda^2_{blue} - \lambda^1_{blue}) \int_{\lambda^1_{red}}^{\lambda^2_{red}} f_\nu d\lambda}{(\lambda^2_{red} - \lambda^1_{red}) \int_{\lambda^1_{blue}}^{\lambda^2_{blue}} f_\nu d\lambda}, \tag{3.1}$$

with $(\lambda^1_{blue}, \lambda^2_{blue}, \lambda^1_{red}, \lambda^2_{red}) = (3750, 3950, 4050, 4250)$ Å. Given the limited resolution of our composite SEDs, these integrals generally correspond to two points on either side of the break, but are still well constrained.

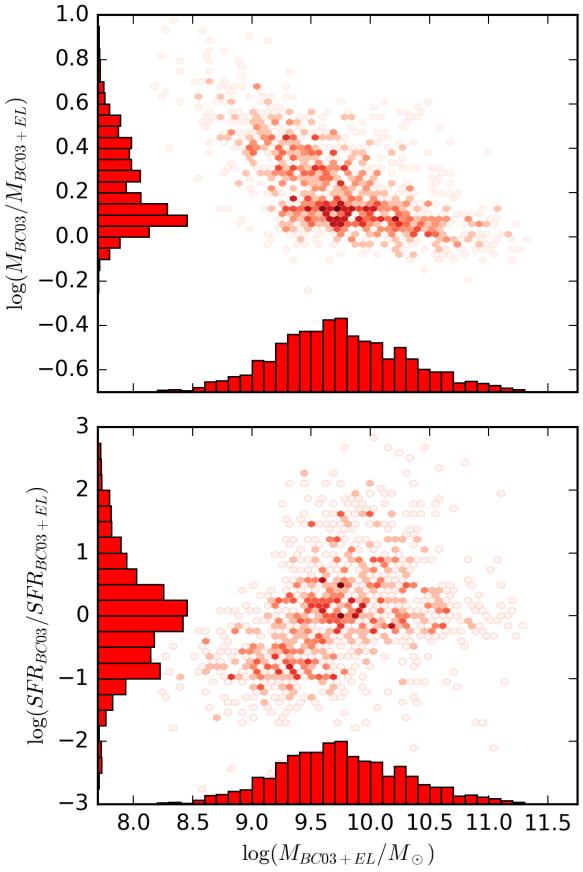

Figure 3.1: Differences in parameters fit with FAST due to the inclusion of emission lines. *Top:* The masses of low mass galaxies are significantly overestimated if the effects of strong emission lines are not accounted for. *Bottom:* These emission lines also increase the star formation rates of the best fit models.

Several of the ELG composite SEDs have $D(4000) < 1$, indicating stellar populations dominated by light from young, massive O stars (e.g., Poggianti & Barbaro, 1997). Errors are determined by calculating $D(4000)$ using the 1σ flux values for the composite SED points. As detailed in Appendix C of Kriek et al. (2011), our photometric redshift errors are sufficiently small such that they will not effect this measurement.

3.5.5 Equivalent Widths

We measure the rest-frame equivalent width of [OIII]λ5007,4959+H$\beta\lambda$4861 for all of our composite SEDs and Hα+[NII]+[SII] for our $1 < z < 3$ composite SEDs. For the $2.5 < z < 4.0$

sample, the Hα+[NII]+[SII] line blend falls between the K_s-band and the *IRAC* 3.6 μm filter, and will therefore not be observable until the *James Webb Space Telescope* (*JWST*) is taking data. To measure the equivalent widths of these line blends, we use the best fit SEDs from FAST models with emission lines, as described above. We remove the emission lines from these best-fit SEDs to obtain the stellar continuum, and convolve this with the custom composite SED filters to obtain synthetic photometry of the continuum. The composite SED is then normalized by this synthetic photometry.

We measure the equivalent width in several ways, two of which are shown in Figure 3.2. First, we perform a simple trapezoidal integration under the continuum normalized composite SED in the area of interest

$$EW_{\text{[OIII] }blend} = \int_{4361}^{5507} (1 - f_\lambda / f_c) d\lambda \tag{3.2}$$

$$EW_{H\alpha\, blend} = \int_{5763}^{7363} (1 - f_\lambda / f_c) d\lambda, \tag{3.3}$$

where f_λ is the composite SED flux and f_c is the continuum flux from the best fit SED. We note that the composite SED points themselves must be within these limits and therefore are nominally in a narrower wavelength regime. However, since the custom composite SED filters are fairly broad, signals outside of these wavelength limits are in fact being probed. This would be the case even if a single composite SED point were used.

In addition, we fit a Gaussian profile to the continuum normalized composite SED and integrate under that curve. The results are generally similar to within 10%. However in some cases, the composite SED points have spacing which yields a discrepancy between the two methods, as can be seen with the Hα emission in Figure 3.2. In these cases, the fits were visually inspected, and in all such cases the Gaussian profile fit was judged to be superior.

For blends of multiple lines, such as [OIII]λ5007,4959 + H$\beta\lambda$4861, we also attempted fitting multiple Gaussian curves, one to each line. Forcing the center of each Gaussian profile to be at the emission wavelength provides a good overall fit to the data, but the individual curves

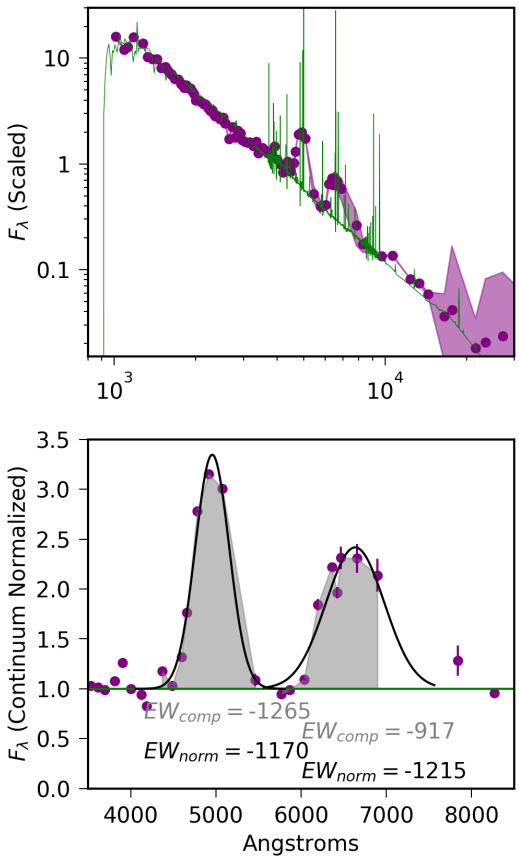

Figure 3.2: Sample equivalent width fit. *Top:* The composite SED from galaxies at $1 < z < 3$ with the largest measured emission line equivalent widths. The median composite SED points and associated errors on medians are shown in purple. The best fit emission line SED is in green. *Bottom:* The continuum normalized flux of the composite SED points showing [O III]+Hβ and Hα emission. The black curves show fits of Gaussian profiles to the emission line blends, while the gray shading shows a simple trapezoidal integration to obtain the equivalent width. In general these two methods agree within 10%, although in cases of extreme emission such as this, the selection of points for trapezoidal integration is an important factor and can lead to larger discrepancies. Throughout this work, we quote equivalent widths from the Gaussian curve fits.

are often unphysical, usually showing strong absorption in one Gaussian profile and strong emission in another. Further constraining this multi-Gaussian profile fit by forcing a line ratio, e.g., [OIII]λ5007/[OIII]λ4959=3, generally results in fitting absorption for Hβ, which we take to be unphysical as well given the large Hα EWs. The overall fits are again good, and very similar to the fit of the single Gaussian curve above. Equivalent widths measured from the Gaussian profiles are in both cases within a few percent of the single curve fit. The broadness of the custom

composite SED filters is the cause of this, as we do not accurately resolve out the different lines.

Weak emission is difficult to quantify accurately, especially when the continuum fit is not good or the composite SED is noisy relative to the line. In general, we are confident in emission equivalent widths down to 20Å, and most composite SEDs have [OIII]+Hβ and Hα equivalent widths greater than this.

In the remainder of this paper, referenced equivalent widths will be from the single Gaussian profile fit for each line blend.

3.5.6 Morphology

The ZFOURGE data release includes a catalog of sources cross-matched with the *CANDELS* morphological catalogs of van der Wel et al. (2012). The resolution of the $HST-F160W$ imagery used in these catalogs is 0.13". While at high redshifts this nominally makes fitting small galaxies difficult, van der Wel et al. (2012) find that galaxies with half-light radii of 0.3 pixels are recovered correctly using GALFIT (Peng et al., 2010). There are 31 galaxies in our sample across a range of redshifts and composite SEDs that have fit sizes below this limit - excluding these galaxies make no difference in our results. We compare sizes and Sérsic indices for galaxies of different classifications in Section 3.7.3.

3.6 Spectral Feature Analysis

3.6.1 Composite SED Classification

In this work we classify our composite SEDs which show evidence of star formation by their their *D*(4000), emission line strengths, and dust attenuation (see Figure 3.3). *D*(4000) is a proxy for age (e.g. Poggianti & Barbaro, 1997), while Hα probes the star formation activity for galaxies in a composite SED (e.g., Kennicutt & Evans, 2012). While [OIII] emission is dependent upon abundances, it is also sensitive to ionizing photons from young stars. This selection is therefore independent of the colors and morphologies of the composite SEDs. Nonetheless as described below, we still pick out trends in both parameters based on our classification.

The majority of our composite SEDs have equivalent widths of $EW_{H\alpha} \sim 100$Å and these are

classified as Star Forming Galaxies (SFGs). As this decreases, we see trends toward increasing *D*(4000) and dust attenuation as fit by FAST, in agreement with Figure 8 from Kriek et al. (2011). At low *D*(4000) we see groups with large $EW_{H\alpha}$ (and $EW_{[OIII]+H\beta} > 400$Å), which we classify as Extreme Emission Line Galaxies (ELGs).

While the SFGs have *D*(4000)$\sim 1.3 \pm 0.2$ and $\log_{10}(EW_{H\alpha}/\text{Å}) \sim 2^{+0.5}_{-1}$, several composite SEDs have *D*(4000)> 1.5 and $EW_{H\alpha} < 20$Å. Upon visual inspection, we classify these as either Quiescent Galaxies (QGs) or Post-Starburst Galaxies (PSBs) based on the sharpness of the turnover of the SED around 5000Å(see Figure 3.4).

The composite SEDs constructed from galaxies at $2.5 < z < 4$ lack coverage across wavelengths to which Hα is redshifted - the line falls between the K_s-band and the *IRAC* channels. We again use *D*(4000) and $EW_{[OIII]+H\beta}$ to identify 3 ELG composite SEDs, and use visual identification to compare the others to the low redshift sample. There is less variety seen than at $1 < z < 3$, with 15 of the 19 composite SEDs clearly falling into the star-forming regime, including the two dusty composite SEDs. The remaining two, constructed from *UVJ*-quiescent galaxies show some scatter, but appear most similar to the PSBs from the $1 < z < 3$ sample. While there may be a few older quiescent galaxies in these samples, they are in the minority.

Figure 3.4 shows the optical wavelengths for examples of the different classes. While dusty SFGs, TGs, and QGs all have a plateau in the SED from $0.5-0.7\mu$m, the PSBs have a distinct peak blueward of this, consistent with the populations of A-type stars that helped lead to their original moniker - E+A galaxies.

Because we do not have coverage of Hα for our $2.5 < z < 4.0$ composite SEDs, we compare *D*(4000) and [O III]+Hβ emission lines to the $1 < z < 3$ set of composite SEDs to classify them, using visual inspection when overlap occurs. In what follows, we compare the properties of galaxies in these different classes. On the whole, reassigning a single composite SED to a different class (within reason, i.e., SFG $<->$ TG or PSB $<->$ QG) does not affect our conclusions.

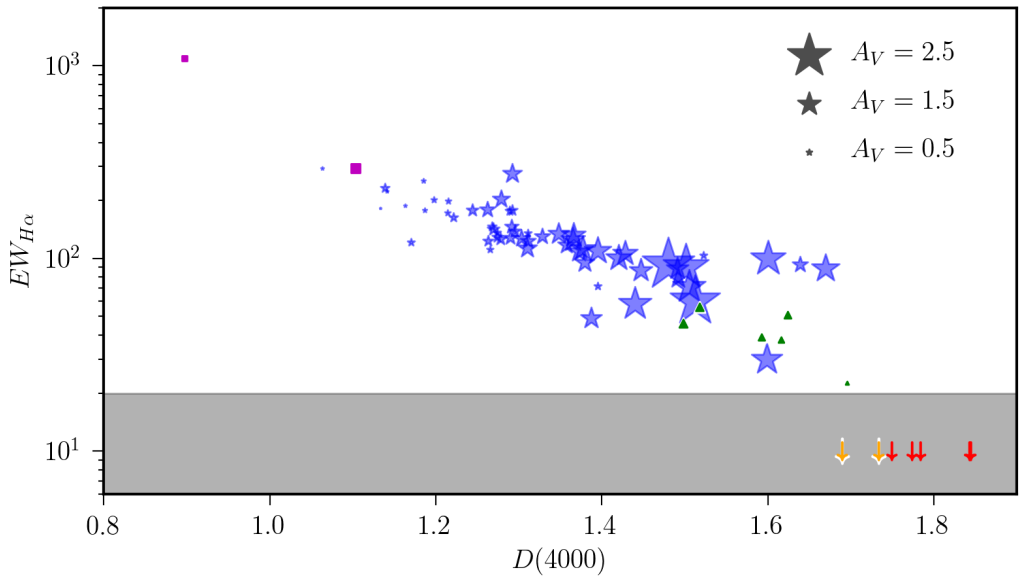

Figure 3.3: Classification method for composite SED populations. Hα $EW_{\rm REST}$ against $D(4000)$ for out $1 < z < 3$ composite SEDs. This is used in concert with the dust attenuation fit using FAST, indicated by marker size, to classify the composite SEDs which show evidence of star formation. Star Forming Galaxy composite SEDs are blue stars, showing a trend toward larger dust attenuation and lower Hα $EW_{\rm REST}$ at higher $D(4000)$. Transition Galaxies (green triangles) show significantly less dust for their $D(4000)$, bucking the trend of the the other star-forming galaxies. Those classified as Extreme Emission Line Galaxies are shown as magenta squares, which have $D(4000) < 1.1$ and $EW_{[OIII]} > 400$Å. Post-Starburst Galaxies (orange), and Quiescent Galaxies (red) are not detected above our noise threshold of 20Å (gray shaded region).

3.6.2 EW-mass

The use of deep narrowband imaging to find emission line galaxies in specific redshift windows has been used for over two decades (e.g., Hu & McMahon, 1996; Cowie & Hu, 1998; Teplitz et al., 1999), notably in the High Redshift Emission Line Survey (HiZELS; Geach et al., 2008). More recently, emission line galaxies have also been identified from flux excesses in broadband filters relative to nearby multi-wavelength photometry (e.g., Fumagalli et al., 2012; Labbé et al., 2013; Stark et al., 2013; Smit et al., 2014). Composite SEDs have been used for emission line galaxy selection as well (Kriek et al., 2011; Forrest et al., 2017).

Using these large numbers of equivalent widths, trends have been found with mass and redshift.

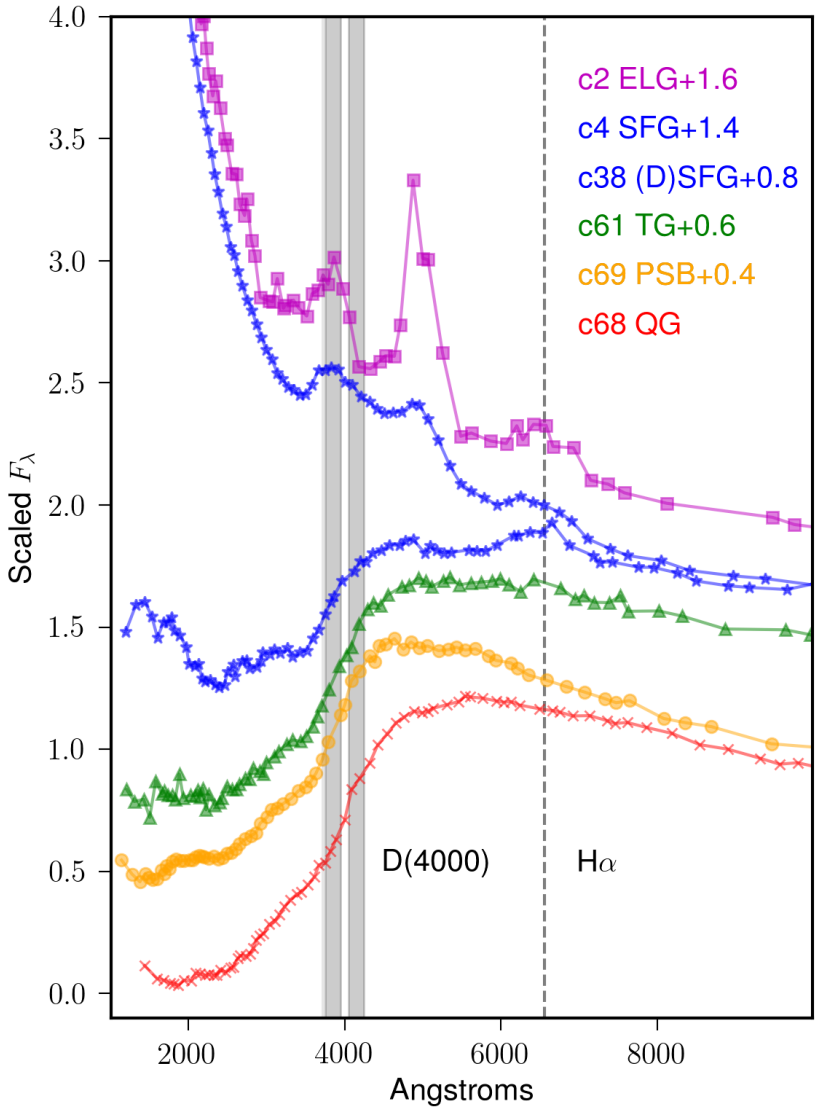

Figure 3.4: Representative optical fluxes of composite SED classes. These are plotted with a vertical offset for clarity. The composite id for reference with the Appendix is given. We are able to discern between the quiescent and post-starburst composite SEDs due to the sharper turnover of the post-starbursts. That is, the spectral peak redward of the 4000Å break is blueward of $\sim$ 4500Å for post-starbursts, while older quiescent populations peak redward of 5000Å. Blue star-forming galaxies and extreme emission line galaxies have considerably more UV-optical flux than any of the other types shown here. Id's given are for reference with data in the Appendix.

Fumagalli et al. (2012) use data from *3D-HST* to trace out Hα+[NII] EW against mass and find that for galaxies of a given mass, EWs are higher at higher redshift. Similarly, Khostovan et al. (2016) (using data from HiZELS) and Smit et al. (2015) (using *Spitzer* data) trace out Hβ+[OIII] EWs against mass, with similar conclusions. Specifically, Hβ+[OIII] EW appears to turn over at $z \sim 2.5$, while [OII] EW peaks around $z \sim 3.5$.

We compare results from our composite SEDs to those of the literature by fitting a line to the logarithm of equivalent width against logarithm of stellar mass, weighted by the number of galaxies in each composite SED. This results in steeper relations for the [O III]+Hβ EWs ($q = -1.03 \pm 0.03$ and $q = -0.93 \pm 0.09$ for $1 < z < 3$ and $2.5 < z < 4$, respectively), than in previous work such as HiZELS ($q = -0.35$; Khostovan et al., 2016). We note that we are not mass complete down to the lowest-mass composite SED and that we have increased sensitivity to luminous objects with high-EW in our high-redshift composite SEDs, possibly elevating the relation.

As a check, we refit only the composite SEDs classified as star-forming. While the fit to the $1 < z < 3$ sample does not change ($q = -1.04 \pm 0.04$), the $2.5 < z < 4$ sample does show a difference ($q = -0.69 \pm 0.13$) as ELGs are more prevalent for this sample. Nonetheless, the relations remain significantly steeper, signifying a more drastic decrease in characteristic EW with increasing mass. Additionally, there is a ~ 0.25 dex offset between our high- and low-redshift relations, the higher redshift sample having a larger EW for a composite SED of a given mass, which is in agreement with the HiZELS work in Khostovan et al. (2016).

In contrast to our results for [O III]+Hβ, the Hα EWs are in good agreement with both Fumagalli et al. (2012) and Sobral et al. (2013) (see Figure 3.5).

Figure 3.5 also shows that the discrepancy between SFG and TG emission line ratios is due to smaller $EW_{H\alpha}$ than SFGs.

The ratio of Hα+[NII] / Hβ+[OIII] EW also varies with Hα+[NII] at $1 < z < 3$. While $EW_{H\alpha}/EW_{[OIII]+H\beta} \sim 3$ for star-forming galaxies with $EW_{H\alpha} \sim 100$Å, this drops down near unity for the more extreme emitters. Unfortunately we are unable to probe Hα+[NII] in our high redshift sample to see if this ratio varies with redshift, but this will be explored by *JWST*.

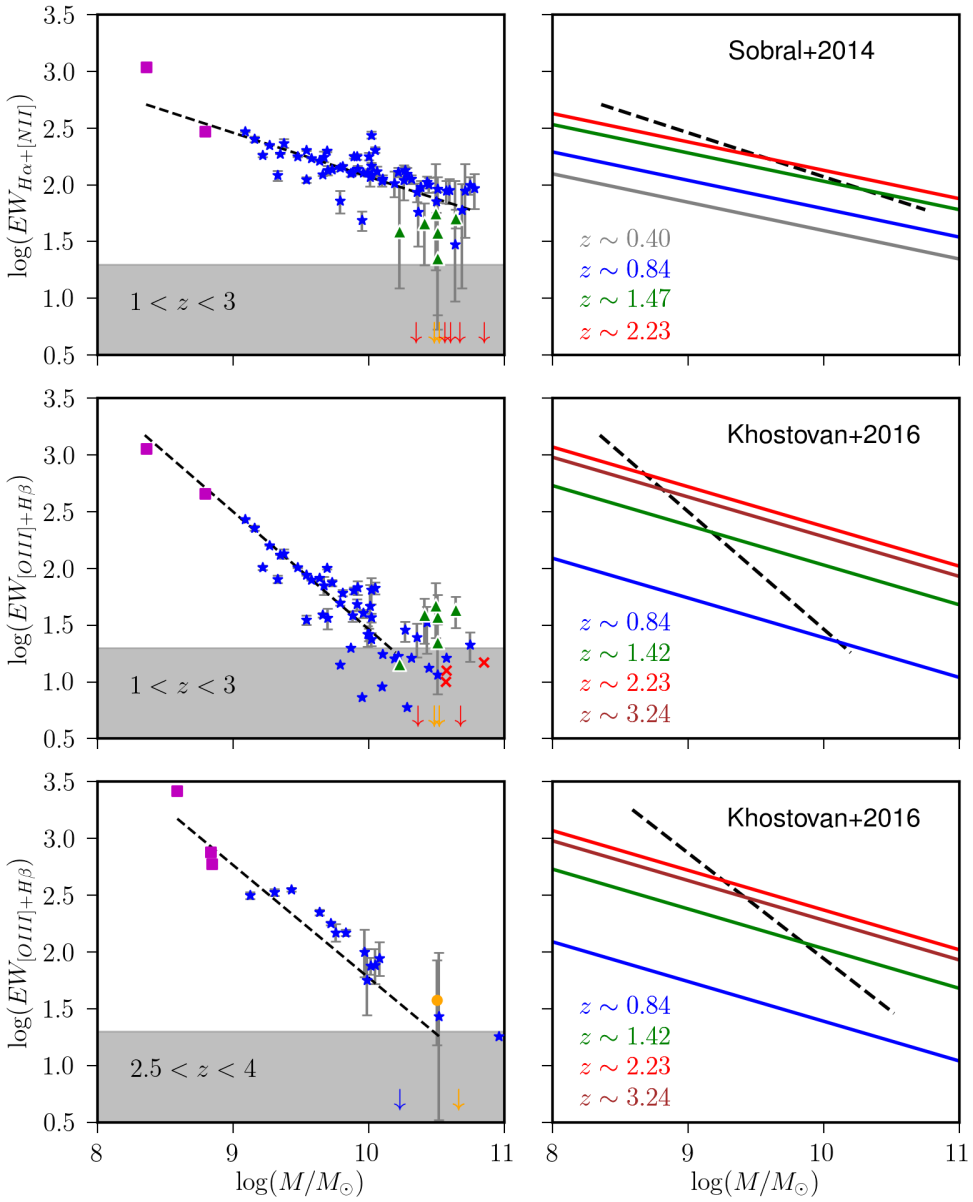

Figure 3.5: The relation between equivalent width and stellar mass. Points are colored according to the classifications scheme shown in previous figures. The gray shaded regions represent $EW <$ 20Å, which we take to be the limit of our sensitivity with the composite SEDs. *Top Left*: Hα+[NII] EW for composite SEDs at $1 < z < 3$. *Middle Left*: [OIII]+Hβ EW for composite SEDs at $1 < z < 3$. *Bottom Left*: [OIII]+Hβ EW for composite SEDs at $2.5 < z < 4$. *Right*: Fits to composite SED EWs shown as black lines, with relations from (Khostovan et al., 2016) (top, middle) and (Sobral et al., 2013) shown as colored lines.

3.7 Photometric Analysis

3.7.1 Color Relations

The composite SEDs are formed based on multi-color comparisons. As such, we would expect the groups to separate into distinct groups on color-color diagrams, the best known of which is the *UVJ* diagram (e.g. Wuyts et al., 2007; Williams et al., 2009; Whitaker et al., 2012b; Straatman et al., 2016; Forrest et al., 2016). There is a spread in the colors of analogs in a given composite SED, and we display these by calculating 1σ error ellipses based on the covariance between the colors, shown in Figure 3.6. As expected, composite SEDs in a given class are mostly separated from other classes, although some of the individual galaxy colors do overlap. This indicates that while the *UVJ* diagram does a good job discerning between a simple red and blue sequence, it does not yield the whole picture that can be obtained by analyzing the full SED of a galaxy. In this picture, the TGs are consistent with galaxies in the green valley and with the transition galaxies of Pandya et al. (2017).

We note that there is reduced diversity in the high-redshift composite SEDs. While some of this is due to the reduced sensitivity to objects with faint stellar continua, this does not explain the lack of quiescent objects, nor the lack of transition objects, as ZFOURGE is mass complete for these samples out to $z \sim 3.5$. This is suggestive that these populations are rarer at high redshifts, which is known to be the case for quiescent objects (e.g., Straatman et al., 2016). Nonetheless, post-starburst galaxies are found here, implying that star formation has been turned off, or at least significantly reduced, as studies have shown that galaxies in this regime of the *UVJ* diagram can still be forming stars, albeit with low sSFR (e.g., Ciesla et al., 2017).

Additionally, the star-forming sequence of the *UVJ* diagram broadens, suggesting a wider range of colors for star forming galaxies at high redshift. While measurement errors may play a small role here, the intrinsic spread is expected to increase due to the presumed bursty nature of star formation in young galaxies (e.g., Papovich et al., 2001; Castellano et al., 2014; Izotov et al., 2016), although uncertainties remain on this front (see, for example, Smit et al., 2015) There are

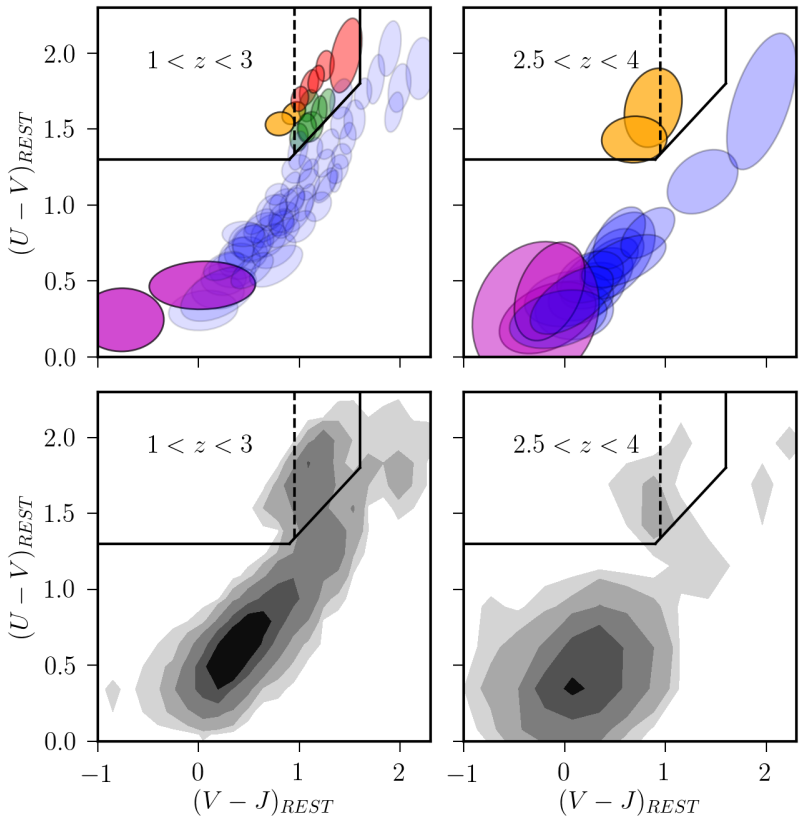

Figure 3.6: The *UVJ* diagram. *Top:* The 1σ error ellipses of our composite SEDs based on analog positions on the *UVJ* diagram. $1 < z < 3$ composite SEDs are on the left, while $2.5 < z < 4$ composite SEDs are on the right. Star-forming composite SEDs are shown in blue, emission line galaxies in magenta, post-starbursts in orange, quiescent composite SEDs in red, and transitional composite SEDs in green. The vertical dashed line is from Whitaker et al. (2012a); Wild et al. (2014) and separates post-starbursts (blueward) from older quiescent galaxies (redward). *Bottom:* Contours of analog galaxies on the *UVJ* diagram. Contours for the $1 < z < 3$ sample are 3, 10, 30, 100, and 300 galaxies, while $2.5 < z < 4$ contours are 3, 8, 22, 60, and 120 galaxies.

also a greater number of galaxies with strong nebular emission falling in the rest-frame V band, which boosts galaxies to particularly blue colors in *(V-J)*.

This classification scheme is also consistent with that determined using a color-mass diagram. We correct the rest-frame *(U-V)* colors using the dust attenuation for a galaxy as described in Brammer et al. (2009) and shown in Figure 3.7. This correction for dust attenuation more closely approximates the intrinsic colors, providing a clearer separation between SFG, TG, PSB, and QG

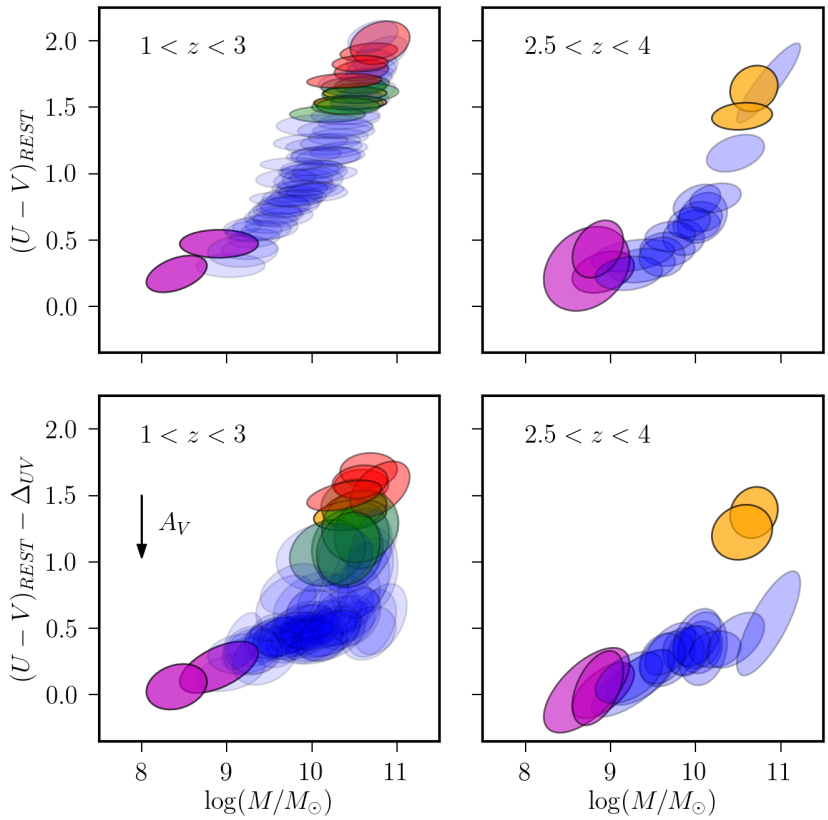

Figure 3.7: Dust corrected *(U-V)* colors. The composite SEDs plotted as 1σ error ellipses of the analogs that comprise that composite SED in *(U-V)*-mass space. The top rows are colors fit using EAZY, while the bottom row is corrected by dust attenuation derived using FAST. The left column is for galaxies in our sample in $1 < z < 3$, while the right column is for galaxies in $2.5 < z < 4$. The dust correction removes many of the star-forming galaxies in the observed green valley.

composite SEDs.

3.7.2 Star Forming Main Sequence

Previous works have also classified galaxies in narrow redshift bins based solely upon sSFR (e.g., Pandya et al., 2017). Figure 3.8 shows the composite SEDs on the sSFR-$M_\odot$ plane. While on the whole different categories do separate out nicely, there exists some overlap between TGs and PSBs in the low redshift set. The sSFRs are lower for the PSBs on average, which is reasonable since they are thought to be almost completely quenched, while TGs are in the process of quenching. However, numerous studies have shown an evolution of SFR (and sSFR) against mass

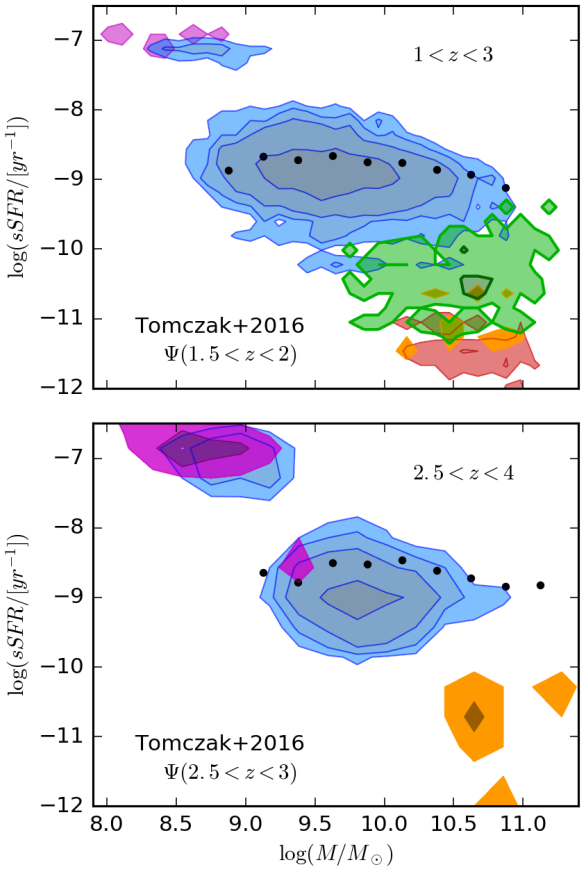

Figure 3.8: The relation between sSFR and stellar mass. The various classes show separation with respect to sSFR. The black points are the $SFR - M_*$ relations for star-forming galaxies from Tomczak et al. (2016) at similar redshifts. While there is some overlap between the TGs and PSBs, the mean sSFR for PSBs is lower. The average sSFR increases at higher redshifts.

as a function of redshift - in general, higher redshifts saw fewer quenched galaxies, higher mass galaxies quenching, and higher star formation rates for star-forming galaxies of a given mass (e.g. Whitaker et al., 2012b; Behroozi et al., 2013; Sparre et al., 2015; Tomczak et al., 2016; Pandya et al., 2017).

Due to the large width of the redshift bins for our composite SEDs, the evolution of these relations is a driver of the scatter observed in Figure 3.8. Therefore while we find larger numbers of galaxies with high sSFRs and fewer quenched galaxies at higher redshifts, we do not make any conclusions about the efficacy of galaxy categorization by sSFR.

3.7.3 Morphological Evolution

We also investigate the morphologies of galaxies with regard to mass and classification, shown in Figure 3.9. The star-forming galaxies match well with previous analyses of the size-mass relation (e.g., ZFOURGE and COSMOS/UltraVISTA; Allen et al., 2017; Faisst et al., 2017). At low redshifts, all other galaxy classifications have smaller sizes for a given mass. The TGs in particular, have median sizes half those of the SFGs and twice those of the QGs, as would be expected for galaxies whose star formation is being quenched.

The median sizes for PSBs are $50 - 80\%$ the size of those for the QGs of the same mass, although the distributions overlap. Slightly smaller sizes for PSBs are suggestive of further size growth in quiescent galaxies despite the cessation of new star formation, in agreement with Yano et al. (2016); Almaini et al. (2017). Schawinski et al. (2014); Pandya et al. (2017) also point out that post-starburst galaxies often appear smaller than the typical galaxy at a given redshift due to the fact that these galaxies stopped forming stars at an earlier epoch, when the average galaxy size was smaller.

While ELGs and SFGs have similar Sérsic indices of $n \sim 1$, the TGs have values of $n \sim 2-3$, suggesting a morphological evolution coeval with a decrease in star formation. PSBs and QGs have values of $n \sim 3.5$, and the distributions look quite similar, in agreement with results from Almaini et al. (2017). This indicates that by the time star formation has ceased completely, any morphological changes such as the development of a central bulge are already complete, although further size growth may occur.

Additionally, we fit a line to the individual analog Sérsic indices against mass and redshift. No class shows evidence for significant evolution with redshift, with slopes $|m|< 0.2$, smaller than the spread and errors on the values. All classes except the ELGs show median increases with mass, although such increases are $\Delta n < 1$, no larger than the distribution of galaxy values for a given mass.

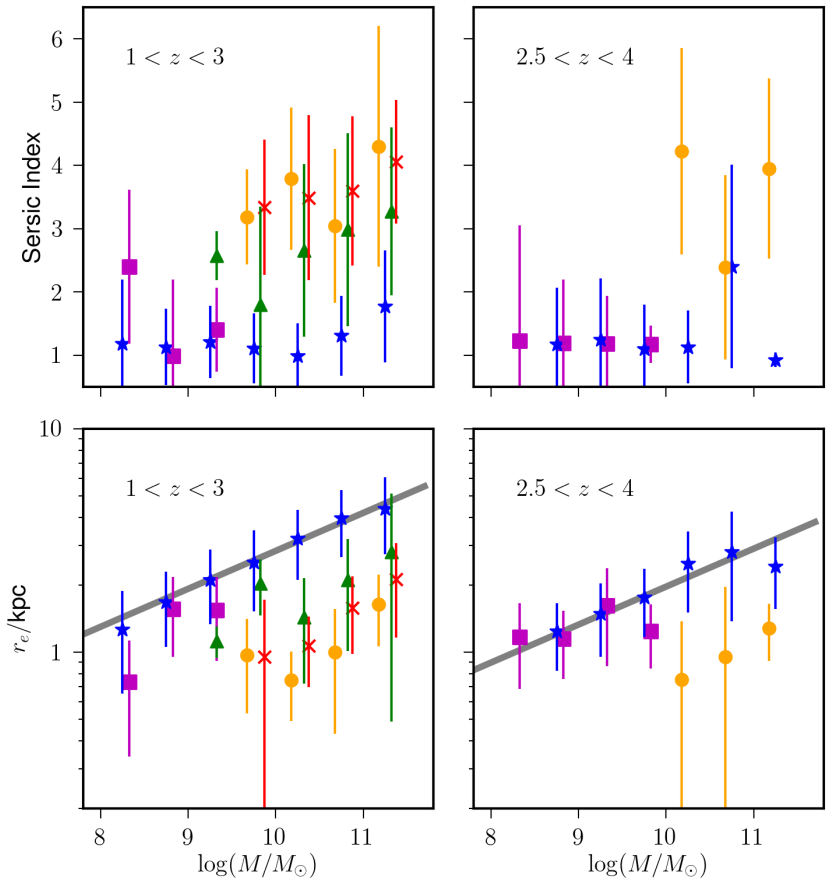

Figure 3.9: Sizes and Sérsic indices against stellar mass. *Top:* The Sérsic indices for galaxies in our sample according to mass and classification, color coded as in previous figures. Points are slightly offset along the abscissa for clarity. *Bottom:* The size-mass plane for galaxies in our composite SEDs. The SF galaxies follow the size-mass relations from Allen et al. (2017) (thick gray line) quite well, while at low-redshift all other classes are smaller in size for a given mass (top). At high reshifts (bottom), the ELGs have similar sizes, while PSBs are smaller.

3.7.4 Post-Starburst and Transitional Galaxy Number Densities

Using the composite SEDs classified as post-starbursts, we calculate the number densities of these galaxies across several redshifts. Our results, shown in Figure 3.10, are consistent with those from the NEWFIRM Medium Band Survey (NMBS; Whitaker et al., 2012a) and the UKIDSS Deep Survey (UDS; Wild et al., 2016) at $z \sim 1 - 2$ and extend out to higher redshifts. We note that each of these works selects PSBs in a different manner - Whitaker et al. (2012a) use an age

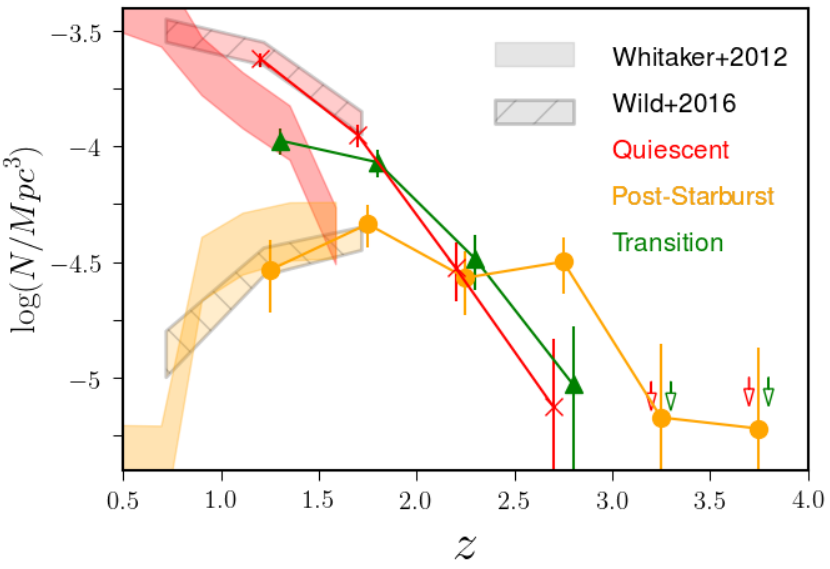

Figure 3.10: The evolution of comoving number density for quenching galaxies. The comoving number densities of QGs (red), PSBs (orange), and TGs (green) against redshift. Our results are consistent with the results from Wild et al. (2016) shown as hashed shaded regions. Results from NMBS (Whitaker et al., 2012a) are shown as non-hashed shaded regions. Notably, the shapes of the TG and QG curves appear quite similar, which is suggestive of them being along a similar evolutionary pathway. While both these tracks flatten out towards lower redshifts, the PSBs show strong evidence for a turnover around $z \sim 1.5$.

motivated cut on the *UVJ* diagram, Wild et al. (2016) use a selection based on Principal Component Analysis colors, while we use composite SEDs to select on population $D(4000)$ and emission line characteristics.

Comparing the number densities of different groups across a range of redshifts suggests that the transitional phase is even rarer than the traditional post-starburst phase at high redshifts, but becomes more common at $z < 2$. Additionally, the density of PSBs is relatively constant from $1.5 < z < 3$, with evidence for a turnover at $z \lesssim 1.75$, becoming rarer at lower redshifts. While the PSB curve stays mostly flat, the shape of the TG curve is more similar to that of the QGs, which increases dramatically from $z = 3$ before beginning to flatten at $z \sim 1.5$. This suggests that the TG population represents a quenching mechanism with a longer timescale than PSBs, which has become more prevalent at later times, discussed in more detail in the following section.

Across $3 < z < 4$, (Tomczak et al., 2016) report a ZFOURGE mass completeness limit of $\log_{10}(M/M_{\odot}) = 10.25$. The TGs, PSBs, and QGs have mass distributions with medians $\log_{10}(M/M_{\odot}) = 10.51$, 10.54, and 10.61, respectively. We thus expect that these populations are nearly complete out to $z \sim 4$, although a small number of lower mass galaxies may not have been detected. Due to the similar masses and detection-band magnitudes for members of the TGs, PSBs, and QGs, any biases and selection effects would effect them in a similar manner. While some individual galaxies in our $2.5 < z < 4$ PSB composite SEDs could be quiescent or transitioning, the clear differences in SED shape guarantee that they would be few in number.

3.8 Discussion

Our TG classification appears successful in picking out galaxies transitioning between more typical star-forming galaxies and quiescent galaxies. These galaxies have masses $\log_{10}(M/M_{\odot}) \sim 10.5$, consistent with dusty SFGs, PSBs, and QGs. However, there is no evidence of large amounts of dust in the TGs (compared to dusty SFGs of similar mass), with $A_V \sim 1$ mag (vs. $\sim 2-3$), and they show less Hα emission - $EW_{\rm REST} \sim 30-50$Å (vs. $30-100$Å for dusty SFGs; Figure 3.5). The red colors and low emission line equivalent widths are therefore due to fewer O and B type stars and low level residual star formation than to heavy dust obscuration, as expected for SFGs of similar mass.

The TGs still show more dust than PSBs and QGs (~ 0.5 mag) and are morphologically different (r_e/kpc~ 3 vs. 1 for PSBs and $n = 2.7$ vs. 3.5; Figure 3.9). Komolgorov-Smirnov tests for the distributions of TGs and PSBs in dust, size, and Sérsic index yield $p < 0.05$ and Anderson-Darling tests simillarly reject the hypothesis that the two groups are drawn from the same distribution.

Interestingly, the number density of the TGs in Figure 3.10 appears to 'lead' that of the QGs from $1 < z < 3$, suggesting an evolutionary pathway, while the PSBs have nearly constant number densities across the the same time, before becoming rarer at lower redshifts.

Galaxies in the green valley with similar low level sSFRs have had several potential explanations proposed. The most common is that these galaxies are in the process of quenching by some as yet undetermined mechanism(s), which are likely dependent on both galaxy mass and environment

(see Introduction of Darvish et al. (2016) for a nice summary). The variety of quenching mechanisms are associated with different timescales for the cessation of star formation. Barro et al. (2013) and Schawinski et al. (2014) showed that galaxies in the green valley of the color-mass diagram are representative of multiple quenching mechanisms and not a single separate population. On the other hand simulations have claimed that a single timescale of $\lesssim 2$ Gyr to cross the green valley is able to match observations (e.g., Trayford et al., 2016; Davé et al., 2017; Nelson et al., 2017; Pandya et al., 2017).

However, there is also the possibility that quiescent galaxies have had their star formation 'rejuvenated' and are thus moving into the green valley from the red side as suggested in both observations (e.g., Rampazzo et al., 2007; Fang et al., 2012; Darvish et al., 2016; Pandya et al., 2017) and simulations (e.g., Davé et al., 2017; Nelson et al., 2017). Such a movement is not only rare, but also results in only a small change in color, which cannot move a previously quenched galaxy to match the colors of galaxies in the blue cloud (Davé et al., 2017; Nelson et al., 2017). These rejuvenated galaxies are therefore not presumed to be a significant part of our TGs.

Another possibility is that SFGs oscillate about the star-forming main sequence, with periods of enhanced and reduced star formation on the order of 0.3 dex (e.g., Tacchella et al., 2016). Not only do stimulations suggest this is more common for lower mass galaxies (Zolotov et al., 2015b), but our TGs also extend over 1 dex below the main sequence, implying that this explanation can only contribute a small portion of the TGs observed.

A further hypothesis is that all galaxies in the process of quenching will have a post-starburst phase, which is shorter than the overall time in the green valley and either precedes or follows it. The relative number densities of TGs and PSBs conflict with this idea, as the number densities of PSBs are more constant over cosmic time, with a turnover around $z \sim 1.5$, while TGs continue to climb, more in concert with the QGs. Pandya et al. (2017) showed that post-starburst (fast-quenching) galaxies are more common at high redshifts relative to the transitional (slow-quenching) galaxies which dominate the quenching process below $z \sim 0.7$. Our results are consistent with this picture, where we find spatial number densities of transitional galaxies increasing

sharply with decreasing redshift, while post-starbursts appear to have a turnover at $z \sim 1.75$. We thus conclude that the vast majority of the TGs in our sample are in fact moving from the blue, disk dominated, star-forming cloud to the red, bulge dominated, quenched sequence, possibly through multiple mechanisms with similar timescales on the order of $1 - 2$ Gyr.

4. DISCOVERY OF EXTREME [OIII]+Hβ EMITTING GALAXIES TRACING AN OVERDENSITY AT $z \sim 3.5$ IN CDF-SOUTH *

4.1 Synopsis

Using deep multi-wavelength photometry of galaxies from ZFOURGE, we group galaxies at $2.5 < z < 4.0$ by the shape of their spectral energy distributions (SEDs). We identify a population of galaxies with excess emission in the K_s-band, which corresponds to [O III]+Hβ emission at $2.95 < z < 3.65$. This population includes 78% of the bluest galaxies with UV slopes steeper than $\beta = -2$. We de-redshift and scale this photometry to build two composite SEDs, enabling us to measure equivalent widths of these Extreme [O III]+Hβ Emission Line Galaxies (EELGs) at $z \sim 3.5$. We identify 60 galaxies that comprise a composite SED with [O III]+Hβ rest-frame equivalent width of 803 ± 228Å and another 218 galaxies in a composite SED with equivalent width of 230 ± 90Å. These EELGs are analogous to the 'green peas' found in the SDSS, and are thought to be undergoing their first burst of star formation due to their blue colors ($\beta < -1.6$), young ages ($\log(\mathrm{age/yr}) \sim 7.2$), and low dust attenuation values. Their strong nebular emission lines and compact sizes (typically ~ 1.4 kpc) are consistent with the properties of the star-forming galaxies possibly responsible for reionizing the universe at $z > 6$. Many of the EELGs also exhibit Lyman-α emission. Additionally, we find that many of these sources are clustered in an overdensity in the Chandra Deep Field South, with five spectroscopically confirmed members at $z = 3.474 \pm 0.004$. The spatial distribution and photometric redshifts of the ZFOURGE population further confirm the overdensity highlighted by the EELGs.

4.2 Background Information

The discovery of galaxies with strong [O III]λ5007 emission, extreme star formation rates (SFRs), low masses, and low reddening by Cardamone et al. (2009) was key to finding objects

*Reprinted with permission from "Discovery of Extreme [OIII]+Hβ Emitting Galaxies Tracing an Overdensity at $z \sim 3.5$ in CDF-South" by Forrest et al., 2017. The Astrophysical Journal Letters, Volume 838, Issue 1, article id. L12, 6 pp., Copyright 2017 by the American Astronomical Society.

thought to be responsible for the reionization of the Universe (Robertson et al. (2013); Nakajima & Ouchi (2014); Robertson et al. (2015)). Known as 'green peas' for their strong emission in the rest-frame optical and compact sizes, similar galaxies have since been found at much higher redshifts. These green peas seem in many aspects to be more extreme versions of blue compact dwarfs (Sargent & Searle (1970)), having low masses and strong nebular emission lines, albeit with distinctly higher specific star formation rates (sSFRs; e.g., Maseda et al., 2014).

These objects exhibit bright optical nebular emission lines such as Hα and [O III], with rest-frame equivalent widths of several hundred to over one thousand angstroms, indicating bursty star forming activity (e.g., Atek et al., 2011; van der Wel et al., 2011; Maseda et al., 2013; Stark et al., 2014; Sanders et al., 2016, hereafter S16). Such galaxies are increasingly common at higher redshifts, appear to have enhanced [O III]λ5007 relative to both Hβ and [OII]λ3727, and are often Lyman-α Emitters (LAEs) (e.g., Labbé et al., 2013; Smit et al., 2014; Holden et al., 2016; Trainor et al., 2016; Nakajima et al., 2016).

While the strong emission lines of these objects can be detected with spectroscopy at $z \sim 3$ (Holden et al., 2016; Nakajima et al., 2016, S16), the rest-frame optical stellar continuum is quite faint ($K_s > 25$). Indeed for such low-mass objects, this continuum has until recently been too faint for spectroscopy of large samples at these redshifts (e.g., Nanayakkara et al., 2016). However, we can use the deep multi-wavelength photometry available in ZFOURGE to construct composite SEDs (Forrest et al. (2016)) and analyze the faint stellar continuum of a sample of emission-line objects at $2.5 < z < 4.0$.

We will refer to the most intense of these compact, [O III]-emitting galaxies, as Extreme Emission Line Galaxies (EELGs), and galaxies with less intense, but still significant [O III] emission as Strong Emission Line Galaxies (SELGs) for the duration of the Letter. We assume a ΛCDM cosmology of $\Omega_M = 0.3$, $\Omega_\Lambda = 0.7$, and $H_0 = 70$ km s^{-1} Mpc^{-1}. For such a Universe, 1" = 7.320 kpc at $z = 3.5$. We use a Chabrier Initial Mass Function (Chabrier (2003)) and the AB magnitude system (Oke & Gunn (1983)).

4.3 Data & Methods

4.3.1 [OIII] Emitter Photometry

We use data from the medium band near-infrared FourStar Galaxy Evolution Survey (ZFOURGE; Straatman et al., 2016). This survey combines imaging from a large number of previous surveys to create the deepest K_s-band detection image (see Straatman et al., 2016, for details) of the Chandra Deep Field South (CDFS Giacconi et al., 2002)), with a 5σ limiting depth of 26.5 AB mag. Imaging in the COSMOS (Scoville et al. (2007)) and UDS (Lawrence et al. (2007)) fields are also quite deep, at 25.5 and 25.7 magnitudes, respectively. In addition, due to its medium band filters bracketing well-known features, such as the Balmer break, [O III] emission, and Hα emission, ZFOURGE provides precise photometric redshifts. Extensive testing against spectroscopic redshifts yielded $\sigma_{z,\mathrm{spec}} = 0.01$ (Nanayakkara et al., 2016; Straatman et al., 2016). The photometric redshift errors for objects without spectroscopic redshifts were also estimated from the photometric redshift differences of close pairs (Quadri & Williams (2010)). For blue star-forming galaxies, this method yields $\sigma_{z,\mathrm{pairs}} = 0.015$ at $z \sim 2.5$, which agrees with the z_{phot} determinations from EAZY (Brammer et al. (2008)).

In Section 3 I presented a set of composite SEDs from non-AGN ZFOURGE galaxies in $2.5 < z < 4.0$, with $SNR_{K_s} > 20$. Details of this method are given in Section 2. Here we analyze the bluest groups of galaxies from this group. Matching was performed slightly differently, with the smallest number of galaxies in a group before reassignment set to 20. While this yields different numbers of galaxies in a given composite SED, the qualitative results do not change.

The bluest composite SEDs show significant emission from [O III]+Hβ, corresponding to a sample of EELGs (60 galaxies), and the other to a population of SELGs (218 galaxies). The emission lines fall into the K_s-band in the redshift range $2.95 < z < 3.65$, and this excess flux in the K_s-band increases our confidence in the photometric redshifts, which are in strong agreement with the handful of spectroscopic redshifts available for this population.

Spectroscopic redshifts for a subset of galaxies in our sample are found by cross-matching

with several works including ESO/GOODS spectroscopy from *FORS2* (Vanzella et al. (2009)) and *VIMOS* (Balestra et al. (2010)), *3D-HST* (Momcheva et al. (2016)), and the ZFIRE survey (Nanayakkara et al. (2016)). These samples total 37 SELGs and 7 EELGs with either grism or spectroscopic redshifts. There are 17 emission line galaxies with *HST/WFC3/G141* grism redshifts from *3D-HST*, with median $|\Delta z|/z = 0.04$, and 27 with rest-frame ultraviolet spectroscopic redshifts, with median $|\Delta z|/z = 0.016$.

4.3.2 Fitting Stellar Continuum with FAST

We make use of FAST to fit the stellar continuum of the composite SEDs using the Bruzual & Charlot (2003) (BC03) models to obtain equivalent widths for optical emission lines in Section 4.4.2. Accounting for emission lines as strong as those observed in the EELGs is of critical importance during this process. Failure to do so will result in FAST overestimating the stellar continuum, leading to errors in parameters such as stellar mass, SFR, and age (e.g., Erb et al., 2010; Atek et al., 2011; Reddy et al., 2012b; Salmon et al., 2015, hereafter S15; Spitler, et al., in prep).

We test three methods for fitting both the composite SEDs and the individual galaxies using the BC03 models. Declining-τ models for all three methods have $7 < \log(\tau/\mathrm{yr}) < 11$, ages $6 < \log(\mathrm{age/yr}) < 9.25$, and dust attenuations $0 < \mathrm{A_V/mag} < 4$.

First, we fit the BC03 models to the set of photometry (Method A). The strength of the emission feature artificially raises the level of the stellar continuum, and thus the mass, for this method. Secondly, we use the same models, but mask out points affected by [O III]+Hβ emission (Method B). The third method uses a set of high resolution ($\Delta\lambda = 1$Å) BC03 models with emission lines added fit to the entire composite SED (Method C). These emission line models, as detailed in Section 3 of S15, include 119 sets of relative emission-line strengths with nebular emission taken into account. While the nebular continuum is not considered in this method, effects from this flux are minimal in the rest-frame optical, and so can be safely ignored (S15). We also run sets of models with several metallicity values.

Method C yields the best fit to the composite SED, with $\chi^2 = 4.97$ for the EELG composite, compared to $\chi^2 = 7.83$ using Method A, which is used in the ZFOURGE catalogs. The best fits also

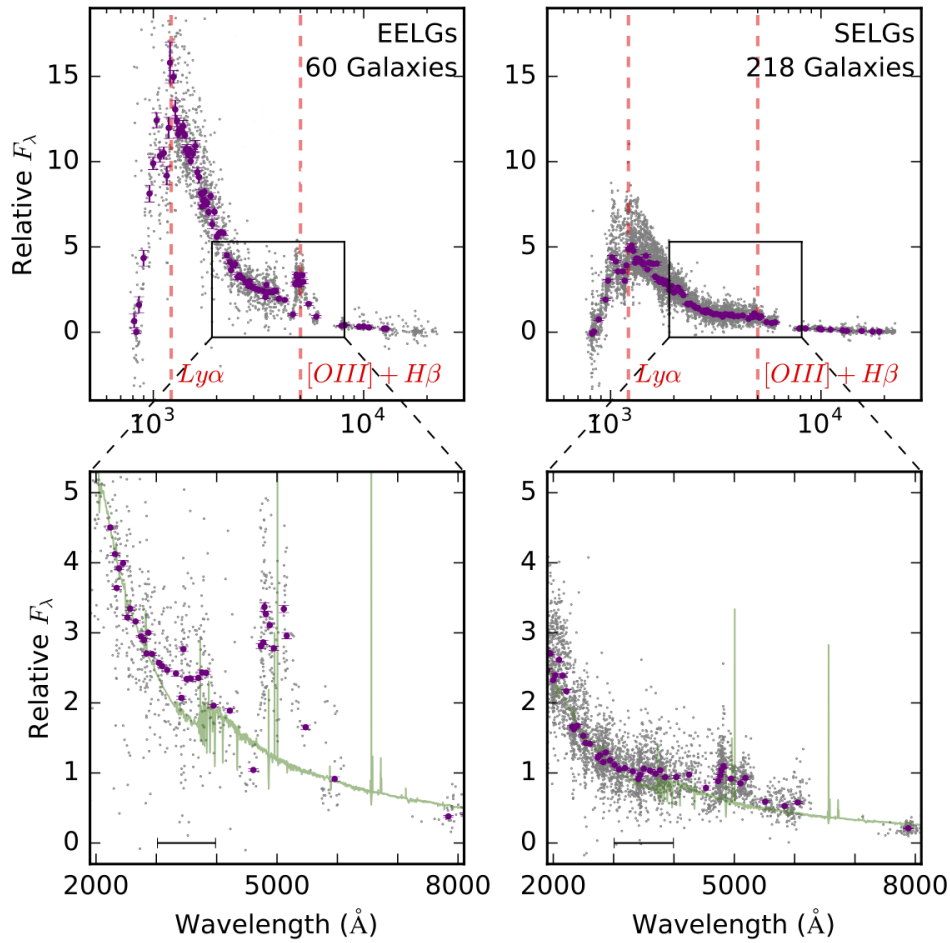

Figure 4.1: EELG and SELG composite SEDs. These galaxies have significant emission from [O III]λ5007 + Hβ, in the K_s-band at $z \sim 3.5$. Their de-redshifted and scaled analog photometry is shown in gray, while the median points which make up the composite SEDs are in purple. The best-fit model from FAST is green (emission lines are scaled down for clarity; see Section 4.3.2), and the characteristic width of the composite filters is shown at the bottom. The strong emission in [O III]+Hβ is apparent and the EELG composite (left) also shows Lyα emission.

have a sub-solar metallicity, $Z = 0.004$, in agreement with studies suggesting low metallicities for these galaxies (e.g., Salzer et al., 2005; Izotov et al., 2011; van der Wel et al., 2011, S15; S16). The resulting mean values and one sigma spreads for the individual ELGs are shown in Table 4.1.

4.4 [OIII]+Hβ Emission Line Galaxies

4.4.1 Galaxy Properties

Using Method C described above, we find that the EELG population in general is younger than the SELG population by 0.3 dex, has 0.5 dex less mass, and has more intense star formation (sSFR of $5.5 \times 10^{-8}\mathrm{yr}^{-1}$ compared to $1.5 \times 10^{-8}\mathrm{yr}^{-1}$). This is consistent with a picture of the SELG population being on the same evolutionary path, but slightly more evolved.

We find mean physical sizes of 1.34 kpc and 1.63 kpc for the EELG and SELG populations by cross-matching with the H_{F160W} sizes from CANDELS (van der Wel et al., 2012, $\lambda_{\mathrm{REST}} \sim 3400$Å at $z \sim 3.5$). However, we note that at $z \sim 3.5$ the angular resolution of $HST/WFC3/H_{F160W} \sim 0.95$ kpc, and so a number of these galaxies are unresolved. Nonetheless, the small sizes are consistent with measurements in both the local and distant Universe. Henry et al. (2015) find a NUV Petrosian radius of ~ 1 kpc at $z \sim 0.2$ ($\lambda_{\mathrm{REST}} \sim 1900$Å). The $1.4 < z < 2.3$ sample from Maseda et al. (2014) has sizes ranging from $0.5 < r_{eff}/\mathrm{kpc} < 1.6$, also based on data from van der Wel et al. (2012) ($4620 < \lambda_{\mathrm{REST}}/\text{Å} < 6350$). These data suggest that EELG populations across cosmic time have the same physical sizes at rest-frame UV wavelengths. Additionally, these sizes are consistent with the size-mass relation for $z \sim 3.5$ derived in Allen et al. (2017), which when extrapolated to $\log(M/M_{\odot}) \sim 9$ predicts a size of 1.2 kpc.

One of the objects in our EELG sample is the subject of S16, which analyzes a rest-frame optical spectrum from MOSFIRE. S16 finds galaxy properties in agreement with those derived in this work, namely a low mass ($\log(M_{\star}/M_{\odot}) = 9.33$), high sSFR ($2.3 \times 10^{-8}\mathrm{yr}^{-1}$), young age (160 Myr), and low dust attenuation ($E(B-V)_{\mathrm{stars}} = 0.12$). Critically, they also find a metallicity of 12+(O/H) = 8.00, which confirms the low metallicities characteristic of galaxies undergoing early star formation (Izotov et al. (2011)).

Table 4.1: Properties of the ELG Population

	EELGs			SELGs		
	Method A[1]	Method B	Method C[2]	Method A	Method B	Method C
$\log(M_*/M_\odot)$	$9.2^{+0.3}_{-0.4}$	$8.9^{+0.4}_{-0.3}$	$8.7^{+0.2}_{-0.3}$	$9.4^{+0.3}_{-0.3}$	$9.1^{+0.3}_{-0.3}$	$9.1^{+0.3}_{-0.3}$
$\log(\text{age/yr})$	$8.0^{+0.6}_{-1.2}$	$7.6^{+0.6}_{-0.6}$	$7.2^{+0.1}_{-0.3}$	$8.2^{+0.2}_{-0.2}$	$7.6^{+0.7}_{-0.6}$	$7.5^{+0.4}_{-0.3}$
$\log(\tau/\text{yr})$	$8.1^{+0.6}_{-1.1}$	$8.6^{+2.0}_{-1.6}$	$7.7^{+1.0}_{-0.7}$	$8.0^{+0.4}_{-0.6}$	$8.2^{+1.0}_{-1.1}$	$7.3^{+0.3}_{-0.3}$
SFR $(M_\odot/\text{yr})$	21^{+25}_{-19}	45^{+13}_{-40}	24^{+15}_{-15}	23^{+17}_{-21}	50^{+32}_{-41}	18^{+12}_{-12}
A_V (mag)	$0.21^{+0.44}_{-0.21}$	$0.42^{+0.32}_{-0.31}$	$0.45^{+0.20}_{-0.25}$	$0.15^{+0.00}_{-0.15}$	$0.53^{+0.27}_{-0.23}$	$0.46^{+0.19}_{-0.21}$
$EW_{[OIII]+H\beta}$[3] (Å)	309 ± 115	659 ± 189	803 ± 228	100 ± 67	250 ± 103	230 ± 90
r_e[4] (kpc)			$1.34^{+0.52}_{-0.74}$			$1.62^{+0.65}_{-0.84}$

4.4.2 Large [OIII]+Hβ Equivalent Widths

While the BC03+emission line models produce good fits to the composite SEDs (see Figure 4.1), they still underpredict the strength of the [O III]+Hβ emission feature. To estimate the equivalent width, we remove the emission features from the model and add back in emission lines to match the observed composite SED feature.

We take the continuum to be the level of the best-fit spectrum from FAST using Method C where there are no emission lines, and use a simple linear interpolation to derive the continuum in areas with such features. Since these models have resolution of 1Å in the optical, all absorption features (i.e., Hβ absorption) are retained. After obtaining the continuum fit to the composite SED, we add to it an emission line model with the following flux ratios: $F_{[OIII]\lambda5007} = 3F_{[OIII]\lambda4959} = 7F_{H\beta}$ (e.g., Salzer et al., 2005; van der Wel et al., 2011; Holden et al., 2016; Trainor et al., 2016, S16). The resultant spectrum is convolved with the custom composite SED filters to create synthetic photometry. The amplitude of the emission line model is varied to minimize the least squares of the composite SED and the synthetic photometry. We do not have the resolution to separate the effects of the lines but ratios of [O III]λ5007 to Hβ from 1 to 20 were tested with negligible change to the resulting equivalent width. Errors on the equivalent width were calculated by fitting a range of line strengths to form a grid of χ^2 values and one sigma errors were calculated using the relation $P \propto e^{-\chi^2/2}$.

For the EELG composite SED, we obtain a rest-frame equivalent width $EW_{[OIII]+H\beta} = 803 \pm 228$Å, corresponding to an observed-frame equivalent width $EW_{[OIII]+H\beta} = 3565$Å at the median redshift $z = 3.44$ (see Figure 4.2). The rest-frame equivalent width for the EELG population is consistent with those of EELGs in many studies which range from $\sim 200 - 1600$Å (Atek et al., 2011; van der Wel et al., 2011; Maseda et al., 2013, S16). The SELG population has a rest-frame equivalent width $EW_{[OIII]+H\beta} = 230 \pm 90$Å. Spectroscopic follow-up of these objects would be useful for not only confirming the accuracy of this method, but also analyzing the spread of equivalent width values and [O III]/Hβ line ratios within the population.

To quantify uncertainties in the equivalent widths that are due to uncertainties in the photometric redshifts, we redshift a high equivalent width template and calculate synthetic K_s-band photometric values. We then mimic our composite SED method by de-redshifting the template using the 'correct' redshift with noise added according to the $|\Delta z|/z$ values from spectroscopy (see Section 4.3.1). Repeating this process 100 times, we measure the equivalent width to be 868 ± 273Å, which matches very well with our measurement of 803 ± 228 Å(Table 1, Method C).

We also note that both composite SEDs show emission in the ultraviolet (UV), consistent with many of the analogs having Lyα emission. Several studies have suggested that LAEs are similar to the EELGs (e.g., Hagen et al., 2016; Trainor et al., 2016; Nakajima et al., 2016); our sample is consistent with that picture.

4.4.3 Incidence of ELGs at High Redshift

EELGs are less common locally than at higher redshifts (e.g., Atek et al., 2011; van der Wel et al., 2011; Maseda et al., 2014, 2016; Smit et al., 2014). In the redshift range of $2.5 < z < 4.0$ we detect 60 EELGs with $SNR_{K_s} > 20$, with the faintest at $K_s = 24.9$ magnitudes, and a characteristic equivalent width of $EW_{\rm REST} = 803$Å. Separating the EELGs by field we find 6.29×10^{-5} Mpc^{-3}, 0.897×10^{-5} Mpc^{-3}, and 2.15×10^{-5} Mpc^{-3} for CDFS, COSMOS, and UDS respectively. SELGs have densities of 23.0×10^{-5} Mpc^{-3}, 4.34×10^{-5} Mpc^{-3}, and 7.02×10^{-5} Mpc^{-3} in the same order, and are 3.7 times more common than the EELGs in total.

In the redshift range $2.5 < z < 4.0$, these EELGs and SELGs dominate the population of the

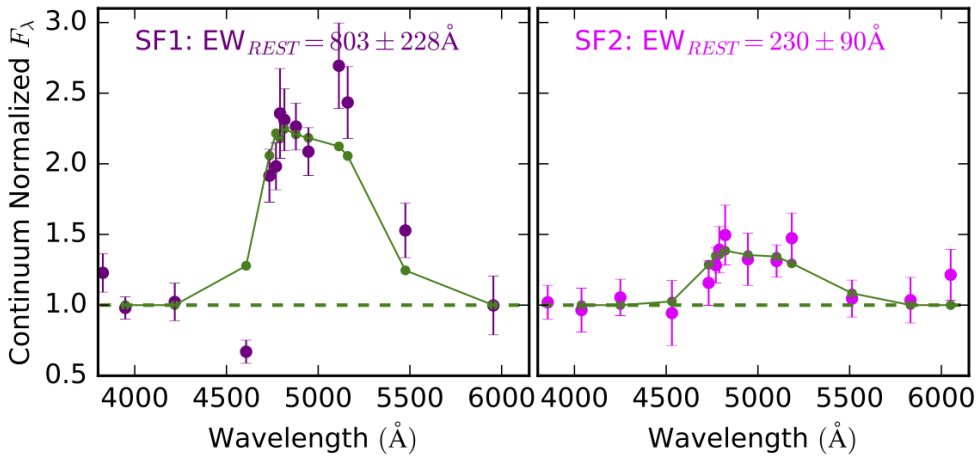

Figure 4.2: The equivalent width for our EELG and SELG composite SEDs. The purple points show the composite SED normalized to the level of the stellar continuum as fit by FAST in the range while masking the emission feature. Green points represent the synthetic photometry of the stellar continuum + emission line model in the effective composite SED filter curves.

bluest galaxies with $\beta < -2$. We select all ZFOURGE galaxies with $(U\text{-}V)_{\rm REST} < 1$, $(V\text{-}J)_{REST} < 1$ and at least 5 photometric detections in the restframe wavelength range $1250 < \lambda/ < 2600$, and fit a power law, $F_\lambda \propto \lambda^\beta$ to obtain the UV slope, β (Calzetti et al. (1994)). Of the 58 such galaxies with $\beta < -2$, 45 (78%) fall into our EELG or SELG groups, indicating that the majority of the bluest galaxies have strong emission features.

4.5 Large Scale Structure in CDFS at $z \sim 3.5$

The EELGs and SELGs show an unexpected peak at $z \sim 3.5$ in CDFS. The full redshift distribution of galaxies in the ZFOURGE catalog, both photometric and spectroscopic, also confirms the presence of a galaxy overdensity at $z \sim 3.5$ in CDFS (Straatman et al., 2016, see Figure 4.3, as well as Figure 23 of). Comparing the CDFS redshift distribution to the combined distribution from COSMOS and UDS shows a strong difference, greater than 10σ as found using a K-S test. Such an overdensity has been suggested by data from *3D-HST* (Skelton et al., 2014, Figure 24), who use EAZY as well. The same is not found in CDF-North, which has similar filter coverage

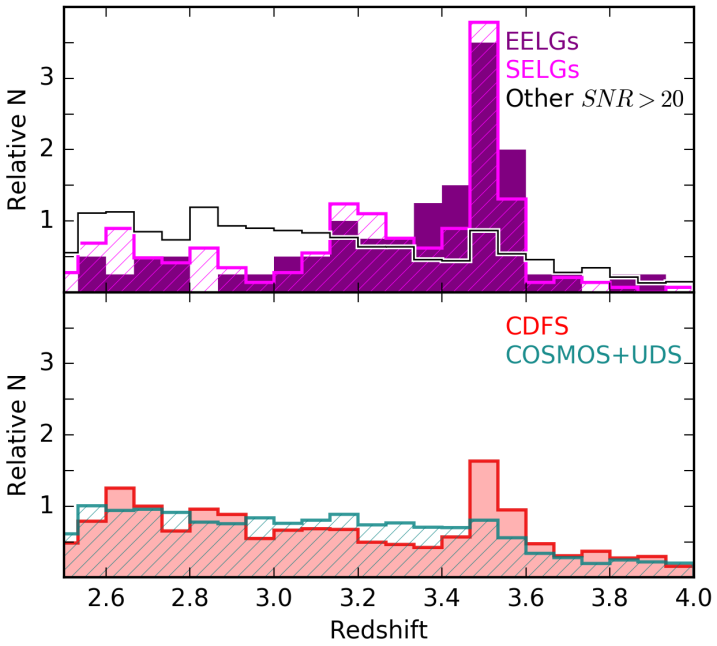

Figure 4.3: Redshift distributions for galaxies in our sample. The top panel shows the photometric redshifts for the EELG and SELG populations in purple and light purple, respectively, as well as galaxies from the other composite SEDs of Forrest, et al., in prep, in black. On the bottom is the normalized distribution of photometric redshifts for all galaxies with $K_s < 24.9$ in $2.5 < z < 4$.

and K_s-band depth, and selects based on $HST\ F125W + F140W + F160W$ imaging (their tables 6 and 7). This removes the possibility of the overdensity being due to a bias in EAZY.

To map possible overdensities projected on the sky, we use the 7^{th} nearest-neighbor measure (e.g., Papovich et al., 2010; Spitler et al., 2012). For each field, we create a grid of 1000 points on a side, and calculate the distance to the 7^{th} closest galaxy at each point, which is converted into a density. Each point in all three fields is shaded by the number of standard deviations above the mean density in the respective field (see Figure 4.4). Additional density calculations were made using the $3^{rd}, 5^{th}$, and 10^{th} nearest neighbors - the results are similar to those from the 7^{th} nearest neighbor measure.

In the top row of Figure 4.4, we show all three fields considering galaxies in the range $3.42 < z < 3.56$, with a magnitude cut of $K_s < 24.9$ mag, where all three fields are complete (Straatman et al., 2016). The 5 sigma peak in the UDS contains 10 galaxies while the 5 sigma peaks in

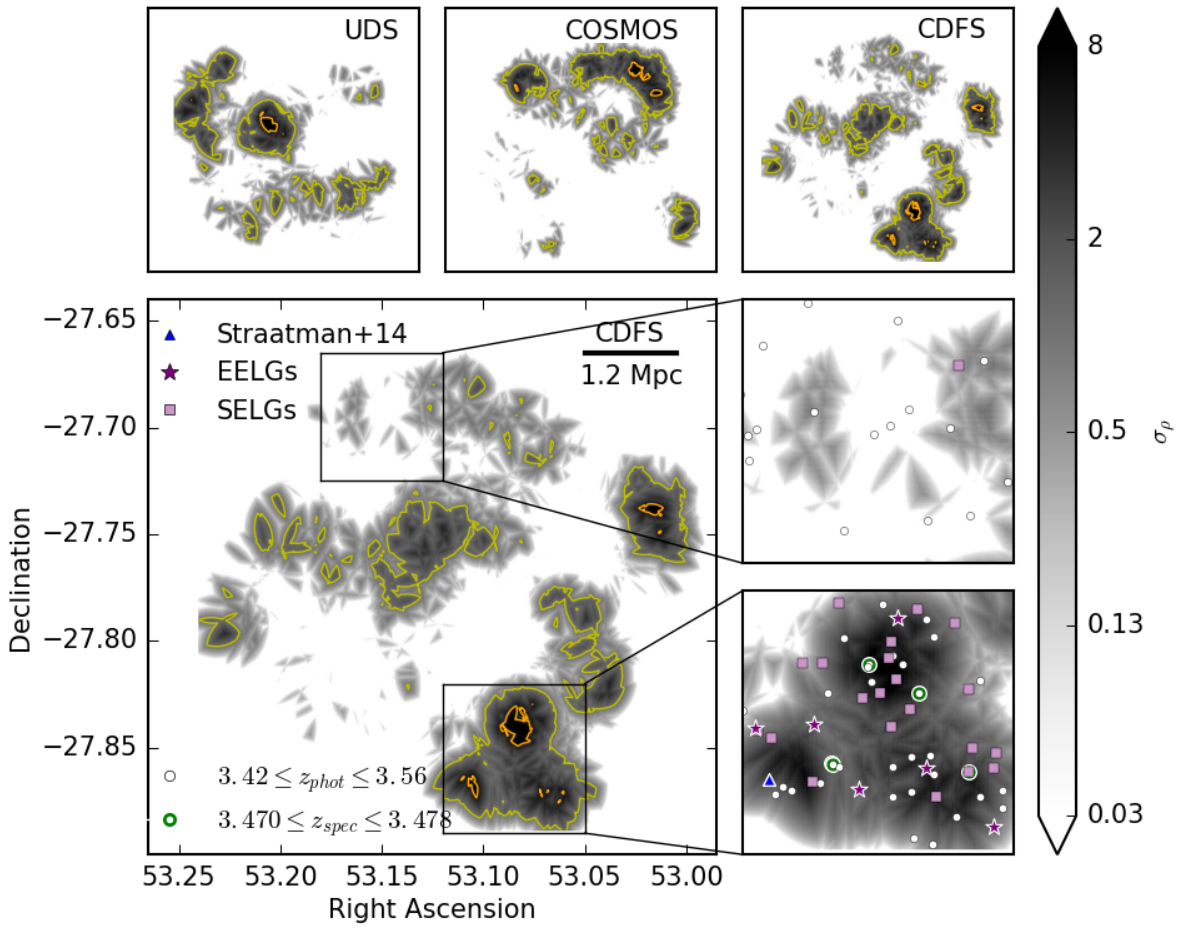

Figure 4.4: Overdensity in CDF-S at $z \sim 3.47$. *Top:* Projected spatial density in all three ZFOURGE fields of the galaxies in the redshift range $3.42 \leq z \leq 3.56$ and brighter than $K_s < 24.9$. The density at a point is determined using the 7^{th} nearest neighbor metric, and shaded by number of standard deviations above the mean density in the field. Both 1σ (yellow) and 5σ (orange) contours are shown. *Bottom:* Projected spatial density for CDFS with galaxies overplotted. Galaxies with $3.470 \leq z_{\rm spec} \leq 3.478$ are shown in green and a massive quiescent galaxy from Straatman et al. (2014) at $z = 3.56$ is displayed in blue. For individual galaxies in $3.42 \leq z \leq 3.56$, EELGs are purple stars, SELGs are magenta squares, other galaxies are white circles. Note that the overdense region has five spectroscopically confirmed galaxies - the leftmost two have a projected separation of ~ 1 arcsecond, and so are not resolved at this scale.

COSMOS contain $10 - 30$ galaxies. In contrast, the largest overdensity in CDFS contains 53 galaxies. Slightly increasing or decreasing the redshift ranges does not change our results. We focus on the most significant overdensity at $z \sim 3.5$ which is in CDFS but note that we do not exclude an overdensity in COSMOS.

At $z = 3.5$, the galaxy overdensity in CDFS at (RA, Dec) = (53.08, -27.85) is approximately 1.8 Mpc in size. Spectroscopy by Vanzella et al. (2009) in CDFS confirm five galaxies at $z = 3.474$ (Figure 4.4, green circles). Straatman et al. (2014) also report a massive quiescent galaxy at $z = 3.56$ (Figure 4.4, blue triangle).

Previous studies find that blue galaxies such as LAEs and LBGs trace large scale structure (e.g., Steidel et al., 1998; Ouchi et al., 2005). Our results confirm that galaxies with strong [O III]+ Hβ emission also exist in such overdensities. EELGs have the added advantage that they can be spectroscopically confirmed more easily via their strong emission.

A possible bias in our result is that the nebular emission at $z \sim 3.5$ is boosting the flux in the K_s-band such that we are preferentially detecting lower mass galaxies at this redshift. However, the redshift and projected distributions of galaxies without these strong emission features show evidence of an overdensity as well.

5. UV TO IR LUMINOSITIES AND DUST ATTENUATION DETERMINED FROM ∼4000 *K*-SELECTED GALAXIES AT $1 < z < 3$ IN THE ZFOURGE SURVEY *

5.1 Synopsis

We build a set of composite galaxy SEDs by de-redshifting and scaling multi-wavelength photometry from galaxies in the ZFOURGE survey, covering the CDFS, COSMOS, and UDS fields. From a sample of ∼4000 K_s-band selected galaxies, we define 38 composite galaxy SEDs that yield continuous low-resolution spectra ($R \sim 45$) over the rest-frame range 0.1-4 μm. Additionally, we include far infrared photometry from the *Spitzer Space Telescope* and the *Herschel Space Observatory* to characterize the infrared properties of our diverse set of composite SEDs. From these composite SEDs we analyze the rest-frame *UVJ* colors, as well as the ratio of IR to UV light (IRX) and the UV slope (β) in the IRX$-\beta$ dust relation at $1 < z < 3$. Blue star-forming composite SEDs show IRX and β values consistent with local relations; dusty star-forming galaxies have considerable scatter, as found for local IR bright sources, but on average appear bluer than expected for their IR fluxes. We measure a tight linear relation between rest-frame *UVJ* colors and dust attenuation for star-forming composites, providing a direct method for estimating dust content from either *(U-V)*or *(V-J)*rest-frame colors for star-forming galaxies at intermediate redshifts.

5.2 Background Information

Constraining the dust content of galaxies is vital to improving our knowledge of star formation histories and galaxy evolution. The geometry and orientation of dust grains, as well as their spatial distribution in galaxies greatly affect the shape of a galaxy's observed spectral energy distribution (SED) (e.g., Chevallard et al., 2013; Casey et al., 2014; Penner et al., 2015; Salmon et al., 2015). Correcting for these effects is necessary to understand the intrinsic properties of a galaxy. For nearby galaxies, spectroscopy provides insight into these effects. However, because spectroscopy

*Reprinted with permission from "UV to IR Luminosities and Dust Attenuation Determined from ∼4000 K-Selected Galaxies at $1 < z < 3$ in the ZFOURGE Survey" by Forrest et al., 2016. The Astrophysical Journal Letters, Volume 818, Issue 2, article id. L26, 6 pp., Copyright 2016 by the American Astronomical Society.

requires significantly more telescope time and brighter targets than photometry, photometry is a better choice for large, deep samples.

Beyond the local universe, galactic properties are often determined by fitting stellar population synthesis models to a handful of photometric points, then assigning redshifts, ages, metallicities, masses, etc. to the galaxy based on the best fitting SED (e.g., Papovich et al., 2001; Franx et al., 2003). The use of medium band near-IR filters in the NEWFIRM Medium Band Survey (NMBS; Whitaker et al., 2011) and the Fourstar Evolution Survey (ZFOURGE; Straatman et al., 2016) has enabled more accurate photometric redshift ($z_{\rm phot}$) measurements of large numbers of galaxies, on the order of $\sigma_{\rm NMAD} \sim 0.01 - 0.02$ (for $K_s < 25$) when compared to higher quality redshifts from grism Bezanson et al. (2016) and spectroscopic observations Nanayakkara et al. (2016). These surveys also cover legacy fields which have extensive photometric observations from the rest-frame UV to the near-IR.

The combination of greater photometric sampling and near-IR filters which identify the 4000Å break allow for a more constrained SED fit (e.g., Kriek & Conroy, 2013). This makes these surveys prime datasets for the development of multi-wavelength composite SEDs. If one can determine which galaxies have intrinsically similar SEDs, then by de-redshifting and scaling photometry for galaxies at several redshifts one can generate a well-sampled composite SED. Over the last few years, several papers have demonstrated the effectiveness of multi-wavelength composite SEDs in determining galaxy properties (e.g., Kriek et al., 2011; Kriek & Conroy, 2013; Utomo et al., 2014; Yano et al., 2016). In this work we use data from the ZFOURGE survey (http://zfourge.tamu.edu/) to define composite SEDs due not only to the survey's accurate redshifts, but also its depth (limiting magnitude of $K \sim 25.5$ mag). This allows us to build composite SEDs from galaxies at higher redshifts and lower masses than previous studies while still maintaining precision in our $z_{\rm phot}$ measurements.

The optical to near-infrared (IR) SED characterizes the properties of the stellar populations. To better track total star formation, rest-frame mid-far IR observations, which indicate the amount of dust heated by young, massive stars, are essential (e.g., Kennicutt, 1998; Kennicutt & Evans, 2012).

The ultraviolet (UV) flux more directly traces these stars, and the ratio of these two components, the infrared excess (IRX), is a tracer of dust attenuation in the UV. The UV slope (β) is also sensitive to the effects of dust Calzetti et al. (1994), and it can be compared to the IRX to determine how dust attenuation affects the light of star-forming galaxies.

This IRX$-\beta$ relation has been fit for various samples in the local universe (e.g., Meurer et al., 1999; Howell et al., 2010; Overzier et al., 2011) and in some cases compared to samples at higher redshifts Reddy et al. (2010, 2012a); Penner et al. (2012); Casey et al. (2014); Salmon et al. (2015). Notably, Howell et al. (2010) found that (U)LIRGs in the local universe do show significant scatter about IRX$-\beta$ relations, largely due to variations in IR flux. The resulting relations have also been used to derive properties such as continuum reddening Puglisi et al. (2016) and distributions of dust in dust-obscured galaxies (DOGs) Penner et al. (2012). Several of these works found discrepancies between high-z dusty star-forming galaxies and local IRX$-\beta$ relations. Many of these studies estimate IR fluxes from a single photometric point, usually a *Spitzer*/MIPS 24 μm flux. Our inclusion of *Herschel* data broadens the IR wavelength range and improves determination of the IR flux, although uncertainties still do exist.

We assume a ΛCDM cosmology of $\Omega_M = 0.3$, $\Omega_\Lambda = 0.7$, and $H_0 = 70$ km s^{-1} Mpc^{-1} and a Chabrier IMF Chabrier (2003), and adopt an AB magnitude system Oke & Gunn (1983).

5.3 Data & Methods

5.3.1 Data

We use photometric data from the deep near-IR ZFOURGE survey (Straatman et al., 2016), covering the CDFS Giacconi et al. (2002), COSMOS Scoville et al. (2007), and UDS Lawrence et al. (2007) fields, as well as archival data to obtain photometric coverage over observed wavelengths ranging from 0.3 μm to 8 μm. The near-IR filters of ZFOURGE split the traditional J and H bands into 3 and 2 medium-band filters, respectively. These allow us to constrain the photometric redshifts of the observed galaxies with a much higher precision than previously available - $\sigma_{\rm NMAD} = 0.02$ (Nanayakkara et al., 2016).

We also include data from *Spitzer*/MIPS 24 μm (GOODS-S: PI Dickinson, COSMOS: PI Scoville, UDS: PI Dunlop) and *Herschel*/PACS 100 μm and 160 μm filters from deep Herschel surveys of GOODS-S (Elbaz et al. 2011) and of the CANDELS COSMOS and UDS fields (PI: Dickinson; Inami et al. in preparation). Section 2.3 from Tomczak et al. (2016) provides a description of how IR fluxes were measured. Critically, these data allow better characterization of the rest-frame infrared wavelengths - and therefore dust content - of many of these galaxies.

To reduce any uncertainties due to photometric errors, we use a K_s-band signal to noise cut of 20. We also restrict our sample to the redshift range $1.0 < z < 3.0$.

5.3.2 Building Composite SEDs

We again use the composite SED method, which broadly follows the methods of Kriek et al. (2011) and Utomo et al. (2014) and is outlined in Section 2. It should be noted that this procedure used a previous, internally released version of the ZFOURGE catalogs, which had fewer galaxies than the one used in Sections 3 & 4.

After making the redshift and SNR cuts mentioned above, we are left with 3984 galaxies. We obtain 38 composite SEDs from 2598 galaxies that we use for the remainder of this analysis; these have a resolving power of $R \sim 45$ in the rest-frame optical. The remaining galaxies are in groups with fewer than 20 analogs. Example composite SEDs are shown in Figure 5.1.

Each composite point is dependent on the filter curves of the underlying photometry. To determine rest-frame colors and parameters from SED-fitting, custom filter curves are defined for each point in our composite SEDs. This is done by de-redshifting observed filter curves and scaling them to equal volume, then summing their responses. Note that the errorbars on the composite SED points are $\sigma_{\rm NMAD}$ errors on the medians and do not represent the errors in the photometry of the analogs. In addition, a number of galaxies have negative flux measurements in the IR because their photometry is dominated by noise in the background-subtracted images; these are plotted as downward arrows in Figure 5.1. Such non-detections are included when calculating medians and errors to build our composites and are not removed. These composite SEDs reveal details, such as Hα emission, that are usually only available through spectroscopy.

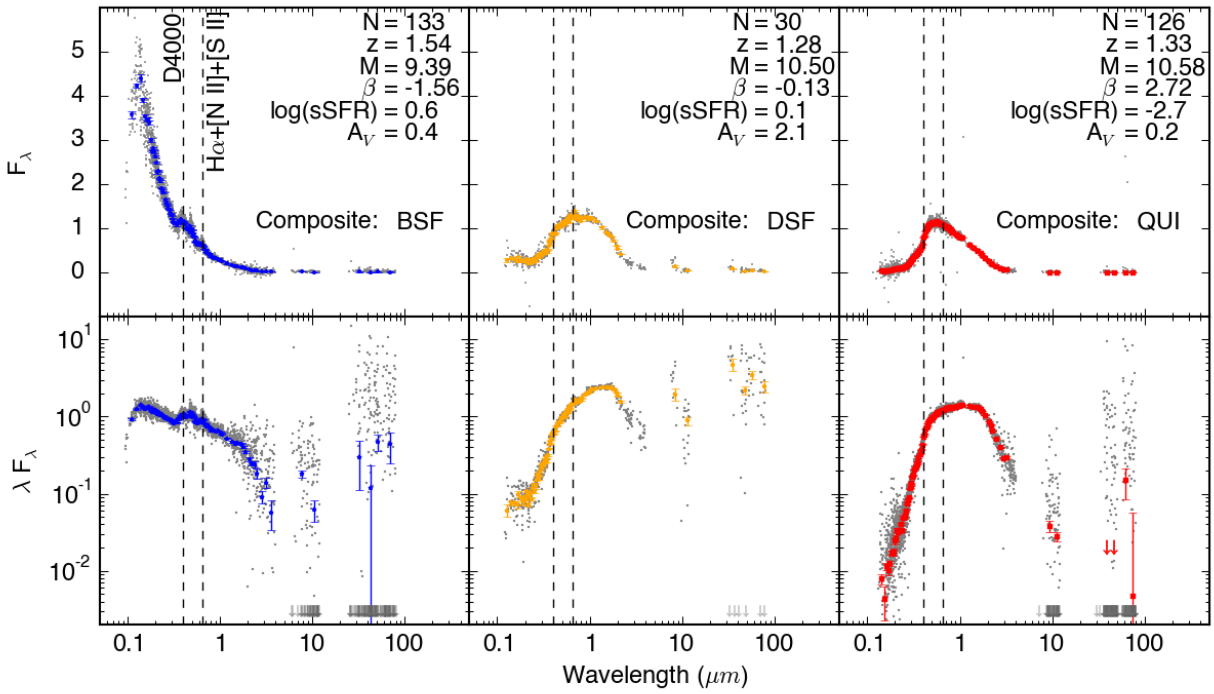

Figure 5.1: Examples of composite SEDs. These include a blue star-forming composite SED (BSF), a dusty star-forming composite SED (DSF), and a quiescent composite SED (QUI). Colored points represent the composite SEDs with NMAD scatter on the median as errorbars, while the gray points are the de-redshifted, scaled photometry from observations. Downward arrows show non-detections in the *Spitzer*/MIPS and *Herschel*/PACS filters and reflect the flux limits in those bands. The numbers given are the number of galaxies in the composite SED, the $z_{\rm phot}$ and mass of the median galaxies, as well as the UV slope, the logarithm of the specific star formation rate (sSFR), and the dust attenuation A_V, also determined from SED-fitting. Vertical dashed lines mark the location of the $D(4000)$ break and the Hα line blend. The increased IR flux in the dusty star-forming composite SED relative to the quiescent composite SED likely reflects reddening from dust. This is also supported by the A_V values reported by FAST.

For each of our composite SEDs, we also generate 100 bootstrapped composite SEDs. Each one is made by performing a bootstrap resampling of the analog galaxies for the composite SED and recalculating the SED points and custom filter curves. For parameters such as UV slope, UV flux, and IR flux, the same methods are applied to these bootstrapped composite SEDs to obtain errors on said parameters.

5.4 Analysis

5.4.1 UVJ Colors of Composite SEDs

In the star-forming section of the *UVJ* plane, a strong correlation exists between redder colors and increased dust attenuation Wuyts et al. (2007); Williams et al. (2009); Patel et al. (2012). Additionally, the quiescent population has a considerably lower specific star formation rate (Williams et al., 2009; Papovich et al., 2015; Straatman et al., 2016, sSFR;). It should be noted that the sSFR values reported by our SED-fitting program, FAST Kriek et al. (2009) do not consider the IR portion of the data. In Figure 5.2 we plot our composite SEDs on the *UVJ* diagram to analyze these relations. The composite SEDs span the range covered by observed galaxies quite well, although the most extreme colors are not represented due to their rarity in our initial sample. The previously known strong trend of star-forming galaxies with increasing dust (A_V) from the bottom-left to the top-right of the plot is quite clear, as is the strong decrease in sSFR from the star-forming to the quiescent regions. We analyze these results in conjunction with our IRX$-\beta$ results in Section 5.4.3.

5.4.2 IRX$-\beta$ Relation of Star-Forming Composite SEDs

To obtain β we fit the scaled rest-frame UV data from our composite SEDs with a power law of the form $F_\lambda \propto \lambda^\beta$. In this work we use photometry with rest-frame wavelengths in the range $1500 < \lambda/\text{Å} < 2600$ to fit the UV slope, similar to the range of the Calzetti et al. (1994) fitting windows, and mask points within 175 Å of the 2175 Å feature Noll et al. (2009a); Buat et al. (2011, 2012). We also obtain the UV flux for our IRX calculation by integrating under the power law fit determined above in a 350 Å window centered on 1600 Å as in Meurer et al. (1999).

We calculate the IR flux by fitting the average template from Chary & Elbaz (2001) to the scaled, de-redshifted composite SED IR points, and integrating under the resultant template from $8-1000$ μm (Forrest et al., in prep). Additionally we only use such points that are at longer wavelengths than 8 μm in the rest-frame. Individual galaxies in our composite subsamples have luminosities $9.7 < \log(L_{IR}/L_{\odot}) < 13.6$, while the average of galaxies in a single composite range $10.5 < \log(L_{IR}/L_{\odot}) < 11.5$. Galaxies in a particular composite have a median L_{IR} scatter of 0.4 dex. For star-forming composite SEDs, this model is sufficient for our analysis. It should be noted however that the Chary & Elbaz (2001) templates are not designed to fit quiescent galaxies. As such, quiescent composite SEDs (as determined by position on the *UVJ* diagram) are neither included on our IRX$-\beta$ plot, nor considered when calculating our IRX$-\beta$ relation.

Having obtained the three measurements necessary for the IRX$-\beta$ plot, we show our star-forming composite SEDs in Figure 5.3. We find the IRX$-\beta$ relation that fits these composite SEDs using the form

$$IRX = BC_{\rm UV} \times [10^{0.4A_{1600}} - 1]. \tag{5.1}$$

Here $BC_{\rm UV}$ corrects to obtain all luminosity redward of the Lyman break (912 Å). We assume $BC_{\rm UV} = 1.68$, as derived in similar studies Meurer et al. (1999); Overzier et al. (2011); Takeuchi et al. (2012); Casey et al. (2014) to compute the least squares best fit to the data.

The other parameter is the dust attenuation at 1600 Å, which is assumed to be a foreground screen, and thus linearly correlated with β as $A_{1600} = q + r\beta$ Meurer et al. (1999). Performing a fit to the star-forming composite SEDs we obtain:

$$IRX = 1.68 \times [10^{0.4(5.05+2.39\beta)} - 1]. \tag{5.2}$$

Our slope parameter of $r = 2.39$ is steeper than previously determined values of $r \sim 2$ (see Table 1). There is no discrepancy in our blue star-forming composite SEDs, as they are consistent with both local relations (e.g., Meurer et al., 1999; Overzier et al., 2011; Takeuchi et al., 2012)

and higher redshift samples (e.g., Reddy et al., 2010, 2012a). This can be seen in the left panel of Figure 5.4.

Several previous studies of IR-luminous galaxies at $z \sim 0$ have shown that IR-luminous galaxies have greater scatter in the IRX$-\beta$ plane and lie above relations derived for starburst galaxies (e.g., Howell et al., 2010; Overzier et al., 2011; Reddy et al., 2012a; Casey et al., 2014). Similarly, the composite SEDs most discrepant from the Meurer et al. (1999) relation are those with the highest average IR flux among their analogs, in agreement with Howell et al. (2010) ($z \sim 0$ and Penner et al. (2012) ($z \sim 2$). However, many of these studies used UV- or IR-selected samples, whereas our work uses the largest sample yet of mass-selected galaxies at $z \sim 2$.

More recently, Talia et al. (2015) analyzed the $A_{1600}-\beta$ relation using high-redshift UV spectra of 62 IR-detected galaxies at $1 < z < 3$, obtaining a much flatter fit than previous work, although still broadly consistent with predictions based on the Calzetti attenuation law. Our work, utilizing photometry only, includes a much larger sample, suggesting that previous works making use of local IRX$-\beta$ relations incorrectly estimate the extinction of the UV continuum for high redshift dust-obscured samples.

This offset implies that the dust attenuation at redshifts $z \sim 1-3$ is different from that in local galaxies; specifically, the steeper slope of our $A_{1600} - \beta$ relation means that dusty star-forming galaxies in our sample's redshift range have more UV attenuation due to dust than would be assumed from local calibrations. This amounts to a 0.5 magnitude underestimate of 1600 Å attenuation for galaxies with $\beta = 0$, increasing towards $\beta \sim 1$, and becoming consistent with the M99 relation for $\beta \sim -1$.

5.4.3 Dust Attenuation from Composite SED Colors

Both the IRX and *UVJ* colors separate the red and blue star-forming populations effectively; therefore we can also analyze the relation between IRX and these colors. We fit our A_{1600} values derived from the IRX$-\beta$ fits to the rest-frame colors (Figure 5.4). The resulting linear relations

are

$$A_{1600} = (3.64 \pm 0.23)(U-V)_{\rm REST} - (0.43 \pm 0.24) \quad (5.3)$$

$$A_{1600} = (2.86 \pm 0.30)(V-J)_{\rm REST} + (0.58 \pm 0.30), \quad (5.4)$$

which can be used in conjunction with the IRX$-A_{1600}$ relation to obtain

$$\text{IRX} = 1.68 \times [10^{0.4(3.64(U-V)_{\rm REST}-0.43)} - 1] \quad (5.5)$$

$$\text{IRX} = 1.68 \times [10^{0.4(2.86(V-J)_{\rm REST}+0.58)} - 1]. \quad (5.6)$$

Our derived A_{1600} for star-forming galaxies correlates well with the *(U-V)*$_{\rm REST}$ color, as can be seen in the upper central panel of Figure 5.4, allowing it to be used as a proxy for UV dust attenuation at these redshifts for all but the reddest star-forming galaxies. Because rest-frame colors are fairly easily determined, these relations provide a useful way to estimate dust corrections for star-forming galaxies without requiring a spectrum.

Table 5.1: Fit parameters of the IRX$-\beta$ relation.[a]

Paper	q	δq	r	δr	Sample
This Work	5.05	0.16	2.39	0.14	$1 < z < 3$ composite SEDs
Meurer 1999	4.43	0.08	1.99	0.04	local starbursts
Penner 2012	5.94	–	2.34	–	$z \sim 2$ DOGs, 24 μm-selected (61)
Casey 2014	3.36	0.10	2.04	0.08	$z < 0.085$, IRX<60
Talia 2015	3.33	0.24	1.10	0.23	$1 < z < 3$ SFG spectra (62)

We use the above relations to derive the direction of the unit vector of IRX and A_{1600} on the *UVJ* diagram. While the IRX trend more or less parallels the distribution of the star-forming composite SEDs, it is apparent that the A_{1600} vector on the *UVJ* diagram does not parallel the color evolution of star-forming galaxies as A_V does Wuyts et al. (2007); Williams et al. (2009).

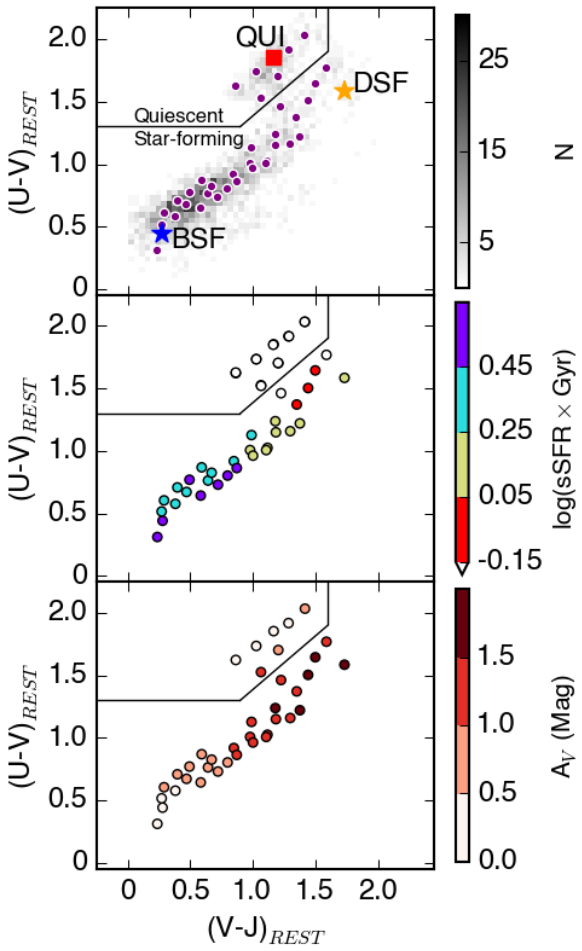

Figure 5.2: Composite SEDs on the *UVJ* diagram. The top panel shows the distribution of the parent sample (greyscale) behind the composite SEDs (purple). The example quiescent (red square), blue star-forming (blue star), and dusty star-forming (yellow star) composite SEDs shown in Figure 5.1 are labeled as well. The middle and bottom panels show the composite SEDs colored by the logarithm of the sSFR and A_V from SED-fitting, respectively. The composite SEDs show known trends with sSFR and A_V as quiescent composite SEDs have much smaller sSFR values, and dusty star-forming composite SEDs have the greatest amount of dust attenuation.

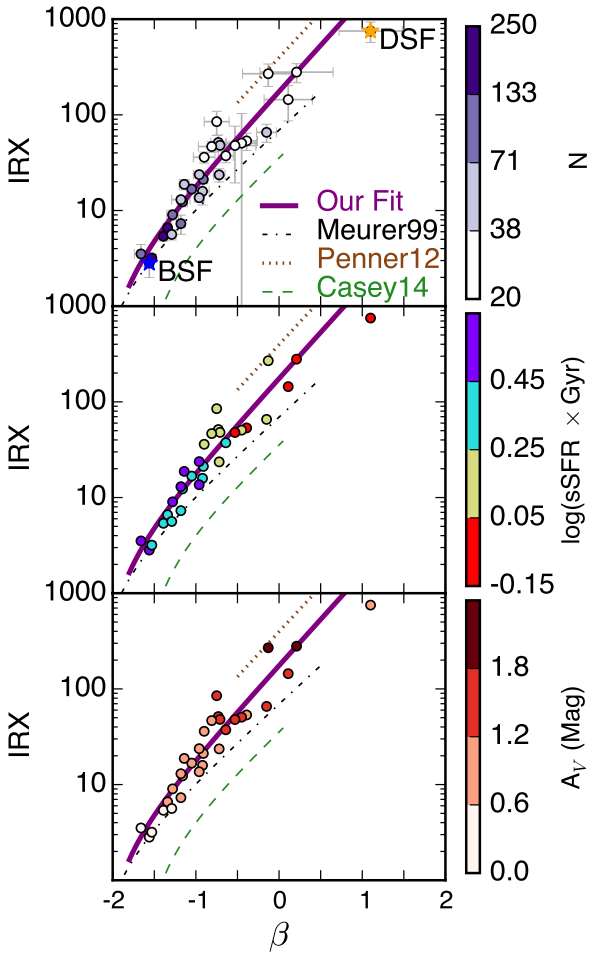

Figure 5.3: Star-forming composite SEDs on the IRX$-\beta$ diagram. Star-formation selection is based on *UVJ* position. The point colors correspond to the number of analog galaxies (purple), the logarithm of the sSFR (rainbow), and the A_V (red) from SED-fitting. Also shown are two local fits - Meurer et al. (1999) (black dashed-dotted line) and Casey et al. (2014) (green dashed line) - and two fits to $z \sim 2$ data - this work (purple line) and a fit to the median points of Penner et al. (2012) (brown dotted line). Our dusty star-forming composite SEDs lie systematically above these local relations, appearing bluer than expected for their IR fluxes.

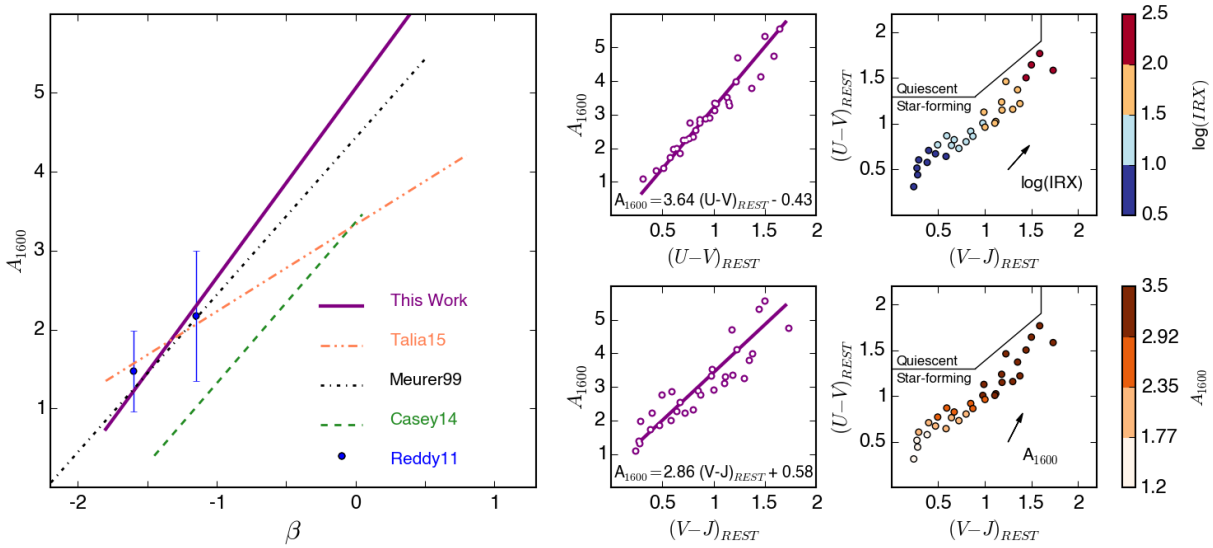

Figure 5.4: Dust-color relations. A comparison of different extinction relations from literature $A_{1600}-\beta$ fits is shown on the left panel. The $z \sim 2$ LBG stacks from Reddy et al. (2012a) are shown as blue points, which are consistent with several relations within the errorbars. While galaxies with steeper UV slopes are in general agreement, our dusty star-forming composite SEDs show more extinction than would be determined from local relations. Fit relations between our derived A_{1600} and *UVJ* rest-frame colors are shown in the middle column. These relations advocate the use of rest-frame optical colors to probe UV dust attenuation at these redshifts. The right panels show the *UVJ* diagrams color-coded by IRX and A_{1600}, with unit vectors for each parameter showing the effects of increasing the dust content.

6. SUMMARY

Work for this dissertation has added to our scientific understanding of galaxy evolution throughout cosmic history. While many details remain murky, the general picture has become much clearer over the last several decades. Most galaxies at high redshift have limited data available and in this work we focus on maximizing the utility of this data through population studies. In so doing, we have constrained identified multiple quenching pathways, characterized the youngest, most actively star-forming galaxies, and identified the average dust attenuation over $1 < z < 4$. Further work on these fronts will aid simulations in their efforts to reproduce observations, thus improving our theoretical knowledge of galaxy life cycles.

6.1 Galaxies in Transition at $1 < z < 4$

In this work we have classified ~ 7000 galaxies from ZFOURGE based on UV to near-IR rest-frame colors and spectral feature similarities. Building composite SEDs allowed us to leverage the large amount of multi-wavelength photometry and accurate photometric redshifts from ZFOURGE for galaxies across a broad redshift range, $1 < z < 4$. These composite SEDs show a wide range of properties and independently yield predicted relations based on emission line equivalent widths, sizes, masses, and number densities. Also, building composite SEDs aided in the identification of rare populations in our sample, as well as characterization of properties that are not typically available with photometry alone.

We identified a number of galaxies showing considerable nebular emission due to vigorous star formation. Galaxies with extreme nebular emission, [O III]+Hβ $EW_{\rm REST}$ from several hundred to over one thousand angstroms, are increasingly common at higher redshifts, making up $\sim 25\%$ of the star-forming galaxies in our sample at $3.5 < z < 4$. For star-forming galaxies of a given mass, the typical [O III]+Hβ $EW_{\rm REST}$ at $2.5 < z < 4$ is $2-3$ times that of galaxies at $1 < z < 3$. These galaxies also have $D(4000) \lesssim 1$, consistent with populations dominated by massive, young O and B stars.

Additionally we find evidence for galaxies with at least two quenching patterns. Most of these transitional galaxies (TGs) show Hα emission with $EW_{\rm REST} \sim 30$Å, star formation rates ~ 1.5 dex beneath the star-formation stellar mass relation, effective radii half that of SFGs of similar mass, Sérsic indices of $2-3$ increasing with mass, and colors that lie on the boundary between quiescent and star forming galaxies on the *UVJ* diagram. The majority of these transitional galaxies have masses $10 < \log_{10}(M/M_{\odot}) < 11$, but several with masses $\log_{10}(M/M_{\odot}) < 9.5$ exist by $z \sim 1$.

The other class of these galaxies is consistent with the classical 'post-starburst' (PSB) regime. These have small (1/3 the effective radii of star forming galaxies at similar mass), bulge-dominated ($n \sim 3-4$) morphologies consistent with quiescent galaxies, no nebular emission, sSFRs just above the quiescent regime, but also bluer colors than quiescent galaxies at similar masses and redshifts.

The greater and increasing number density of the TGs at low redshifts (0.5 dex larger than PSBs at $z = 1.25$) implies that this group/quenching pathway is becoming more common, while the post-starbursts are becoming rarer at $z < 1.5$. This is potentially due to a longer timescale associated with said pathway, on the order of 2 Gyr, a factor of $2-10$ times longer than the post-starburst phase is expected to last.

The processes that brings star-forming galaxies into the green valley generate changes in color, sSFR, size, and Sérsic index. These changes appear together, implying that morphological changes cannot precede other effects by a significant amount of time, as may be expected with morphological quenching. As a result, selecting transitional galaxies on the basis of any of these properties will yield similar results for population parameters, although individual galaxies may show differences. Further, selections based on observed properties, such as color, are preferable to those which are derived, such as specific star formation rate.

Finally, we note that post-starburst galaxy morphologies do not appear to change from $1 < z < 4$, although there is some evidence for sizes evolving from $1-1.8$ kpc with mass across $9.5 < \log_{10}(M/M_{\odot}) < 11$. Sérsic indices also increase slightly with mass, but the scatter in this

parameter is too large to conclude a trend in a statistically significant manner.

6.2 Extreme Emission Line Galaxies at $z \sim 3.5$ *

I utilized multi-wavelength photometry from the ZFOURGE survey to build composite SEDs based on similar galaxy redshift and SED shape, revealing a population of galaxies with very blue colors and excess emission in the K_s-band at $z \sim 3.5$. Parameters derived from FAST characterize these galaxies as having very young ages ($\log(\mathrm{age/yr}) \sim 7.2$), low masses ($\log(M/M_\odot) \sim 8.6$), and low dust content ($\mathrm{A_V} \sim 0.45$). In addition, they are small in size ($r_e \sim 1.3$ kpc), and their remarkable emission from [O III]+Hβ, $EW_{\mathrm{REST}} = 803 \pm 228$Å for the strongest emitters, is consistent with the properties of extreme star-forming galaxies that may have reionized the universe.

I observed that these EELGs appear on the order of 10^{-5} Mpc^{-3} at $z \sim 3.5$, and make up the vast majority (78%) of the galaxies with $\beta < -2$ at this epoch. This is in contrast to the local universe, where such objects are more than a factor of ten rarer.

Finally, I explored the distribution of these galaxies on the sky, and find an overdensity in the overall population of CDFS at $z \sim 3.5$. This giant structure is ~ 2 Mpc in projected size and is a candidate progenitor of a galaxy cluster environment. It also includes a massive quiescent galaxy from Straatman et al. (2014) and rest-frame UV spectroscopically confirmed LBGs (Vanzella et al. (2009)) in a very narrow redshift range.

6.3 The Average Dust Attenuation Law at $z \sim 2$ **

In Section 5 I empirically generated a set of 38 composite SEDs from the photometric data points of ∼4000 K_s-band selected galaxies in the redshift range $1 < z < 3$ from the mass complete ZFOURGE survey. The use of composite SEDs allowed me to densely probe the SEDs of large samples of galaxies without spectroscopy. I analyzed these galaxies using the *UVJ* diagnostic plot, and verified that this simple color−color relation test does an excellent job of separating quiescent

*Reprinted with permission from "Discovery of Extreme [OIII]+Hβ Emitting Galaxies Tracing an Overdensity at $z \sim 3.5$ in CDF-South" by Forrest et al., 2017. The Astrophysical Journal Letters, Volume 838, Issue 1, article id. L12, 6 pp., Copyright 2017 by the American Astronomical Society.

**Reprinted with permission from "UV to IR Luminosities and Dust Attenuation Determined from ∼4000 K-Selected Galaxies at $1 < z < 3$ in the ZFOURGE Survey" by Forrest et al., 2016. The Astrophysical Journal Letters, Volume 818, Issue 2, article id. L26, 6 pp., Copyright 2016 by the American Astronomical Society.

galaxies from star-forming galaxies.

In addition, I explored the IRX$-\beta$ relation, which parameterizes the dust content of galaxies, for our star-forming composite SEDs. While there is a range of results regarding IRX$-\beta$ in previous studies, this work utilized a large, mass-selected sample to derive the relation at intermediate redshifts. I found that these composite SEDs lie above the relations derived for local samples of galaxies, indicating differences in dust properties. Specifically, dusty star-forming galaxies have more dust attenuation in the UV, and are therefore intrinsically bluer, than would be derived based on calibrations from samples of non-dust obscured galaxies extending the results of previous work in the local universe to $z \sim 2$.

I also found trends with low scatter between dust attenuation and rest-frame *UVJ* colors for star-forming galaxies, which can be used to parameterize dust of star-forming galaxies without spectra. This is particularly useful for high-redshift galaxies whose apparent faintness make spectroscopy difficult.

6.4 Further Study

Many questions remain in out quest for a deeper and more complete understanding of galaxy evolution. In particular, the mechanisms which contribute to galaxy quenching must be constrained. Improving our knowledge of both the frequency and amplitude of these effects, as well as trends with mass, environment, and redshift is also necessary. Constraining the quenching timescales for each mechanism will aid in deriving these numbers, and it is likely that simulations will be of great utility here.

Observationally, progress towards these goals will largely be made on three fronts: (1) Improved understanding and incorporation of lessons from stellar evolution will enable more accurate interpretation of observations, (2) detailed and precise observations of nearby galaxies will add to our understanding of intra-galactic processes, and (3) increased numbers of high-redshift galaxy observations will offer clues as to the changes of characteristics in galaxy populations with the use of advanced computing techniques.

6.4.1 Applying Lessons from Stellar Evolution

Our knowledge of galaxy evolution has many remaining gaps, and the field of stellar evolution is similar. Because we are unable to resolve individual stars in most galaxies, answers to many of the questions stellar astronomers study are not applied to SED models as meticulously as is needed.

Over the last decade, improvements in stellar population synthesis models have enhanced the precision with which observations are matched with model spectra. The Flexible Stellar Population Synthesis code (FSPS; Conroy et al., 2009; Conroy & Gunn, 2010) offer improved fits compared to Bruzual & Charlot (2003) and Maraston (2005) by applying a flat prior to uncertain pieces of stellar evolution physics. While FSPS fits post-starburst colors well, it has trouble predicting other common observables such as D_n4000. Similarly, the Binary Population and Spectral Synthesis code (BPASS; Eldridge & Stanway, 2009; Eldridge et al., 2017) shows improvements due to a better treatment of massive binary stars, which enable bluer intrinsic properties. While this is effective for individual stellar populations, galaxies such as Wolf-Rayet galaxies are modeled ~ 0.2 mag too blue in $B - V$.

Great promise has been shown with the Prospector code (Leja et al., 2017), which analyzes a wide range of galaxy parameters using Markov Chain Monte Carlo sampling and a Bayesian framework. With a particular focus on modeling star formation histories (SFHs), Prospector has been able to fit galaxies with the FSPS models while also reproducing observables that FSPS has had difficulty with (e.g., D_n4000). Determining SFHs for galaxies such as the EELGs in Section 4 will yield information about the initial bursts of star formation in young galaxies.

With the increasing study of different quenching mechanisms and pathways, the transitional galaxies identified in Section 3 are also prime candidates for further follow-up. Using a program such as Prospector to constrain the star formation histories of these galaxies, particularly in comparison to star-forming and post-starburst galaxies, will reveal further differences between these populations and inform what is more clearly being revealed as a variety of quenching pathways (e.g. Davé et al., 2017; Nelson et al., 2017). If the TGs do indeed represent a slower quench-

ing mechanism, their SFHs should gradually decrease with time, while a faster mechanism would show a steep drop off.

6.4.2 Gaining Understanding from Local Galaxies

Nearby galaxies have the distinct advantage of the ability to resolve individual stars for the nearest, and single stellar populations for those slightly more distant. From this, effects such as stellar and AGN feedback can be analyzed more closely, as can effects of interstellar dust attenuation.

Completing a composite SED analysis on galaxies in the Sloan Digital Sky Survey (SDSS; York et al., 2000) will allow for comparison of galaxy properties and number densities with the higher redshift sample in Section 3. Combined with current work at $1 < z < 3$, tracing the number density evolution of both TGs and PSBs over $0 < z < 0.5$ yields the frequency of these galaxies over ~ 10 Gyr. A similar evolution in number density would suggest that the two galaxy populations are simply different stages of the same evolutionary pathway. Additionally, galaxies of interest in the SDSS sample can be easily followed up spectroscopically, or already have been (Blanton et al., 2017).

Combining this information with model fitting programs such as Prospector will create a strong foundational knowledge of galaxy evolution at low redshift which can be extended and compared to higher redshift samples. In particular, calibrating how long ago and how quickly a post-starburst galaxy turned off star formation, or how long bursts of star formation in extreme emission line galaxies last relative to other star formation indicators can provide tools for use with high redshift, data poor galaxies.

6.4.3 Extending Results to High Redshift with Large Samples

Work by Barro et al. (2013) and Pandya et al. (2017) supports the idea that the average timescale for galaxy quenching increases with decreasing redshift, implying different quenching pathways. While rapid quenching seen at $z \sim 3$ would be associated with mergers of gas-rich galaxies, such processes would no longer be efficient at lower redshifts (Robertson et al., 2006; Barro et al., 2013).

As a result, other processes including morphological quenching and halo quenching have time to take effect Martig et al. (2009); Gabor & Davé (2012).

Additionally, spectroscopic analysis of these galaxies provides instantaneous star formation rates through Hα emission and can aid in detection of AGN using the Baldwin-Phillips-Terlevich diagnostic (Baldwin et al., 1981). Although we have removed galaxies with obvious signs of AGN activity, less luminous AGN could still play a role in TGs, especially at high redshift where AGN feedback can play a role in fast galaxy quenching (Gabor & Davé, 2012). Furthermore, the strength of emission lines such as [OII]λ3727, H$\delta\lambda$4102, and H$\alpha\lambda$6563 can distinguish between phases of quenching in PSBs, as detailed in Wilkinson et al. (2017). A similar classification for TGs will further improve understanding of how quickly star formation shuts off relative to the timescales seen in simulations (e.g. Davé et al., 2017).

Further analysis of the extreme emission line galaxies at high redshift is also an area of increasing focus. Work by Naidu et al. (2018, , submitted) puts an upper limit on the Lyman continuum escape fraction of these galaxies, constraining their possible contribution to reionization. The Multi-Object Spectroscopic Emission Line (MOSEL; Tran et al., 2018, , in prep) is undertaking spectroscopic follow-up of these lines to constrain properties such as metallicity, line strength, and gas fraction. Additionally, Cohn et al. (2018, , in prep) use Prospector to obtain star formation histories, confirming that the bulk of star formation in these galaxies occurred in the last 100 Myr.

Observations will continue to improve in not only sensitivity and resolution, but also in size. Current surveys such as the Dark Energy Survey, and future projects including the James Webb Space Telescope (*JWST*), the Large Synoptic Survey Telescope, and the Giant Magellan Telescope will greatly enhance the quality and quantity of extragalactic data. These new data sets will dwarf current surveys and further enable the use of advanced statistical techniques and machine learning to glean insights about large galaxy populations.

Further spectroscopic follow-up of the emission line galaxy and transitional galaxy samples at $z \sim 3$ is critical for understanding the earliest star-forming galaxies, and will also lead to interesting science cases for the next generation of telescopes, including *JWST*. Such telescopes

would be capable of detecting Hα emission from these galaxies, which currently falls between the K-band and the *Spitzer* 3.6μm band, as well as looking for large scale structure based on optical emission lines.

REFERENCES

Abazajian, K., Adelman-McCarthy, J. K., Ageros, M. A., et al. 2003, The Astronomical Journal, 126, 2081

Allen, R. J., Kacprzak, G. G., Glazebrook, K., et al. 2017, The Astrophysical Journal, 834, L11

Almaini, O., Wild, V., Maltby, D. T., et al. 2017, Monthly Notices of the Royal Astronomical Society, 472, 1401

Atek, H., Siana, B., Scarlata, C., et al. 2011, The Astrophysical Journal, 743, 121

Baldwin, J. A., Phillips, M. M., & Terlevich, R. 1981, Publications of the Astronomical Society of the Pacific, 93, 5

Balestra, I., Mainieri, V., Popesso, P., et al. 2010, Astronomy and Astrophysics, 512, A12

Barro, G., Faber, S. M., Pérez-González, P. G., et al. 2013, The Astrophysical Journal, 765, 104

Barro, G., Kriek, M., Perez-Gonzalez, P. G., et al. 2017, 1

Behroozi, P. S., Wechsler, R. H., & Conroy, C. 2013, The Astrophysical Journal, 770, 57

Bezanson, R., Wake, D. a., Brammer, G. B., et al. 2016, The Astrophysical Journal, 822, 30

Blanton, M. R., Bershady, M. A., Abolfathi, B., et al. 2017, The Astronomical Journal, 154, 28

Brammer, G. B., van Dokkum, P. G., & Coppi, P. 2008, The Astrophysical Journal, 686, 1503

Brammer, G. B., Whitaker, K. E., van Dokkum, P. G., et al. 2009, The Astrophysical Journal, 706, L173

—. 2011, The Astrophysical Journal, 739, 24

Brammer, G. B., Sánchez-Janssen, R., Labbé, I., et al. 2012, The Astrophysical Journal, 758, L17

Brinchmann, J., Kunth, D., & Durret, F. 2008, Astronomy and Astrophysics, 485, 657

Bruzual, G., & Charlot, S. 2003, Monthly Notices of the Royal Astronomical Society, 344, 1000

Bruzual A., G. 1983, The Astrophysical Journal, 273, 105

Buat, V., Giovannoli, E., Heinis, S., et al. 2011, Astronomy & Astrophysics, 533, A93

Buat, V., Noll, S., Burgarella, D., et al. 2012, Astronomy & Astrophysics, 545, A141

Calzetti, D. 2001, Publications of the Astronomical Society of the Pacific, 113, 1449

Calzetti, D., Kinney, A. L., & Storchi-Bergmann, T. 1994, The Astrophysical Journal, 429, 582

Cardamone, C., Schawinski, K., Sarzi, M., et al. 2009, Monthly Notices of the Royal Astronomical Society, 399, 1191

Cardamone, C. N., van Dokkum, P. G., Urry, C. M., et al. 2010, The Astrophysical Journal Supplement Series, 189, 270

Casey, C. M., Scoville, N. Z., Sanders, D. B., et al. 2014, The Astrophysical Journal, 796, 95

Castellano, M., Sommariva, V., Fontana, A., et al. 2014, Astronomy & Astrophysics, 1403, 743

Chabrier, G. 2003, Publications of the Astronomical Society of the Pacific, 115, 763

Charlot, S., & Fall, S. M. 2000, The Astrophysical Journal, 539, 718

Chary, R., & Elbaz, D. 2001, The Astrophysical Journal, 556, 562

Chevallard, J., Charlot, S., Wandelt, B., & Wild, V. 2013, Monthly Notices of the Royal Astronomical Society, 432, 2061

Ciesla, L., Elbaz, D., & Fensch, J. 2017, Astronomy & Astrophysics, 608, A41

Coe, D., Zitrin, A., Carrasco, M., et al. 2013, Astrophysical Journal, 762, arXiv:1211.3663

Cohn, J. H., Leja, J., Tran, K.-v. H., et al. 2018, 1

Conroy, C., & Gunn, J. E. 2010, The Astrophysical Journal, 712, 833

Conroy, C., Gunn, J. E., & White, M. 2009, The Astrophysical Journal, 699, 486

Couch, W. J., & Sharples, R. M. 1987, Monthly Notices of the Royal Astronomical Society, 423

Cowie, L. L., & Hu, E. M. 1998, The Astronomical Journal, 115, 1319

Cowley, M. J., Spitler, L. R., Tran, K.-V. H., et al. 2016, Monthly Notices of the Royal Astronomical Society, 457, 629

Darvish, B., Mobasher, B., Sobral, D., et al. 2016, The Astrophysical Journal, 825, 1

Davé, R., Rafieferantsoa, M. H., & Thompson, R. J. 2017, Monthly Notices of the Royal Astronomical Society, 471, 1671

de Barros, S., Vanzella, E., Amorín, R., et al. 2016, Astronomy & Astrophysics, 585, A51

Dickey, C. M., van Dokkum, P. G., Oesch, P. A., et al. 2016, The Astrophysical Journal, 828, L11

Draine, B. 2003, Annual Review of Astronomy and Astrophysics, 41, 241

Dressler, A., & Gunn, J. E. 1983, The Astrophysical Journal, 270, 7

Eales, S., de Vis, P., W. L. Smith, M., et al. 2017, Monthly Notices of the Royal Astronomical Society, 465, 3125

Eales, S., Smith, D., Bourne, N., et al. 2018, Monthly Notices of the Royal Astronomical Society, 473, 3507

Eldridge, J. J., & Stanway, E. R. 2009, Monthly Notices of the Royal Astronomical Society, 400, 1019

Eldridge, J. J., Stanway, E. R., Xiao, L., et al. 2017, Publications of the Astronomical Society of Australia, 34, e058

Erb, D. K., Pettini, M., Shapley, A. E., et al. 2010, The Astrophysical Journal, 719, 1168

Erben, T., Schirmer, M., Dietrich, J. P., et al. 2005, Astronomische Nachrichten, 326, 432

Erben, T., Hildebrandt, H., Lerchster, M., et al. 2009, Astronomy and Astrophysics, 493, 1197

Faisst, A. L., Carollo, C. M., Capak, P. L., et al. 2017, The Astrophysical Journal, 839, 71

Fang, J. J., Faber, S. M., Koo, D. C., & Dekel, A. 2013, The Astrophysical Journal, 776, 63

Fang, J. J., Faber, S. M., Salim, S., Graves, G. J., & Rich, R. M. 2012, Astrophysical Journal, 761, arXiv:1210.6062

Ferland, G. J., Korista, K. T., Verner, D. A., et al. 1998, Publications of the Astronomical Society of the Pacific, 110, 761

Fioc, M., & Rocca-Volmerange, B. 1999, eprint arXivastroph9912179, 18

Fontana, A., Dunlop, J. S., Paris, D., et al. 2014, Astronomy & Astrophysics, 570, A11

Forrest, B., Tran, K.-V. H., Tomczak, A. R., et al. 2016, The Astrophysical Journal, 818, L26

Forrest, B., Tran, K.-V. H., Broussard, A., et al. 2017, The Astrophysical Journal Letters, 838, L12

Franx, M., Labb, I., Rudnick, G., et al. 2003, The Astrophysical Journal, 587, L79

Fumagalli, M., Patel, S. G., Franx, M., et al. 2012, The Astrophysical Journal, 757, L22

Furusawa, H., Kosugi, G., Akiyama, M., et al. 2008, The Astrophysical Journal Supplement Series, 176, 1

Gabor, J. M., & Davé, R. 2012, Monthly Notices of the Royal Astronomical Society, 427, 1816

Geach, J. E., Smail, I., Best, P. N., et al. 2008, Monthly Notices of the Royal Astronomical Society, 388, 1473

Giacconi, R., Zirm, A., Wang, J., et al. 2002, The Astrophysical Journal Supplement Series, 139, 369

Giavalisco, M., Ferguson, H. C., Koekemoer, A. M., et al. 2004, The Astrophysical Journal, 600, L93

Glazebrook, K., Schreiber, C., Labbé, I., et al. 2017, Nature Publishing Group, 544, 71

Grogin, N. A., Kocevski, D. D., Faber, S. M., et al. 2011, The Astrophysical Journal Supplement Series, 197, 35

Hagen, A., Bond, N. A., Ciardullo, R., et al. 2016, arXiv:1610.01163

Henry, A., Scarlata, C., Martin, C. L., & Erb, D. 2015, The Astrophysical Journal, 809, 19

Hildebrandt, H., Pielorz, J., Erben, T., et al. 2009, \Aap, 498, 725

Hildebrandt, H., Erben, T., Dietrich, J. P., et al. 2006, Astronomy and Astrophysics, Volume 452, Issue 3, June IV 2006, pp.1121-1128, 452, 1121

Holden, B. P., Oesch, P. A., González, V. G., et al. 2016, The Astrophysical Journal, 820, 73

Howell, J. H., Armus, L., Mazzarella, J. M., et al. 2010, The Astrophysical Journal, 715, 572

Hsieh, B.-C., Wang, W.-H., Hsieh, C.-C., et al. 2012, The Astrophysical Journal Supplement Series, 203, 23

Hu, E. M., & McMahon, R. G. 1996, Nature, 382, 231

Inoue, A. K. 2011, Monthly Notices of the Royal Astronomical Society, 415, 2920

Izotov, Y. I., Guseva, N. G., Fricke, K. J., & Henkel, C. 2016, Monthly Notices of the Royal Astronomical Society, 462, 4427

Izotov, Y. I., Guseva, N. G., & Thuan, T. X. 2011, The Astrophysical Journal, 728, 161

Kennicutt, R. C. 1998, Annual Review of Astronomy and Astrophysics, 36, 189

Kennicutt, R. C., & Evans, N. J. 2012, Annual Review of Astronomy and Astrophysics, 50, 531

Kennicutt, R. C., Hao, C.-N., Calzetti, D., et al. 2009, The Astrophysical Journal, 703, 1672

Khostovan, A. A., Sobral, D., Mobasher, B., et al. 2016, Monthly Notices of the Royal Astronom-

ical Society, 463, 2363

Kocevski, D. D., Barro, G., Faber, S. M., et al. 2017, The Astrophysical Journal, 846, 112

Koekemoer, A. M., Faber, S. M., Ferguson, H. C., et al. 2011, The Astrophysical Journal Supplement Series, 197, 36

Kriek, M., & Conroy, C. 2013, The Astrophysical Journal, 775, L16

Kriek, M., van Dokkum, P. G., Labbé, I., et al. 2009, The Astrophysical Journal, 700, 221

Kriek, M., van Dokkum, P. G., Whitaker, K. E., et al. 2011, The Astrophysical Journal, 743, 168

Labbé, I., Huang, J., Franx, M., et al. 2005, The Astrophysical Journal, 624, L81

Labbé, I., Oesch, P. a., Bouwens, R. J., et al. 2013, The Astrophysical Journal, 777, L19

Lawrence, a., Warren, S. J., Almaini, O., et al. 2007, Monthly Notices of the Royal Astronomical Society, 379, 1599

Leja, J., Johnson, B. D., Conroy, C., van Dokkum, P. G., & Byler, N. 2017, The Astrophysical Journal, 837, 170

Madau, P., & Dickinson, M. 2014, Annual Review of Astronomy and Astrophysics, 52, 415

Maltby, D. T., Almaini, O., Wild, V., et al. 2016, 5, 1

Maraston, C. 2005, Monthly Notices of the Royal Astronomical Society, 362, 799

Martig, M., Bournaud, F., Teyssier, R., & Dekel, A. 2009, The Astrophysical Journal, 707, 250

Martin, D. C., Small, T., Schiminovich, D., et al. 2007, The Astrophysical Journal Supplement Series, 173, 415

Maseda, M. V., van der Wel, A., da Cunha, E., et al. 2013, The Astrophysical Journal, 778, L22

Maseda, M. V., van der Wel, A., Rix, H.-W., et al. 2014, The Astrophysical Journal, 791, 17

—. 2016, arXiv:1608.01674

McCracken, H. J., Milvang-Jensen, B., Dunlop, J., et al. 2012, Astronomy & Astrophysics, 544, A156

Mendez, A. J., Coil, A. L., Lotz, J., et al. 2011, The Astrophysical Journal, 736, 110

Meurer, G. R., Heckman, T. M., & Calzetti, D. 1999, The Astrophysical Journal, 521, 64

Momcheva, I. G., Brammer, G. B., van Dokkum, P. G., et al. 2016, The Astrophysical Journal

Supplement Series, 225, 27

Naidu, R. P., Forrest, B., Oesch, P. A., Tran, K.-v. H., & Holden, B. P. 2018, 1

Nakajima, K., Ellis, R. S., Iwata, I., et al. 2016, The Astrophysical Journal, 831, L9

Nakajima, K., & Ouchi, M. 2014, Monthly Notices of the Royal Astronomical Society, 442, 900

Nanayakkara, T., Glazebrook, K., Kacprzak, G. G., et al. 2016, The Astrophysical Journal, 828, 21

Nelson, D., Pillepich, A., Springel, V., et al. 2017, arXiv:1707.03395

Noll, S., Burgarella, D., Giovannoli, E., et al. 2009a, Astronomy and Astrophysics, 507, 1793

Noll, S., Pierini, D., Cimatti, A., et al. 2009b, Astronomy & Astrophysics, 499, 69

Nonino, M., Dickinson, M., Rosati, P., et al. 2009, The Astrophysical Journal Supplement Series, 183, 244

Oesch, P. A., Brammer, G., van Dokkum, P. G., et al. 2016, The Astrophysical Journal, 819, 0

Oke, J. B., & Gunn, J. E. 1983, The Astrophysical Journal, 266, 713

Ouchi, M., Shimasaku, K., Akiyama, M., et al. 2005, The Astrophysical Journal, 620, L1

Overzier, R. A., Heckman, T. M., Wang, J., et al. 2011, The Astrophysical Journal, 726, L7

Pandya, V., Brennan, R., Somerville, R. S., et al. 2017, Monthly Notices of the Royal Astronomical Society, 472, 2054

Papovich, C., Dickinson, M., & Ferguson, H. C. 2001, The Astrophysical Journal, 559, 620

Papovich, C., Momcheva, I., Willmer, C. N. A., et al. 2010, The Astrophysical Journal, 716, 1503

Papovich, C., Labbé, I., Quadri, R., et al. 2015, The Astrophysical Journal, 803, 26

Papovich, C., Kawinwanichakij, L., Quadri, R., et al. 2018, arXiv:1801.04934

Patel, S. G., Holden, B. P., Kelson, D. D., et al. 2012, The Astrophysical Journal, 748, L27

Pearson, K. 1901, Philosophical Magazine, 2, 559

Pei, Y. C. 1992, Astrophysical Journal, 395, 130

Peng, Y.-j., Lilly, S. J., Kovač, K., et al. 2010, The Astrophysical Journal, 721, 193

Penner, K., Dickinson, M., Pope, A., et al. 2012, The Astrophysical Journal, 759, 28

Penner, K., Dickinson, M., Weiner, B., et al. 2015, arXiv:1507.00728

Persson, S. E., Murphy, D. C., Smee, S., et al. 2013, Publications of the Astronomical Society of

the Pacific, 125, 654

Poggianti, B. M., & Barbaro, G. 1997, Astronomy & Astrophysics, 325, 1025

Poggianti, B. M., Aragón-Salamanca, A., Zaritsky, D., et al. 2009, The Astrophysical Journal, 693, 112

Puglisi, A., Rodighiero, G., Franceschini, A., et al. 2016, Astronomy & Astrophysics, 586, A83

Quadri, R. F., & Williams, R. J. 2010, The Astrophysical Journal, 725, 794

Rampazzo, R., Marino, A., Tantalo, R., et al. 2007, Monthly Notices of the Royal Astronomical Society, 381, 245

Reddy, N., Dickinson, M., Elbaz, D., et al. 2012a, The Astrophysical Journal, 744, 154

Reddy, N. a., Erb, D. K., Pettini, M., Steidel, C. C., & Shapley, A. E. 2010, The Astrophysical Journal, 712, 1070

Reddy, N. a., Pettini, M., Steidel, C. C., et al. 2012b, The Astrophysical Journal, 754, 25

Retzlaff, J., Rosati, P., Dickinson, M., et al. 2010, Astronomy and Astrophysics, 511, A50

Riess, A. G., Filippenko, A. V., Challis, P., et al. 1998, The Astronomical Journal, 116, 36

Robertson, B., Bullock, J. S., Cox, T. J., et al. 2006, The Astrophysical Journal, 645, 986

Robertson, B. E., Ellis, R. S., Furlanetto, S. R., & Dunlop, J. S. 2015, The Astrophysical Journal, 802, L19

Robertson, B. E., Furlanetto, S. R., Schneider, E., et al. 2013, The Astrophysical Journal, 768, 71

Roweis, S., & Saul, L. 2000, Science, 290, 2323

Salim, S., Rich, R. M., Charlot, S., et al. 2007, The Astrophysical Journal Supplement Series, 173, 267

Salmon, B., Papovich, C., Finkelstein, S. L., et al. 2015, The Astrophysical Journal, 799, 183

Salmon, B., Papovich, C., Long, J., et al. 2016, The Astrophysical Journal, 827, 20

Salmon, B., Coe, D., Bradley, L., et al. 2018, 1

Salzer, J. J., Lee, J. C., Melbourne, J., et al. 2005, The Astrophysical Journal, 624, 661

Sanders, R. L., Shapley, A. E., Kriek, M., et al. 2016, The Astrophysical Journal, 825, L23

Sargent, W. L. W., & Searle, L. 1970, The Astrophysical Journal, 162, L155

Schawinski, K., Urry, C. M., Simmons, B. D., et al. 2014, Monthly Notices of the Royal Astronomical Society, 440, 889

Schiminovich, D., Wyder, T. K., Martin, D. C., et al. 2007, The Astrophysical Journal Supplement Series, 173, 315

Scoville, N., Aussel, H., Brusa, M., et al. 2007, The Astrophysical Journal Supplement Series, 172, 1

Shapley, a. E., Steidel, C. C., Pettini, M., & Adelberger, K. L. 2003, The Astrophysical Journal, 588, 65

Skelton, R. E., Whitaker, K. E., Momcheva, I. G., et al. 2014, The Astrophysical Journal Supplement Series, 214, 24

Smit, R., Bouwens, R. J., Labbé, I., et al. 2015, The Astrophysical Journal, 833, 1

—. 2014, The Astrophysical Journal, 784, 58

Sobral, D., Smail, I., Best, P. N., et al. 2013, Monthly Notices of the Royal Astronomical Society, 428, 1128

Sparre, M., Hayward, C. C., Springel, V., et al. 2015, Monthly Notices of the Royal Astronomical Society, 447, 3548

Spitler, L. R., Labbé, I., Glazebrook, K., et al. 2012, The Astrophysical Journal, 748, L21

Stark, D. P., Schenker, M. a., Ellis, R., et al. 2013, The Astrophysical Journal, 763, 129

Stark, D. P., Richard, J., Siana, B., et al. 2014, Monthly Notices of the Royal Astronomical Society, 445, 3200

Steidel, C. C., Adelberger, K. L., Dickinson, M., et al. 1998, The Astrophysical Journal, 492, 428

Straatman, C. M. S., Labbé, I., Spitler, L. R., et al. 2014, The Astrophysical Journal, 783, L14

Straatman, C. M. S., Spitler, L. R., Quadri, R. F., et al. 2016, The Astrophysical Journal, 830, 51

Tacchella, S., Dekel, A., Carollo, C. M., et al. 2016, Monthly Notices of the Royal Astronomical Society, 457, 2790

Takeuchi, T. T., Yuan, F.-T., Ikeyama, A., Murata, K. L., & Inoue, A. K. 2012, The Astrophysical Journal, 755, 144

Talia, M., Cimatti, A., Pozzetti, L., et al. 2015, Astronomy & Astrophysics, 582, A80

Taniguchi, Y., Scoville, N., Murayama, T., et al. 2007, The Astrophysical Journal Supplement Series, 172, 9

Teplitz, H. I., Malkan, M. a., & McLean, I. S. 1999, The Astrophysical Journal, 514, 33

Tomczak, A. R., Quadri, R. F., Tran, K.-v. H., et al. 2016, The Astrophysical Journal, 817, 118

Trainor, R. F., Strom, A. L., Steidel, C. C., & Rudie, G. C. 2016, The Astrophysical Journal, 832, 171

Tran, K.-V. H., Franx, M., Illingworth, G., Kelson, D. D., & van Dokkum, P. 2003, The Astrophysical Journal, 599, 865

Tran, K.-v. H., Franx, M., Illingworth, G. D., et al. 2004, The Astrophysical Journal, 609, 683

Tran, K.-v. H., Forrest, B., Alcorn, L., et al. 2018, 1

Trayford, J. W., Theuns, T., Bower, R. G., et al. 2016, Monthly Notices of the Royal Astronomical Society, 460, 3925

Tress, M., Mármol-Queraltó, E., Ferreras, I., et al. 2018, 13, 1

Utomo, D., Kriek, M., Labbé, I., Conroy, C., & Fumagalli, M. 2014, The Astrophysical Journal, 783, L30

van der Wel, A., Straughn, a. N., Rix, H.-W., et al. 2011, The Astrophysical Journal, 742, 111

van der Wel, A., Bell, E. F., Häussler, B., et al. 2012, The Astrophysical Journal Supplement Series, 203, 24

van Dokkum, P. G., Labbé, I., Marchesini, D., et al. 2009, Publications of the Astronomical Society of the Pacific, 121, 2

van Dokkum, P. G., Brammer, G., Fumagalli, M., et al. 2011, The Astrophysical Journal, 743, L15

Vanderplas, J., & Connolly, A. 2009, The Astronomical Journal, 138, 1365

Vanzella, E., Giavalisco, M., Dickinson, M., et al. 2009, The Astrophysical Journal, 695, 1163

Vanzella, E., de Barros, S., Castellano, M., et al. 2015, Astronomy & Astrophysics, 576, A116

Whitaker, K. E., Kriek, M., van Dokkum, P. G., et al. 2012a, The Astrophysical Journal, 745, 179

Whitaker, K. E., van Dokkum, P. G., Brammer, G., & Franx, M. 2012b, The Astrophysical Journal,

754, L29

Whitaker, K. E., Labbé, I., van Dokkum, P. G., et al. 2011, The Astrophysical Journal, 735, 86

Wild, V., Almaini, O., Dunlop, J., et al. 2016, Monthly Notices of the Royal Astronomical Society, 463, 832

Wild, V., Almaini, O., Cirasuolo, M., et al. 2014, Monthly Notices of the Royal Astronomical Society, 440, 1880

Wilkinson, C. L., Pimbblet, K. A., & Stott, J. P. 2017, Monthly Notices of the Royal Astronomical Society, 472, 1447

Williams, R. J., Quadri, R. F., Franx, M., van Dokkum, P., & Labbé, I. 2009, The Astrophysical Journal, 691, 1879

Windhorst, R. A., Cohen, S. H., Hathi, N. P., et al. 2011, The Astrophysical Journal Supplement Series, 193, 27

Wold, S., Esbensen, K., & Geladi, P. 1987, Chemometrics and Intelligent Laboratory Systems, 2, 37

Wuyts, S., Labbé, I., Förster Schreiber, N. M., et al. 2008, The Astrophysical Journal, 682, 985

Wuyts, S., Labbe, I., Franx, M., et al. 2007, The Astrophysical Journal, 655, 51

Wyder, T. K., Martin, D. C., Schiminovich, D., et al. 2007, The Astrophysical Journal Supplement Series, 173, 293

Yano, M., Kriek, M., van der Wel, A., & Whitaker, K. E. 2016, The Astrophysical Journal, 817, L21

York, D. G., Adelman, J., Anderson, Jr., J. E., et al. 2000, The Astronomical Journal, 120, 1579

Zolotov, A., Dekel, A., Mandelker, N., et al. 2015a, Monthly Notices of the Royal Astronomical Society, 450, 2327

—. 2015b, Monthly Notices of the Royal Astronomical Society, 450, 2327

APPENDIX A

SUPPLEMENTAL MATERIAL FOR SECTION 3

In this Appendix, we present the composite SEDs and their associated properties. We first list the properties derived from the composite SEDs themselves, such as equivalent widths and UV slopes in Table A.1 (Table A.2) for the $1 < z < 3$ ($2.5 < z < 4$) composite SEDs. Next are the parameters derived for individual galaxies that make up a composite SED, for which the medians, 16^{th} percentile, and 84^{th} percentile are given. In the case of morphological parameters, median absolute deviations are provided, to minimize errors due to resolution limits. These are given in Table A.3 (Table A.4). Finally, plots of the composite SEDs are shown in scaled F_λ-wavelength, all labeled with a composite id number. For most of the composite SEDs, these are shown in individual panels, colored and separated into their classes as described in the text. The exception to this is the SFGs at $1 < z < 3$, which are three to a panel. Composite SEDs are ordered by UV slope.

Table A.1: Parameters Derived From Composite SEDs at $1.0 < z < 3.0$.

Cid	Class	N_{gal}	$EW_{[OIII]+H\beta}$ (Å)	$EW_{H\alpha+[NII]}$ (Å)	$D(4000)$	β
0	ELG	14	1170^{+40}_{-40}	1215^{+88}_{-88}	$0.90^{+0.01}_{-0.01}$	$-2.35^{+0.04}_{-0.04}$
1	SFG	323	265^{+11}_{-11}	277^{+20}_{-22}	$1.06^{+0.01}_{-0.01}$	$-2.00^{+0.02}_{-0.02}$
2	ELG	22	461^{+14}_{-14}	282^{+28}_{-29}	$1.10^{+0.01}_{-0.01}$	$-1.95^{+0.05}_{-0.05}$
3	SFG	62	102^{+12}_{-11}	183^{+21}_{-22}	$1.13^{+0.03}_{-0.03}$	$-1.87^{+0.03}_{-0.03}$
4	SFG	577	159^{+13}_{-12}	224^{+28}_{-29}	$1.14^{+0.02}_{-0.02}$	$-1.85^{+0.03}_{-0.03}$
5	SFG	537	132^{+14}_{-14}	188^{+35}_{-36}	$1.16^{+0.01}_{-0.01}$	$-1.75^{+0.03}_{-0.03}$
6	SFG	60	36^{+10}_{-10}	111^{+25}_{-26}	$1.27^{+0.03}_{-0.03}$	$-1.74^{+0.03}_{-0.03}$
7	SFG	28	135^{+14}_{-14}	233^{+34}_{-35}	$1.14^{+0.06}_{-0.07}$	$-1.72^{+0.03}_{-0.03}$
8	SFG	51	81^{+10}_{-10}	121^{+13}_{-16}	$1.17^{+0.01}_{-0.02}$	$-1.67^{+0.05}_{-0.05}$
9	SFG	34	227^{+23}_{-23}	254^{+64}_{-64}	$1.19^{+0.01}_{-0.01}$	$-1.67^{+0.05}_{-0.05}$

Table A.1: Continued

Cid	Class	N_{gal}	$EW_{[OIII]+H\beta}$ (Å)	$EW_{H\alpha+[NII]}$ (Å)	$D(4000)$	β
10	SFG	610	102^{+10}_{-10}	178^{+15}_{-17}	$1.19^{+0.01}_{-0.02}$	$-1.60^{+0.04}_{-0.04}$
11	SFG	419	88^{+11}_{-11}	202^{+21}_{-23}	$1.20^{+0.03}_{-0.03}$	$-1.54^{+0.04}_{-0.04}$
12	SFG	503	79^{+12}_{-12}	173^{+28}_{-29}	$1.21^{+0.03}_{-0.04}$	$-1.53^{+0.04}_{-0.04}$
13	SFG	134	39^{+10}_{-10}	124^{+15}_{-17}	$1.26^{+0.00}_{-0.00}$	$-1.50^{+0.05}_{-0.05}$
14	SFG	37	37^{+20}_{-20}	135^{+65}_{-65}	$1.31^{+0.01}_{-0.01}$	$-1.45^{+0.07}_{-0.07}$
15	SFG	61	20^{+10}_{-10}	126^{+15}_{-17}	$1.29^{+0.04}_{-0.05}$	$-1.40^{+0.07}_{-0.07}$
16	SFG	41	24^{+15}_{-15}	147^{+40}_{-41}	$1.29^{+0.06}_{-0.07}$	$-1.40^{+0.08}_{-0.08}$
17	SFG	241	82^{+10}_{-10}	164^{+13}_{-15}	$1.22^{+0.01}_{-0.01}$	$-1.39^{+0.04}_{-0.04}$
18	SFG	71	38^{+13}_{-12}	130^{+54}_{-55}	$1.27^{+0.04}_{-0.04}$	$-1.38^{+0.06}_{-0.06}$
19	SFG	31	17^{+10}_{-10}	130^{+13}_{-16}	$1.33^{+0.02}_{-0.02}$	$-1.37^{+0.08}_{-0.08}$
20	SFG	20	14^{+12}_{-11}	72^{+24}_{-26}	$1.40^{+0.04}_{-0.05}$	$-1.37^{+0.09}_{-0.09}$
21	SFG	145	50^{+14}_{-13}	142^{+39}_{-40}	$1.27^{+0.05}_{-0.06}$	$-1.33^{+0.06}_{-0.06}$
22	SFG	60	26^{+10}_{-10}	137^{+13}_{-16}	$1.30^{+0.01}_{-0.02}$	$-1.32^{+0.07}_{-0.07}$
23	SFG	132	101^{+10}_{-10}	199^{+36}_{-37}	$1.21^{+0.03}_{-0.04}$	$-1.32^{+0.05}_{-0.05}$
24	SFG	107	40^{+13}_{-12}	128^{+31}_{-32}	$1.29^{+0.02}_{-0.03}$	$-1.30^{+0.07}_{-0.07}$
25	SFG	21	16^{+13}_{-13}	103^{+35}_{-37}	$1.52^{+0.02}_{-0.02}$	$-1.28^{+0.07}_{-0.07}$
26	SFG	97	61^{+13}_{-13}	146^{+37}_{-38}	$1.27^{+0.02}_{-0.02}$	$-1.27^{+0.05}_{-0.05}$
27	SFG	53	29^{+17}_{-17}	135^{+52}_{-53}	$1.35^{+0.03}_{-0.03}$	$-1.16^{+0.08}_{-0.08}$
28	SFG	24	2^{+19}_{-18}	89^{+74}_{-75}	$1.67^{+0.05}_{-0.07}$	$-1.16^{+0.41}_{-0.41}$
29	SFG	20	-17^{+12}_{-12}	95^{+26}_{-27}	$1.38^{+0.03}_{-0.03}$	$-1.15^{+0.10}_{-0.10}$
30	SFG	107	37^{+13}_{-13}	123^{+38}_{-39}	$1.31^{+0.05}_{-0.06}$	$-1.15^{+0.08}_{-0.08}$
31	SFG	24	46^{+17}_{-16}	118^{+44}_{-45}	$1.36^{+0.05}_{-0.06}$	$-1.13^{+0.13}_{-0.13}$
32	SFG	77	64^{+13}_{-13}	178^{+33}_{-34}	$1.25^{+0.02}_{-0.02}$	$-1.11^{+0.06}_{-0.06}$
33	SFG	25	-14^{+44}_{-44}	110^{+182}_{-182}	$1.40^{+0.02}_{-0.02}$	$-1.11^{+0.12}_{-0.12}$

Table A.1: Continued

Cid	Class	N_{gal}	$EW_{[OIII]+H\beta}$ (Å)	$EW_{H\alpha+[NII]}$ (Å)	D(4000)	β
34	SFG	46	18^{+10}_{-10}	113^{+13}_{-15}	$1.31^{+0.02}_{-0.02}$	$-1.11^{+0.07}_{-0.07}$
35	SFG	38	3^{+11}_{-11}	132^{+22}_{-23}	$1.37^{+0.02}_{-0.03}$	$-1.10^{+0.09}_{-0.09}$
36	SFG	66	75^{+14}_{-14}	137^{+31}_{-32}	$1.27^{+0.02}_{-0.02}$	$-1.10^{+0.05}_{-0.05}$
37	SFG	50	48^{+11}_{-10}	178^{+15}_{-17}	$1.29^{+0.01}_{-0.01}$	$-1.08^{+0.05}_{-0.05}$
38	SFG	30	13^{+13}_{-12}	100^{+26}_{-27}	$1.42^{+0.03}_{-0.03}$	$-0.99^{+0.10}_{-0.10}$
39	SFG	26	6^{+10}_{-10}	125^{+20}_{-22}	$1.37^{+0.01}_{-0.02}$	$-0.97^{+0.10}_{-0.10}$
40	TG	21	38^{+10}_{-10}	38^{+13}_{-16}	$1.62^{+0.00}_{-0.00}$	$-0.97^{+0.12}_{-0.12}$
41	SFG	27	65^{+18}_{-18}	275^{+17}_{-19}	$1.29^{+0.06}_{-0.07}$	$-0.97^{+0.10}_{-0.10}$
42	SFG	36	26^{+10}_{-9}	179^{+26}_{-28}	$1.26^{+0.01}_{-0.01}$	$-0.97^{+0.07}_{-0.07}$
43	SFG	52	69^{+10}_{-10}	139^{+14}_{-17}	$1.30^{+0.01}_{-0.01}$	$-0.96^{+0.07}_{-0.07}$
44	SFG	37	9^{+12}_{-12}	109^{+31}_{-32}	$1.37^{+0.02}_{-0.03}$	$-0.89^{+0.09}_{-0.09}$
45	SFG	21	71^{+31}_{-30}	177^{+121}_{-122}	$1.29^{+0.03}_{-0.03}$	$-0.87^{+0.09}_{-0.09}$
46	SFG	50	68^{+22}_{-22}	203^{+70}_{-70}	$1.28^{+0.04}_{-0.05}$	$-0.87^{+0.09}_{-0.09}$
47	SFG	54	16^{+17}_{-16}	112^{+56}_{-57}	$1.38^{+0.10}_{-0.11}$	$-0.86^{+0.06}_{-0.06}$
48	SFG	47	33^{+20}_{-20}	106^{+69}_{-69}	$1.43^{+0.01}_{-0.02}$	$-0.70^{+0.13}_{-0.13}$
49	SFG	28	1^{+19}_{-19}	90^{+52}_{-53}	$1.50^{+0.00}_{-0.00}$	$-0.69^{+0.23}_{-0.23}$
50	SFG	26	7^{+15}_{-14}	49^{+36}_{-37}	$1.39^{+0.01}_{-0.01}$	$-0.63^{+0.08}_{-0.08}$
51	SFG	30	25^{+12}_{-11}	87^{+30}_{-31}	$1.45^{+0.07}_{-0.09}$	$-0.55^{+0.12}_{-0.12}$
52	TG	29	14^{+19}_{-18}	39^{+52}_{-52}	$1.59^{+0.05}_{-0.06}$	$-0.39^{+0.11}_{-0.11}$
53	SFG	35	-19^{+10}_{-10}	60^{+27}_{-28}	$1.51^{+0.03}_{-0.03}$	$-0.38^{+0.26}_{-0.26}$
54	TG	38	39^{+11}_{-10}	46^{+19}_{-20}	$1.50^{+0.10}_{-0.13}$	$-0.38^{+0.12}_{-0.12}$
55	SFG	29	-11^{+17}_{-17}	92^{+68}_{-68}	$1.48^{+0.10}_{-0.12}$	$-0.35^{+0.27}_{-0.27}$
56	SFG	28	16^{+23}_{-23}	89^{+75}_{-75}	$1.49^{+0.09}_{-0.11}$	$-0.34^{+0.11}_{-0.11}$
57	SFG	20	2^{+15}_{-15}	30^{+38}_{-38}	$1.60^{+0.08}_{-0.08}$	$-0.30^{+0.26}_{-0.26}$

Table A.1: Continued

Cid	Class	N_{gal}	$EW_{[OIII]+H\beta}$ (Å)	$EW_{H\alpha+[NII]}$ (Å)	$D(4000)$	β
58	SFG	32	-24^{+20}_{-20}	58^{+68}_{-68}	$1.44^{+0.04}_{-0.04}$	$-0.23^{+0.16}_{-0.16}$
59	TG	52	23^{+12}_{-12}	23^{+25}_{-26}	$1.70^{+0.04}_{-0.05}$	$-0.23^{+0.12}_{-0.12}$
60	SFG	27	-4^{+33}_{-33}	71^{+52}_{-53}	$1.51^{+0.03}_{-0.04}$	$-0.18^{+0.17}_{-0.17}$
61	TG	30	43^{+12}_{-11}	50^{+23}_{-24}	$1.62^{+0.03}_{-0.04}$	$0.06^{+0.24}_{-0.24}$
62	SFG	33	21^{+14}_{-14}	100^{+29}_{-31}	$1.60^{+0.03}_{-0.03}$	$0.26^{+0.23}_{-0.23}$
63	TG	20	47^{+17}_{-17}	56^{+56}_{-57}	$1.52^{+0.02}_{-0.02}$	$0.58^{+0.22}_{-0.22}$
64	QG	31	15^{+11}_{-11}	1^{+22}_{-24}	$1.84^{+0.10}_{-0.11}$	$0.67^{+0.32}_{-0.32}$
65	PSB	58	1^{+14}_{-14}	1^{+37}_{-38}	$1.69^{+0.08}_{-0.10}$	$1.03^{+0.17}_{-0.17}$
66	QG	70	10^{+11}_{-11}	2^{+28}_{-29}	$1.77^{+0.08}_{-0.10}$	$1.04^{+0.22}_{-0.22}$
67	SFG	25	12^{+11}_{-11}	93^{+22}_{-23}	$1.64^{+0.04}_{-0.05}$	$1.04^{+0.26}_{-0.26}$
68	QG	82	-4^{+11}_{-11}	-11^{+24}_{-25}	$1.84^{+0.07}_{-0.09}$	$1.13^{+0.48}_{-0.48}$
69	PSB	59	-35^{+10}_{-10}	-27^{+16}_{-18}	$1.73^{+0.08}_{-0.08}$	$1.29^{+0.16}_{-0.16}$
70	QG	67	-4^{+10}_{-10}	5^{+13}_{-16}	$1.75^{+0.11}_{-0.14}$	$1.39^{+0.20}_{-0.20}$
71	QG	110	13^{+10}_{-10}	2^{+14}_{-17}	$1.78^{+0.02}_{-0.03}$	$1.45^{+0.21}_{-0.21}$

Table A.2: Parameters Derived From Composite SEDs at $2.5 < z < 4.0$.

Cid	Class	N_{gal}	$EW_{[OIII]+H\beta}$ (Å)	$D(4000)$	β
0	ELG	19	2578^{+78}_{-89}	$0.91^{+0.00}_{-0.00}$	$-2.05^{+0.07}_{-0.07}$
1	ELG	64	755^{+5}_{-14}	$0.94^{+0.08}_{-0.10}$	$-2.00^{+0.04}_{-0.04}$
2	SFG	52	336^{+10}_{-11}	$1.16^{+0.04}_{-0.04}$	$-1.91^{+0.03}_{-0.03}$
3	ELG	22	599^{+5}_{-5}	$0.95^{+0.09}_{-0.11}$	$-1.87^{+0.13}_{-0.13}$
4	SFG	89	355^{+7}_{-8}	$1.17^{+0.03}_{-0.03}$	$-1.80^{+0.03}_{-0.03}$
5	SFG	88	224^{+10}_{-16}	$1.17^{+0.00}_{-0.00}$	$-1.69^{+0.03}_{-0.03}$
6	SFG	48	315^{+7}_{-8}	$1.97^{+0.05}_{-0.06}$	$-1.66^{+0.05}_{-0.05}$
7	SFG	37	148^{+9}_{-15}	$1.23^{+0.01}_{-0.01}$	$-1.56^{+0.05}_{-0.05}$
8	SFG	167	180^{+9}_{-10}	$1.19^{+0.02}_{-0.02}$	$-1.52^{+0.03}_{-0.03}$
9	SFG	27	100^{+10}_{-10}	$1.18^{+0.04}_{-0.04}$	$-1.49^{+0.06}_{-0.06}$
10	SFG	135	149^{+11}_{-17}	$1.24^{+0.00}_{-0.00}$	$-1.35^{+0.04}_{-0.04}$
11	SFG	76	76^{+10}_{-14}	$1.23^{+0.00}_{-0.00}$	$-1.25^{+0.04}_{-0.04}$
12	SFG	20	1^{+10}_{-11}	$1.24^{+0.06}_{-0.06}$	$-1.20^{+0.08}_{-0.08}$
13	SFG	39	89^{+9}_{-9}	$1.24^{+0.01}_{-0.01}$	$-1.11^{+0.05}_{-0.05}$
14	SFG	39	77^{+10}_{-11}	$1.28^{+0.00}_{-0.00}$	$-0.96^{+0.07}_{-0.07}$
15	SFG	22	57^{+8}_{-10}	$1.29^{+0.03}_{-0.03}$	$-0.93^{+0.13}_{-0.13}$
16	SFG	19	18^{+11}_{-13}	$1.53^{+0.10}_{-0.11}$	$-0.70^{+0.42}_{-0.42}$
17	SFG	30	27^{+12}_{-16}	$1.36^{+0.02}_{-0.02}$	$-0.51^{+0.13}_{-0.13}$
18	PSB	16	38^{+10}_{-12}	$1.60^{+0.18}_{-0.24}$	$-0.14^{+0.24}_{-0.24}$
19	PSB	28	-21^{+10}_{-11}	$1.71^{+0.09}_{-0.09}$	$0.49^{+0.28}_{-0.28}$

Table A.3: Analog Galaxy Parameters for Composite SEDs at $1.0 < z < 3.0$.

Cid	Class	$\log_{10}(M/M_{\odot})$	$sSFR\,(\mathrm{yr}^{-1})$	$\mathrm{A_V}$ (mag)	*(V-J)*	*(U-V)*	r_e (kpc)	n
0	ELG	$8.36^{+0.25}_{-0.23}$	$-7.00^{+0.03}_{-0.08}$	$0.40^{+0.10}_{-0.10}$	$-0.78^{+0.13}_{-0.08}$	$0.26^{+0.10}_{-0.05}$	0.8 ± 0.3	2.8 ± 1.9
1	SFG	$9.09^{+0.35}_{-0.45}$	$-8.35^{+1.11}_{-0.37}$	$0.30^{+0.30}_{-0.30}$	$0.07^{+0.18}_{-0.25}$	$0.30^{+0.08}_{-0.08}$	1.7 ± 0.6	1.3 ± 0.6
2	ELG	$8.79^{+0.40}_{-0.27}$	$-7.95^{+0.87}_{-0.93}$	$0.65^{+0.25}_{-0.55}$	$0.08^{+0.26}_{-0.40}$	$0.46^{+0.08}_{-0.08}$	1.5 ± 0.6	1.4 ± 0.9
3	SFG	$9.22^{+0.31}_{-0.38}$	$-8.72^{+0.24}_{-0.27}$	$0.20^{+0.20}_{-0.12}$	$0.25^{+0.10}_{-0.16}$	$0.39^{+0.07}_{-0.05}$	1.9 ± 0.6	1.2 ± 0.5
4	SFG	$9.27^{+0.31}_{-0.32}$	$-8.68^{+0.38}_{-0.32}$	$0.30^{+0.20}_{-0.20}$	$0.20^{+0.15}_{-0.18}$	$0.43^{+0.07}_{-0.07}$	2.0 ± 0.7	1.1 ± 0.5
5	SFG	$9.35^{+0.27}_{-0.35}$	$-8.83^{+0.34}_{-0.21}$	$0.30^{+0.20}_{-0.20}$	$0.26^{+0.12}_{-0.16}$	$0.52^{+0.06}_{-0.07}$	2.2 ± 0.7	1.2 ± 0.5
6	SFG	$9.54^{+0.36}_{-0.24}$	$-9.02^{+0.58}_{-0.24}$	$0.55^{+0.41}_{-0.25}$	$0.72^{+0.15}_{-0.10}$	$0.71^{+0.07}_{-0.08}$	2.8 ± 1.2	1.0 ± 0.5
7	SFG	$9.38^{+0.56}_{-0.24}$	$-8.80^{+0.64}_{-0.40}$	$0.70^{+0.30}_{-0.40}$	$0.72^{+0.15}_{-0.10}$	$0.62^{+0.05}_{-0.11}$	2.4 ± 0.7	1.2 ± 0.6
8	SFG	$9.33^{+0.33}_{-0.40}$	$-8.79^{+0.31}_{-0.41}$	$0.60^{+0.10}_{-0.40}$	$0.52^{+0.16}_{-0.11}$	$0.57^{+0.07}_{-0.09}$	2.1 ± 0.5	0.9 ± 0.4
9	SFG	$9.16^{+0.27}_{-0.23}$	$-8.93^{+0.44}_{-0.29}$	$0.40^{+0.32}_{-0.30}$	$0.24^{+0.15}_{-0.12}$	$0.59^{+0.07}_{-0.06}$	1.5 ± 0.6	1.9 ± 0.9
10	SFG	$9.48^{+0.27}_{-0.31}$	$-8.90^{+0.26}_{-0.30}$	$0.40^{+0.20}_{-0.20}$	$0.34^{+0.13}_{-0.15}$	$0.57^{+0.07}_{-0.07}$	2.3 ± 0.9	1.2 ± 0.5
11	SFG	$9.54^{+0.27}_{-0.34}$	$-8.98^{+0.32}_{-0.22}$	$0.50^{+0.20}_{-0.30}$	$0.42^{+0.11}_{-0.15}$	$0.64^{+0.07}_{-0.08}$	2.4 ± 0.9	1.3 ± 0.5
12	SFG	$9.58^{+0.33}_{-0.39}$	$-9.00^{+0.28}_{-0.23}$	$0.50^{+0.30}_{-0.20}$	$0.48^{+0.12}_{-0.15}$	$0.69^{+0.06}_{-0.07}$	2.5 ± 0.9	1.2 ± 0.5
13	SFG	$9.66^{+0.28}_{-0.26}$	$-8.99^{+0.35}_{-0.22}$	$0.80^{+0.20}_{-0.30}$	$0.70^{+0.11}_{-0.09}$	$0.77^{+0.07}_{-0.07}$	2.8 ± 1.1	1.0 ± 0.4
14	SFG	$9.70^{+0.27}_{-0.32}$	$-9.21^{+0.31}_{-0.43}$	$0.60^{+0.40}_{-0.40}$	$0.73^{+0.11}_{-0.11}$	$0.97^{+0.05}_{-0.08}$	2.8 ± 1.4	1.5 ± 0.6
15	SFG	$9.87^{+0.32}_{-0.28}$	$-8.99^{+0.27}_{-0.21}$	$0.90^{+0.24}_{-0.30}$	$0.82^{+0.08}_{-0.07}$	$0.89^{+0.05}_{-0.08}$	2.8 ± 0.8	1.0 ± 0.5
16	SFG	$10.02^{+0.38}_{-0.42}$	$-8.91^{+0.34}_{-0.28}$	$1.00^{+0.30}_{-0.20}$	$1.02^{+0.07}_{-0.13}$	$0.86^{+0.05}_{-0.07}$	3.3 ± 1.2	0.9 ± 0.5

Table A.3: Continued

Cid	Class	$\log_{10}(M/M_{\odot})$	$sSFR\,(\mathrm{yr}^{-1})$	$\mathrm{A_V}$ (mag)	*(V-J)*	*(U-V)*	r_e (kpc)	n
17	SFG	$9.64^{+0.34}_{-0.30}$	$-9.00^{+0.23}_{-0.40}$	$0.70^{+0.20}_{-0.30}$	$0.53^{+0.11}_{-0.14}$	$0.75^{+0.06}_{-0.08}$	2.4 ± 1.0	1.4 ± 0.6
18	SFG	$9.88^{+0.26}_{-0.40}$	$-8.99^{+0.31}_{-0.21}$	$0.80^{+0.30}_{-0.20}$	$0.83^{+0.11}_{-0.09}$	$0.82^{+0.06}_{-0.06}$	3.4 ± 1.2	1.0 ± 0.4
19	SFG	$10.22^{+0.26}_{-0.58}$	$-9.12^{+0.50}_{-0.23}$	$1.10^{+0.42}_{-0.20}$	$1.17^{+0.12}_{-0.05}$	$0.99^{+0.07}_{-0.08}$	4.0 ± 0.9	0.7 ± 0.2
20	SFG	$9.79^{+0.35}_{-0.45}$	$-9.41^{+0.20}_{-0.33}$	$0.60^{+0.20}_{-0.40}$	$0.78^{+0.05}_{-0.05}$	$1.06^{+0.06}_{-0.04}$	2.2 ± 0.5	1.6 ± 0.7
21	SFG	$9.79^{+0.28}_{-0.35}$	$-8.99^{+0.27}_{-0.22}$	$0.90^{+0.10}_{-0.30}$	$0.68^{+0.10}_{-0.10}$	$0.83^{+0.06}_{-0.07}$	2.9 ± 1.0	1.1 ± 0.4
22	SFG	$10.00^{+0.35}_{-0.34}$	$-8.99^{+0.21}_{-0.25}$	$1.15^{+0.15}_{-0.25}$	$0.99^{+0.07}_{-0.06}$	$0.96^{+0.05}_{-0.08}$	3.4 ± 0.9	1.1 ± 0.4
23	SFG	$9.70^{+0.27}_{-0.37}$	$-9.17^{+0.27}_{-0.37}$	$0.50^{+0.20}_{-0.20}$	$0.38^{+0.11}_{-0.12}$	$0.68^{+0.05}_{-0.07}$	2.2 ± 0.8	1.3 ± 0.5
24	SFG	$9.96^{+0.30}_{-0.37}$	$-9.00^{+0.19}_{-0.23}$	$1.00^{+0.20}_{-0.30}$	$0.84^{+0.09}_{-0.09}$	$0.93^{+0.06}_{-0.06}$	3.3 ± 1.2	1.2 ± 0.6
25	SFG	$10.19^{+0.43}_{-0.62}$	$-9.93^{+0.37}_{-0.18}$	$0.60^{+0.58}_{-0.30}$	$0.99^{+0.08}_{-0.07}$	$1.33^{+0.06}_{-0.05}$	1.8 ± 0.9	2.4 ± 0.7
26	SFG	$9.81^{+0.28}_{-0.42}$	$-9.17^{+0.36}_{-0.43}$	$0.70^{+0.20}_{-0.20}$	$0.57^{+0.10}_{-0.14}$	$0.75^{+0.07}_{-0.06}$	2.4 ± 0.7	1.3 ± 0.6
27	SFG	$10.27^{+0.22}_{-0.42}$	$-9.20^{+0.27}_{-0.44}$	$1.40^{+0.20}_{-0.40}$	$1.08^{+0.08}_{-0.06}$	$1.14^{+0.06}_{-0.06}$	3.4 ± 0.9	0.9 ± 0.4
28	SFG	$10.71^{+0.31}_{-0.33}$	$-10.36^{+0.31}_{-1.56}$	$1.75^{+0.85}_{-0.25}$	$1.88^{+0.12}_{-0.06}$	$2.01^{+0.14}_{-0.09}$	3.4 ± 0.8	1.4 ± 0.6
29	SFG	$10.39^{+0.33}_{-0.47}$	$-9.28^{+0.29}_{-0.18}$	$1.30^{+0.40}_{-0.20}$	$1.36^{+0.04}_{-0.04}$	$1.20^{+0.03}_{-0.10}$	3.6 ± 1.4	0.8 ± 0.2
30	SFG	$10.03^{+0.31}_{-0.42}$	$-9.04^{+0.20}_{-0.40}$	$1.10^{+0.20}_{-0.30}$	$0.93^{+0.07}_{-0.10}$	$1.02^{+0.05}_{-0.06}$	3.1 ± 1.3	1.1 ± 0.6
31	SFG	$10.01^{+0.36}_{-0.30}$	$-9.36^{+0.30}_{-0.29}$	$1.20^{+0.20}_{-0.40}$	$0.92^{+0.05}_{-0.09}$	$1.15^{+0.02}_{-0.05}$	2.2 ± 0.8	1.2 ± 0.4
32	SFG	$9.89^{+0.33}_{-0.37}$	$-9.08^{+0.18}_{-0.36}$	$0.90^{+0.20}_{-0.20}$	$0.65^{+0.10}_{-0.13}$	$0.85^{+0.06}_{-0.06}$	2.6 ± 0.9	1.1 ± 0.5
33	SFG	$10.26^{+0.29}_{-0.42}$	$-9.19^{+0.40}_{-0.45}$	$1.70^{+0.20}_{-0.33}$	$1.36^{+0.10}_{-0.04}$	$1.22^{+0.09}_{-0.04}$	3.5 ± 0.8	0.9 ± 0.3

Table A.3: Continued

Cid	Class	$\log_{10}(M/M_{\odot})$	$sSFR\,(\mathrm{yr}^{-1})$	$\mathrm{A_V}\ (mag)$	*(V-J)*	*(U-V)*	r_e (kpc)	n
34	SFG	$10.11^{+0.27}_{-0.40}$	$-9.09^{+0.28}_{-0.29}$	$1.30^{+0.18}_{-0.30}$	$1.04^{+0.08}_{-0.05}$	$1.02^{+0.09}_{-0.09}$	3.6 ± 0.8	0.9 ± 0.5
35	SFG	$10.06^{+0.50}_{-0.33}$	$-9.09^{+0.31}_{-0.32}$	$1.55^{+0.15}_{-0.45}$	$1.25^{+0.08}_{-0.09}$	$1.13^{+0.08}_{-0.07}$	3.6 ± 1.0	0.9 ± 0.3
36	SFG	$9.73^{+0.42}_{-0.40}$	$-9.36^{+0.36}_{-0.79}$	$0.60^{+0.20}_{-0.10}$	$0.48^{+0.11}_{-0.11}$	$0.77^{+0.07}_{-0.08}$	2.3 ± 0.8	1.4 ± 0.5
37	SFG	$9.91^{+0.38}_{-0.48}$	$-9.36^{+0.33}_{-0.41}$	$0.80^{+0.20}_{-0.22}$	$0.60^{+0.08}_{-0.08}$	$0.89^{+0.07}_{-0.06}$	2.4 ± 0.9	1.6 ± 0.7
38	SFG	$10.45^{+0.33}_{-0.45}$	$-9.18^{+0.37}_{-0.30}$	$1.65^{+0.35}_{-0.35}$	$1.41^{+0.07}_{-0.07}$	$1.32^{+0.06}_{-0.06}$	3.7 ± 1.1	1.1 ± 0.5
39	SFG	$10.29^{+0.32}_{-0.41}$	$-9.12^{+0.34}_{-0.28}$	$1.55^{+0.25}_{-0.45}$	$1.27^{+0.08}_{-0.07}$	$1.12^{+0.09}_{-0.05}$	3.3 ± 0.5	0.8 ± 0.1
40	TG	$10.51^{+0.58}_{-0.40}$	$-10.09^{+0.17}_{-0.63}$	$0.70^{+0.38}_{-0.50}$	$1.19^{+0.05}_{-0.05}$	$1.60^{+0.07}_{-0.07}$	2.2 ± 1.1	4.6 ± 2.4
41	SFG	$10.02^{+0.36}_{-0.40}$	$-9.17^{+0.26}_{-1.05}$	$1.30^{+0.10}_{-0.20}$	$0.96^{+0.04}_{-0.06}$	$1.05^{+0.05}_{-0.06}$	2.7 ± 1.2	1.4 ± 0.6
42	SFG	$10.00^{+0.29}_{-0.28}$	$-9.00^{+0.34}_{-0.77}$	$1.10^{+0.20}_{-0.10}$	$0.83^{+0.08}_{-0.08}$	$0.89^{+0.03}_{-0.08}$	2.9 ± 1.0	0.8 ± 0.3
43	SFG	$9.92^{+0.22}_{-0.33}$	$-9.20^{+0.20}_{-0.52}$	$0.90^{+0.20}_{-0.20}$	$0.74^{+0.10}_{-0.06}$	$0.97^{+0.05}_{-0.09}$	2.7 ± 1.2	1.5 ± 0.7
44	SFG	$10.10^{+0.57}_{-0.44}$	$-9.44^{+0.46}_{-0.44}$	$1.40^{+0.20}_{-0.60}$	$1.08^{+0.09}_{-0.05}$	$1.20^{+0.08}_{-0.06}$	2.7 ± 0.9	0.9 ± 0.3
45	SFG	$9.67^{+0.51}_{-0.47}$	$-10.46^{+0.95}_{-1.80}$	$0.70^{+0.10}_{-0.28}$	$0.46^{+0.09}_{-0.15}$	$0.82^{+0.05}_{-0.06}$	2.1 ± 0.7	2.6 ± 0.9
46	SFG	$10.05^{+0.26}_{-0.44}$	$-9.36^{+0.36}_{-0.63}$	$1.20^{+0.10}_{-0.20}$	$0.85^{+0.08}_{-0.12}$	$1.01^{+0.07}_{-0.03}$	2.5 ± 0.8	1.2 ± 0.5
47	SFG	$10.32^{+0.34}_{-0.35}$	$-9.23^{+0.24}_{-0.53}$	$1.60^{+0.20}_{-0.40}$	$1.26^{+0.05}_{-0.08}$	$1.28^{+0.05}_{-0.06}$	3.0 ± 1.3	1.3 ± 0.7
48	SFG	$10.43^{+0.38}_{-0.40}$	$-9.58^{+0.39}_{-0.71}$	$1.60^{+0.30}_{-0.60}$	$1.28^{+0.09}_{-0.07}$	$1.39^{+0.09}_{-0.06}$	2.8 ± 0.8	1.6 ± 0.6
49	SFG	$10.59^{+0.38}_{-0.19}$	$-9.17^{+0.39}_{-0.44}$	$2.60^{+0.17}_{-0.60}$	$1.92^{+0.07}_{-0.04}$	$1.61^{+0.09}_{-0.09}$	4.5 ± 0.9	0.8 ± 0.3
50	SFG	$9.95^{+0.49}_{-0.48}$	$-9.58^{+0.39}_{-0.88}$	$1.40^{+0.10}_{-0.60}$	$0.99^{+0.07}_{-0.16}$	$1.22^{+0.10}_{-0.05}$	2.0 ± 1.0	2.1 ± 0.7

Table A.3: Continued

Cid	Class	$\log_{10}(M/M_{\odot})$	$sSFR\,(\mathrm{yr}^{-1})$	$\mathrm{A_V}$ (mag)	*(V-J)*	*(U-V)*	r_e (kpc)	n
51	SFG	$10.36^{+0.43}_{-0.58}$	$-9.58^{+0.21}_{-1.59}$	$1.50^{+0.20}_{-0.30}$	$1.10^{+0.08}_{-0.06}$	$1.33^{+0.07}_{-0.05}$	2.4 ± 0.9	2.1 ± 0.8
52	TG	$10.23^{+0.35}_{-0.57}$	$-10.36^{+0.44}_{-0.32}$	$0.80^{+0.60}_{-0.55}$	$1.00^{+0.04}_{-0.05}$	$1.44^{+0.06}_{-0.05}$	1.3 ± 0.6	3.7 ± 2.4
53	SFG	$10.70^{+0.28}_{-0.32}$	$-9.74^{+0.74}_{-1.12}$	$2.80^{+0.10}_{-0.66}$	$1.99^{+0.07}_{-0.06}$	$1.76^{+0.09}_{-0.07}$	3.8 ± 0.8	1.2 ± 0.4
54	TG	$10.41^{+0.37}_{-0.42}$	$-10.15^{+0.24}_{-0.40}$	$1.00^{+0.50}_{-0.71}$	$1.12^{+0.06}_{-0.08}$	$1.52^{+0.05}_{-0.07}$	2.3 ± 1.0	3.0 ± 1.0
55	SFG	$10.79^{+0.35}_{-0.32}$	$-9.77^{+0.49}_{-0.61}$	$2.90^{+0.30}_{-0.60}$	$2.18^{+0.14}_{-0.06}$	$1.88^{+0.13}_{-0.10}$	4.1 ± 0.9	1.3 ± 0.4
56	TG	$10.57^{+0.26}_{-0.35}$	$-9.84^{+0.43}_{-0.38}$	$1.45^{+0.62}_{-0.62}$	$1.41^{+0.09}_{-0.07}$	$1.56^{+0.05}_{-0.09}$	3.4 ± 1.3	2.0 ± 0.5
57	SFG	$10.64^{+0.25}_{-0.18}$	$-9.84^{+0.39}_{-0.86}$	$1.90^{+0.50}_{-0.70}$	$1.64^{+0.04}_{-0.09}$	$1.74^{+0.04}_{-0.09}$	3.9 ± 1.5	1.7 ± 0.7
58	SFG	$10.37^{+0.43}_{-0.30}$	$-9.45^{+0.45}_{-0.33}$	$2.00^{+0.10}_{-0.70}$	$1.48^{+0.05}_{-0.04}$	$1.43^{+0.08}_{-0.05}$	3.3 ± 1.4	1.1 ± 0.4
59	TG	$10.51^{+0.41}_{-0.37}$	$-10.70^{+0.34}_{-0.38}$	$0.40^{+0.40}_{-0.30}$	$1.08^{+0.10}_{-0.04}$	$1.65^{+0.08}_{-0.06}$	1.7 ± 1.0	4.7 ± 1.7
60	SFG	$10.50^{+0.31}_{-0.23}$	$-9.56^{+0.28}_{-1.74}$	$2.00^{+0.30}_{-0.30}$	$1.54^{+0.08}_{-0.05}$	$1.56^{+0.10}_{-0.07}$	4.3 ± 1.6	1.6 ± 0.6
61	TG	$10.64^{+0.19}_{-0.46}$	$-10.41^{+0.05}_{-0.37}$	$0.85^{+0.52}_{-0.19}$	$1.27^{+0.04}_{-0.06}$	$1.68^{+0.05}_{-0.07}$	2.1 ± 0.8	2.2 ± 1.1
62	TG	$10.75^{+0.27}_{-0.33}$	$-10.15^{+0.43}_{-1.01}$	$2.10^{+0.39}_{-0.80}$	$1.75^{+0.07}_{-0.06}$	$1.84^{+0.09}_{-0.11}$	3.2 ± 1.1	1.3 ± 0.6
63	TG	$10.50^{+0.29}_{-0.57}$	$-10.91^{+0.75}_{-0.65}$	$0.95^{+0.45}_{-0.84}$	$1.08^{+0.05}_{-0.08}$	$1.52^{+0.05}_{-0.06}$	1.9 ± 0.6	3.5 ± 1.8
64	QG	$10.85^{+0.20}_{-0.31}$	$-11.08^{+0.54}_{-0.54}$	$0.80^{+0.62}_{-0.20}$	$1.48^{+0.06}_{-0.12}$	$2.01^{+0.10}_{-0.13}$	2.3 ± 0.7	2.9 ± 1.1
65	PSB	$10.52^{+0.34}_{-0.43}$	$-11.23^{+0.53}_{-1.78}$	$0.40^{+0.10}_{-0.20}$	$0.82^{+0.07}_{-0.11}$	$1.54^{+0.04}_{-0.04}$	0.9 ± 0.3	3.5 ± 1.1
66	QG	$10.57^{+0.38}_{-0.31}$	$-11.38^{+0.47}_{-1.60}$	$0.50^{+0.20}_{-0.20}$	$1.16^{+0.05}_{-0.04}$	$1.83^{+0.06}_{-0.06}$	1.7 ± 0.6	4.5 ± 1.3
67	TG	$10.51^{+0.42}_{-0.36}$	$-10.54^{+0.39}_{-3.10}$	$1.10^{+0.82}_{-0.22}$	$1.40^{+0.10}_{-0.06}$	$1.67^{+0.15}_{-0.06}$	2.8 ± 1.2	1.5 ± 0.7

Table A.3: Continued

Cid	Class	$\log_{10}(M/M_{\odot})$	$sSFR\,(\mathrm{yr}^{-1})$	$\mathrm{A_V}\ (mag)$	*(V-J)*	*(U-V)*	r_e (kpc)	n
68	QG	$10.68^{+0.27}_{-0.37}$	$-11.69^{+0.31}_{-1.55}$	$0.50^{+0.20}_{-0.30}$	$1.26^{+0.07}_{-0.06}$	$1.91^{+0.06}_{-0.05}$	1.7 ± 0.6	3.5 ± 1.1
69	PSB	$10.51^{+0.32}_{-0.35}$	$-11.38^{+0.62}_{-4.10}$	$0.50^{+0.17}_{-0.40}$	$0.93^{+0.09}_{-0.06}$	$1.60^{+0.05}_{-0.04}$	1.1 ± 0.4	3.6 ± 1.1
70	QG	$10.37^{+0.47}_{-0.43}$	$-11.38^{+0.15}_{-5.47}$	$0.30^{+0.44}_{-0.10}$	$1.00^{+0.05}_{-0.05}$	$1.69^{+0.07}_{-0.04}$	1.3 ± 0.4	3.7 ± 0.9
71	QG	$10.57^{+0.31}_{-0.28}$	$-11.62^{+0.24}_{-2.76}$	$0.40^{+0.30}_{-0.20}$	$1.09^{+0.05}_{-0.03}$	$1.77^{+0.05}_{-0.05}$	1.4 ± 0.5	3.8 ± 1.1

Table A.4: Analog Galaxy Parameters for Composite SEDs at $2.5 < z < 4.0$.

Cid	Class	$\log_{10}(M/M_{\odot})$	$sSFR\,(\mathrm{yr}^{-1})$	$\mathrm{A_V}$ (mag)	*(V-J)*	*(U-V)*	r_e (kpc)	n
0	ELG	$8.59^{+0.63}_{-0.33}$	$-6.87^{+0.15}_{-1.51}$	$0.70^{+0.11}_{-0.70}$	$-0.36^{+0.38}_{-0.24}$	$0.35^{+0.19}_{-0.25}$	1.1 ± 0.5	1.5 ± 1.2
1	ELG	$8.84^{+0.49}_{-0.24}$	$-7.13^{+0.10}_{-1.25}$	$0.60^{+0.10}_{-0.50}$	$-0.18^{+0.35}_{-0.34}$	$0.24^{+0.17}_{-0.09}$	1.2 ± 0.5	1.3 ± 0.8
2	SFG	$9.30^{+0.23}_{-0.43}$	$-8.45^{+1.25}_{-0.33}$	$0.15^{+0.43}_{-0.15}$	$-0.07^{+0.30}_{-0.30}$	$0.23^{+0.08}_{-0.05}$	1.5 ± 0.4	1.6 ± 0.9
3	ELG	$8.84^{+0.26}_{-0.27}$	$-7.06^{+0.09}_{-0.08}$	$0.90^{+0.10}_{-0.10}$	$-0.10^{+0.16}_{-0.25}$	$0.35^{+0.23}_{-0.07}$	1.5 ± 0.6	1.2 ± 0.8
4	SFG	$9.43^{+0.30}_{-0.54}$	$-8.30^{+1.10}_{-0.60}$	$0.30^{+0.50}_{-0.30}$	$0.06^{+0.30}_{-0.17}$	$0.30^{+0.11}_{-0.10}$	1.6 ± 0.6	1.5 ± 0.7
5	SFG	$9.64^{+0.19}_{-0.29}$	$-8.99^{+0.46}_{-0.18}$	$0.20^{+0.20}_{-0.20}$	$0.11^{+0.21}_{-0.23}$	$0.35^{+0.16}_{-0.11}$	1.6 ± 0.7	1.1 ± 0.5
6	SFG	$9.12^{+0.72}_{-0.35}$	$-7.24^{+0.09}_{-1.71}$	$0.80^{+0.20}_{-0.70}$	$0.06^{+0.32}_{-0.31}$	$0.36^{+0.12}_{-0.09}$	1.7 ± 0.5	1.0 ± 0.6
7	SFG	$9.76^{+0.19}_{-0.24}$	$-9.00^{+0.36}_{-0.36}$	$0.30^{+0.32}_{-0.30}$	$0.21^{+0.30}_{-0.13}$	$0.55^{+0.09}_{-0.16}$	1.7 ± 0.6	1.9 ± 1.0
8	SFG	$9.72^{+0.24}_{-0.31}$	$-8.99^{+0.64}_{-0.37}$	$0.30^{+0.30}_{-0.20}$	$0.22^{+0.25}_{-0.23}$	$0.41^{+0.14}_{-0.10}$	1.7 ± 0.5	1.2 ± 0.6
9	SFG	$9.97^{+0.25}_{-0.31}$	$-8.82^{+0.29}_{-0.21}$	$0.60^{+0.28}_{-0.10}$	$0.58^{+0.28}_{-0.20}$	$0.62^{+0.11}_{-0.08}$	2.1 ± 0.8	1.1 ± 0.8
10	SFG	$9.83^{+0.26}_{-0.16}$	$-9.00^{+0.21}_{-0.44}$	$0.40^{+0.20}_{-0.30}$	$0.30^{+0.20}_{-0.19}$	$0.51^{+0.13}_{-0.12}$	1.8 ± 0.7	1.3 ± 0.7
11	SFG	$10.02^{+0.25}_{-0.27}$	$-9.00^{+0.19}_{-0.44}$	$0.50^{+0.30}_{-0.20}$	$0.42^{+0.21}_{-0.16}$	$0.62^{+0.10}_{-0.14}$	2.0 ± 0.6	1.4 ± 0.8
12	SFG	$10.23^{+0.27}_{-0.30}$	$-8.87^{+0.22}_{-0.20}$	$1.00^{+0.10}_{-0.10}$	$0.76^{+0.22}_{-0.04}$	$0.83^{+0.09}_{-0.11}$	2.2 ± 1.1	1.1 ± 0.3
13	SFG	$10.08^{+0.23}_{-0.26}$	$-9.07^{+0.41}_{-0.52}$	$0.70^{+0.20}_{-0.30}$	$0.54^{+0.21}_{-0.28}$	$0.65^{+0.16}_{-0.17}$	2.1 ± 0.6	1.5 ± 0.5
14	SFG	$10.05^{+0.22}_{-0.20}$	$-9.44^{+0.45}_{-0.55}$	$0.70^{+0.29}_{-0.30}$	$0.49^{+0.20}_{-0.15}$	$0.70^{+0.07}_{-0.15}$	2.8 ± 1.1	1.1 ± 0.4
15	SFG	$9.99^{+0.30}_{-0.26}$	$-9.61^{+0.58}_{-1.56}$	$0.80^{+0.10}_{-0.20}$	$0.55^{+0.12}_{-0.19}$	$0.84^{+0.04}_{-0.16}$	1.8 ± 0.8	1.1 ± 0.6
16	SFG	$10.96^{+0.20}_{-0.50}$	$-9.74^{+1.30}_{-0.40}$	$2.50^{+0.22}_{-0.41}$	$1.91^{+0.27}_{-0.11}$	$1.64^{+0.31}_{-0.30}$	2.8 ± 1.2	0.9 ± 0.4

Table A.4: Continued

Cid	Class	$\log_{10}(M/M_{\odot})$	$sSFR\,(\mathrm{yr}^{-1})$	$\mathrm{A_V}\ (mag)$	*(V-J)*	*(U-V)*	r_e (kpc)	n
17	SFG	$10.53^{+0.23}_{-0.41}$	$-9.07^{+0.55}_{-0.89}$	$1.50^{+0.34}_{-0.20}$	$1.30^{+0.33}_{-0.15}$	$1.15^{+0.16}_{-0.15}$	2.8 ± 0.7	1.2 ± 0.9
18	PSB	$10.50^{+0.39}_{-0.33}$	$-10.36^{+0.31}_{-0.69}$	$0.40^{+0.46}_{-0.30}$	$0.78^{+0.07}_{-0.35}$	$1.40^{+0.09}_{-0.05}$	1.1 ± 0.7	7.8 ± 0.2
19	PSB	$10.66^{+0.34}_{-0.20}$	$-11.66^{+0.96}_{-2.64}$	$0.50^{+0.30}_{-0.10}$	$0.89^{+0.21}_{-0.18}$	$1.59^{+0.22}_{-0.09}$	0.9 ± 0.4	3.1 ± 1.2

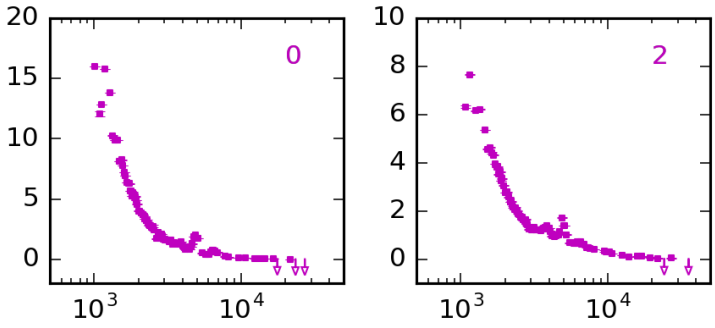

Figure A.1: ELG composite SEDs at $1 < z < 3$. These are plotted as scaled F_λ against wavelength.

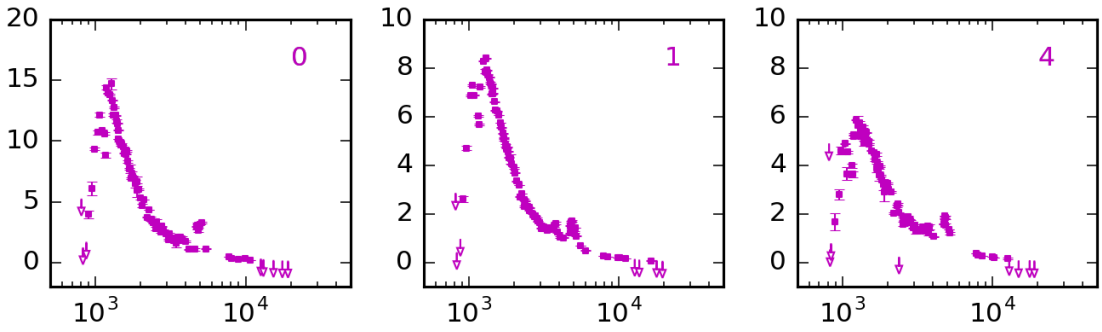

Figure A.2: ELG composite SEDs at $2.5 < z < 4$. These are plotted as scaled F_λ against wavelength.

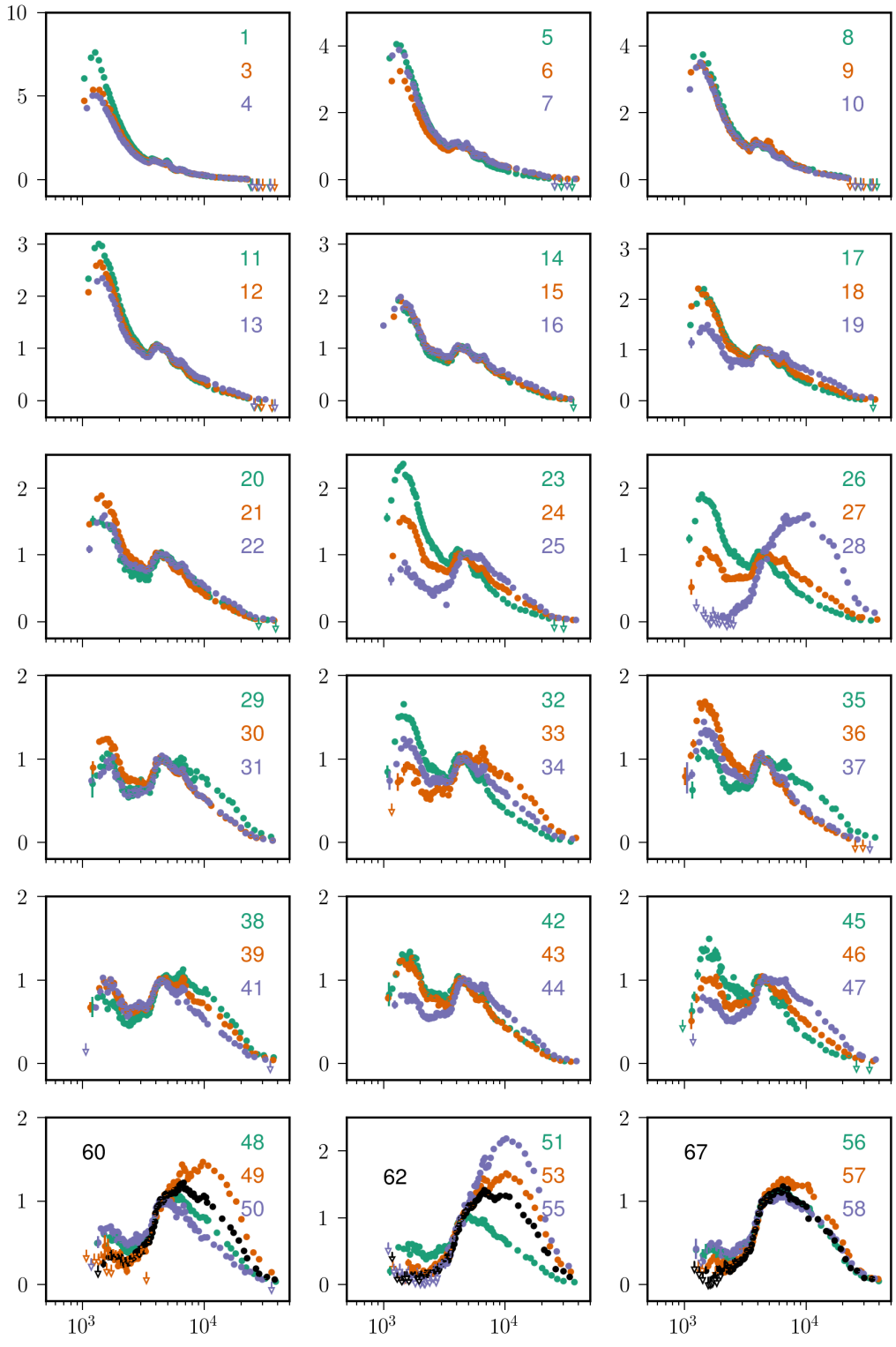

Figure A.3: SFG composite SEDs at $1 < z < 3$. These are plotted as scaled F_λ against wavelength. Each panel has 3 composite SEDs - we have changed the blue color used throughout much of the paper for clarity and grouped by UV flux. Note that the y-axis range changes between panels, although the abscissae are identical. There are many composite SED pairs which are similar, and we do not claim that these are all separate populations, although many have differences, as shown throughout this work.

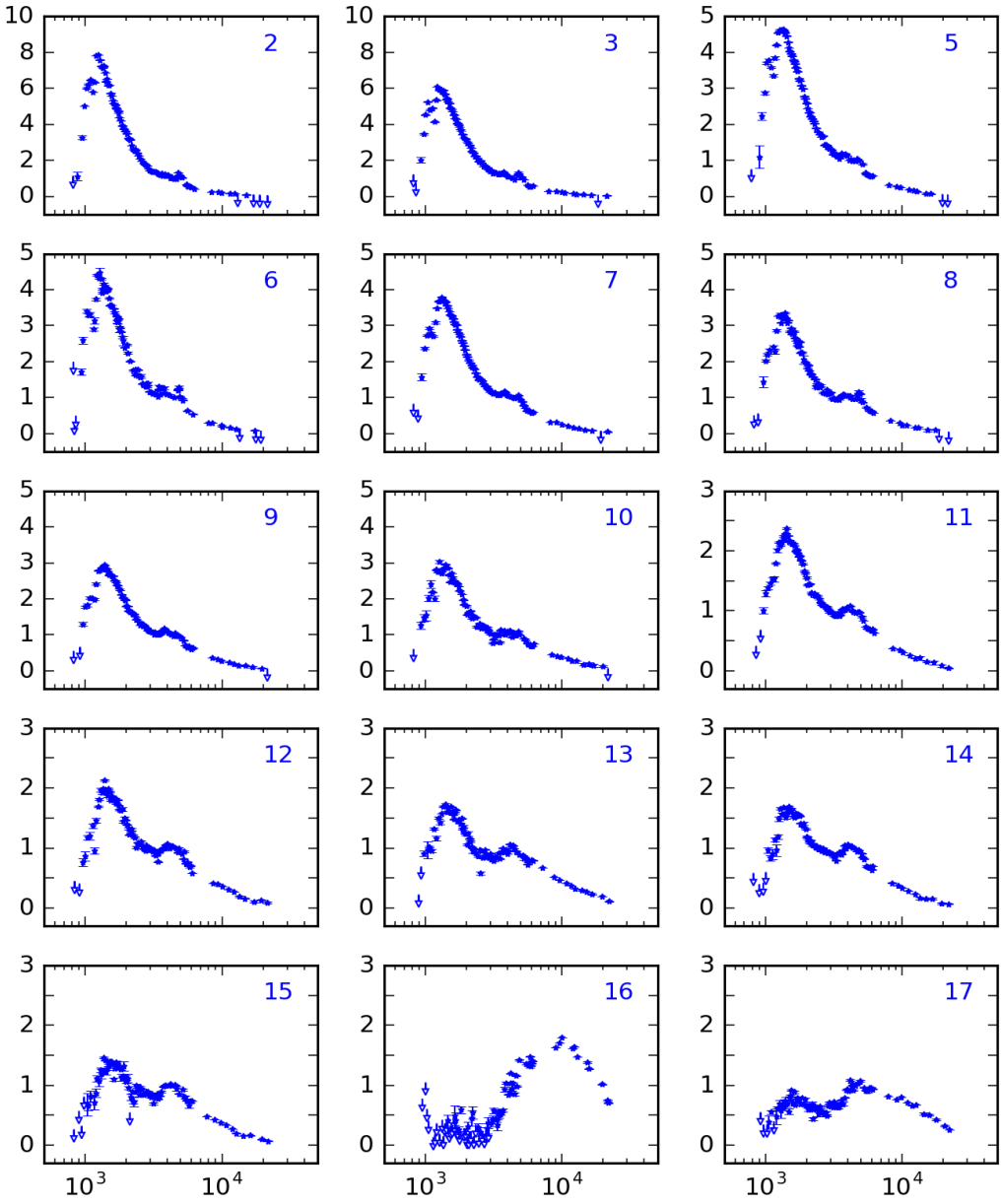

Figure A.4: SFG composite SEDs at $2.5 < z < 4$. These are plotted as scaled F_λ against wavelength. Note that the y-axis range changes between panels, although the abscissae are identical.

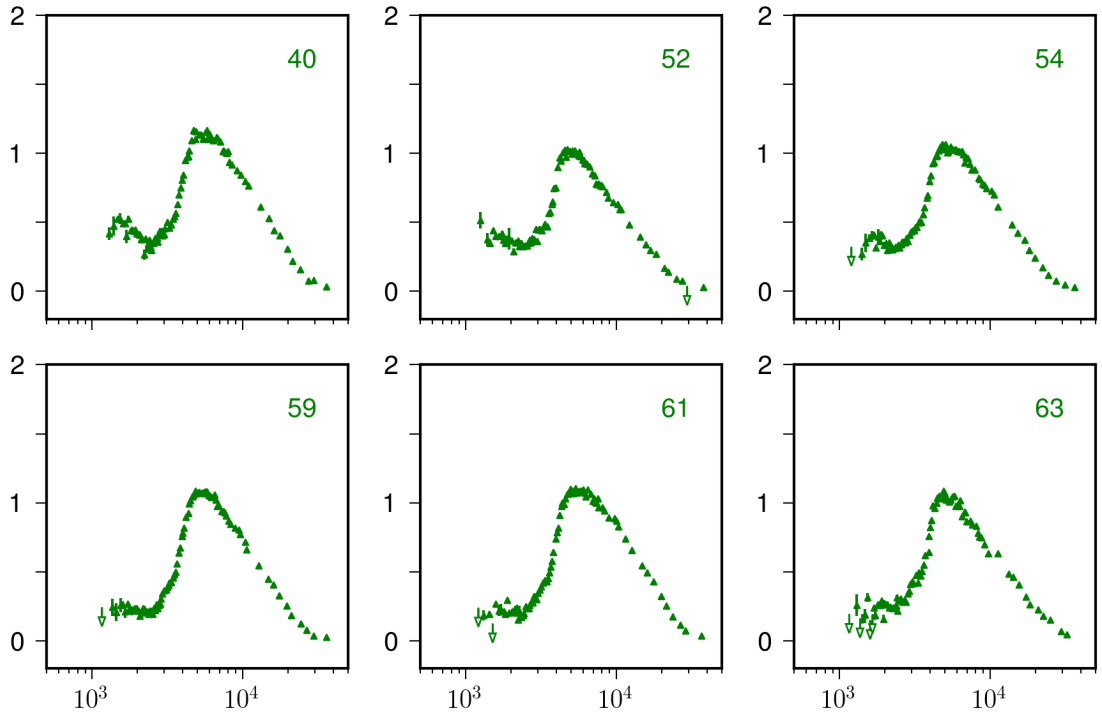

Figure A.5: TG composite SEDs at $1 < z < 3$. These are plotted as scaled F_λ against wavelength.

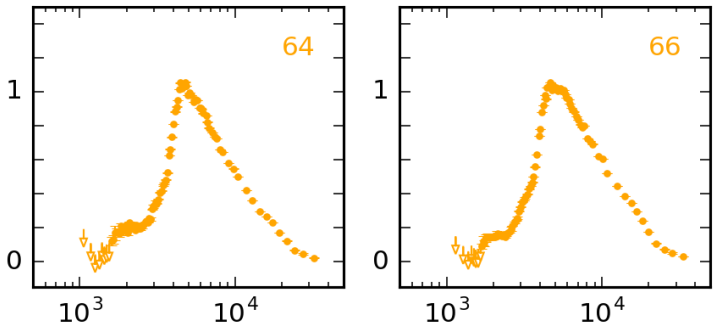

Figure A.6: PSB composite SEDs at $1 < z < 3$. These are plotted as scaled F_λ against wavelength.

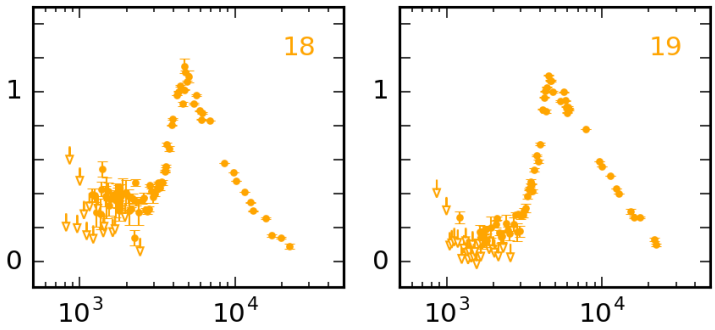

Figure A.7: PSB composite SEDs at $2.5 < z < 4$. These are plotted as scaled F_λ against wavelength.

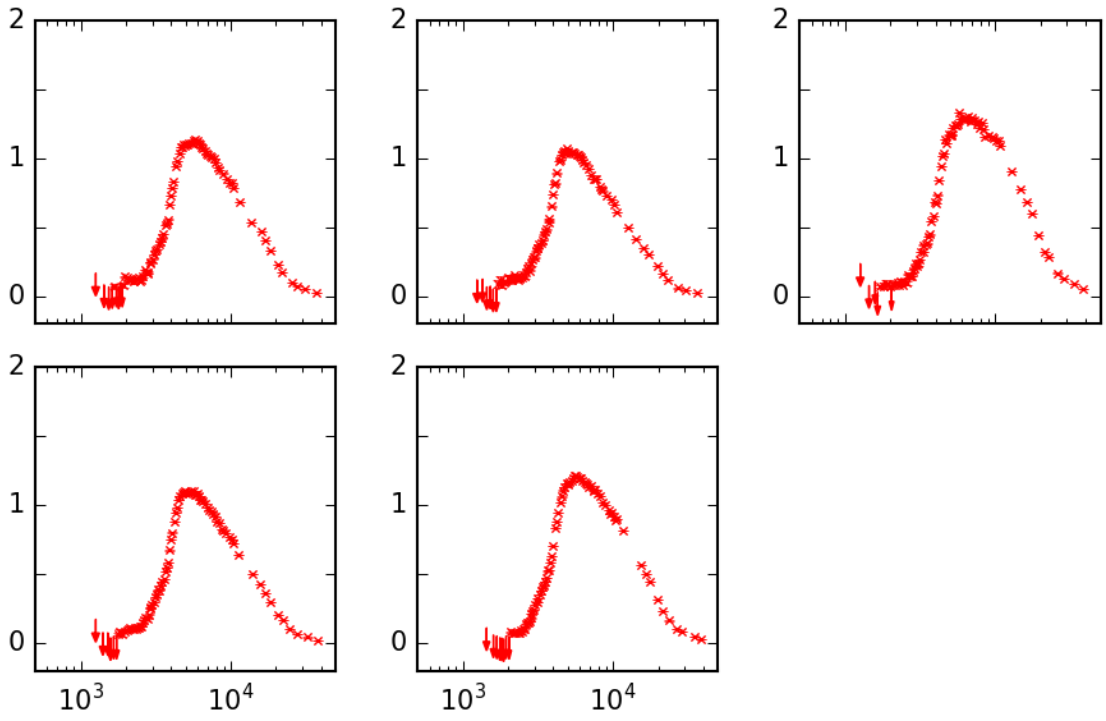

Figure A.8: QG composite SEDs at $1 < z < 3$. These are plotted as scaled F_λ against wavelength.